

TWO PHASE FLOW PHENOMENA IN FUEL CELL MICROCHANNELS

A DISSERTATION

SUBMITTED TO THE DEPARTMENT OF MECHANICAL ENGINEERING

AND THE COMMITTEE ON GRADUATE STUDIES

OF STANFORD UNIVERSITY

IN PARTIAL FULFILLMENT OF THE REQUIREMENTS

FOR THE DEGREE OF

DOCTOR OF PHILOSOPHY

Julie Elizabeth Steinbrenner

March 2011

© 2011 by Julie Elizabeth Steinbrenner. All Rights Reserved.  
Re-distributed by Stanford University under license with the author.



This work is licensed under a Creative Commons Attribution-Noncommercial 3.0 United States License.  
<http://creativecommons.org/licenses/by-nc/3.0/us/>

This dissertation is online at: <http://purl.stanford.edu/gz938pg6790>

I certify that I have read this dissertation and that, in my opinion, it is fully adequate in scope and quality as a dissertation for the degree of Doctor of Philosophy.

**Kenneth Goodson, Primary Adviser**

I certify that I have read this dissertation and that, in my opinion, it is fully adequate in scope and quality as a dissertation for the degree of Doctor of Philosophy.

**John Eaton**

I certify that I have read this dissertation and that, in my opinion, it is fully adequate in scope and quality as a dissertation for the degree of Doctor of Philosophy.

**Carlos Hidrovo**

Approved for the Stanford University Committee on Graduate Studies.

**Patricia J. Gumpert, Vice Provost Graduate Education**

*This signature page was generated electronically upon submission of this dissertation in electronic format. An original signed hard copy of the signature page is on file in University Archives.*



# Abstract

Proton exchange membrane (PEM) fuel cells show promise as CO<sub>2</sub>-free energy-conversion devices. Reducing the size of the gas delivery channels could improve the efficiency and power density of PEM fuel cells by expanding geometric flexibility, reducing lengths of resistive transport paths, and improving the volumetric power density of fuel cell stacks. However, the expected benefits of reduced channel sizes have not been realized due to flooding by water generated at the cathode, which can impede the flow of reactant gases to catalyst sites and dramatically reduce cathodic reaction rates. Channels with small dimensions exhibit an increased propensity toward flooding as surface tension forces become significant when compared with viscous, inertial, and pressure forces.

Optimization of fuel cells, heat exchangers, and other practical devices employing two-phase flow requires an understanding of the physics of the flow and the distinct two-phase flow profiles that result from the interplay of these forces. Despite the fact that the channel geometry is one of the key design parameters of a fluidic system, little previous research examines the effect that microchannel geometry has on the flow structure. This study examines the two-phase flow in channels relevant for PEM fuel cells, incorporating asymmetric water injection in silicon channels of various aspect

ratios and sizes, and developing ex-situ PEM fuel cell channel test structures to visualize the evolution of flow regimes along their length.

First, we investigate fundamental water-gas interactions in silicon channels of varied hydraulic diameters and cross-sectional aspect ratios using a high-contrast fluorescent imaging technique. Flow regime mapping corroborates previously published boundaries between intermittent and separated flow regimes and extends the inquiry to include the effect of side-wall injection conditions which lead to the formation of stratified flow in small square channels and high aspect ratio channels. These stratified flows predominate in high aspect ratio channels and the formation of intermittent plug/slug flow regimes is suppressed. An analytical, stratified flow model is validated using film thickness measurements, and then used to explore the effects of channel aspect ratio and film configuration on parameters such as the pressure losses and liquid coverage of a channel wall. We study the evolution of two-phase flow structures in a microchannel geometry that mimics conditions in a fuel cell channel – a 60-cm long channel with distributed water introduction through a porous gas diffusion layer (GDL) on one wall. In these channels, intermittent flow regimes transition to stable films as more water is introduced into the channel downstream. We develop simple relationships relevant for the optimization of channel design for the evacuation of water. Finally, we present considerations for the implementation of spinning-disk confocal microscopy to provide three-dimensional (3D) visualization of two-phase flow structures. Such a technique may provide insight into key flow transitions that were observed during high-speed fluorescent flow visualization.

By characterizing and modeling two-phase flow in various microchannel geometries under a large range of flow conditions, these studies provide insight that enables the improved design of microchannels for two-phase flow in fuel cells.

# Acknowledgements

In addition to the incredible resources and facilities available at Stanford University, the true asset of this place is the exceptional people who populate it. First and foremost, I thank my advisor, Professor Ken Goodson for his support and encouragement throughout my thesis program. I know that he often takes extra stress on himself in order to allow his students to explore the questions that interest them; it is a gift and a privilege for his students. His advice too, is a gift, and often contains wisdom that becomes only more and more apparent with time.

I thank my reading committee for their time and contributions to my thesis work. Professor Carlos Hidrovo is a mentor and a friend, who gave me great advice and encouragement throughout the past years. Professor John Eaton is a talented researcher and teacher whose insight and ideas were always very helpful.

Much of my work would not have been possible without the collaboration of the other students of the fuel cell project. I thank Fumin Wang for the countless hours he spent fabricating samples, to Sebastien Vigneron for many insightful conversations about life and math, and to Eon Soo Lee who collaborated with me in the lab.

The other members of the Microheat laboratory have been an integral part of my learning and growing during graduate school. I started to name names and tell stories,



but I just couldn't find a good place to stop, so I won't even start here. You are inspiring to me in your enthusiasm for life and heat transfer. I do owe special thanks to Joe, Milnes, Roger, Saniya, and Anita – I value your insights, aids, ideas, and friendship.

I would not be here if it were not for the advice, support, and encouragement of two of my undergraduate professors from Valparaiso University, Dr. Michael Barrett and Prof. Robert Palumbo. They each inspired in me a desire to learn energy systems, taught me the fundamental techniques and motivations for research, and challenged me to live a life and a career that has a positive influence. I cannot understate the impact that working with them has had on my professional and personal development and I would not be where I am today if it were not for them.

To my friends, thank you for being there for me through the years. I cherish the laughs we've had, the meals we've shared, the issues we've debated, the mountains we've climbed, the bubble teas we've sipped, the roads we've run and biked, the places we've camped, the trails we've hiked, the ravines we've canyoneer-ed, the oceans we've explored, the bells we've rung, the slopes we've skied, and the memories we've made. My life would not be as rich without you.

Finally, to my family, I repeat the phrase that I've used before -- *I did it because you believed that I could*. Your unfailing love, support, and confidence have lifted me up throughout this journey. To my mom and dad especially, I want to thank you for the sacrifices you've made, for the wisdom you've shared, and for the example you've been throughout my life.

I am grateful to have been awarded the Charles H. Kruger Stanford Graduate Fellowship at the beginning of my graduate studies. I thankfully acknowledge the financial support for my work which was provided by Honda Research and Development, Inc., by a DURIP grant from the Office of Naval Research, and by access to the Stanford Nanofabrication Facility, an NSF supported-laboratory. I acknowledge the support of the Chateaubriand Fellowship which provided me the engaging opportunity to work at the Commissariat à l'Energie Atomique in Grenoble, France during a leave of absence from my thesis work in 2007.

# Table of Contents

ABSTRACT .....	V
ACKNOWLEDGEMENTS .....	VIII
TABLE OF CONTENTS .....	XI
LIST OF TABLES.....	XIV
LIST OF FIGURES.....	XV
CHAPTER 1. INTRODUCTION.....	1
1.1    BACKGROUND AND MOTIVATION.....	1
1.2    TWO-PHASE FLOW FUNDAMENTALS .....	3
1.3    LIQUID WATER VISUALIZATION IN PEM FUEL CELLS .....	8
1.3.1 <i>In-situ</i> .....	8
1.3.2 <i>Ex-situ</i> .....	10
1.4    OVERVIEW OF THIS WORK .....	12
CHAPTER 2. FLUORESCENT VISUALIZATION OF TWO-PHASE FLOW REGIMES IN RECTANGULAR MICROCHANNELS.....	13
2.1    MOTIVATION .....	13
2.2    EXPERIMENTAL METHOD .....	16
2.2.1 <i>Microfabricated experimental structures</i> .....	16

2.2.2	<i>Experimental apparatus</i> .....	17
2.2.3	<i>Fluorescent imaging technique</i> .....	19
2.3	PROCEDURE .....	21
2.4	RESULTS AND DISCUSSION .....	22
2.4.1	<i>Flow Regime Maps</i> .....	22
2.4.2	<i>Plug flow</i> .....	25
2.4.3	<i>Annular flow</i> .....	31
2.4.4	<i>Stratified flow</i> .....	33
2.4.5	<i>Conclusions</i> .....	35
<b>CHAPTER 3. STRATIFIED FLOW PHYSICS .....</b>		<b>36</b>
3.1	ANALYTICAL STUDIES OF STRATIFIED FLOW .....	36
3.1.1	<i>Non-dimensionalization and aspect ratio effects</i> .....	40
3.1.2	<i>Assessment of a simplified model</i> .....	44
3.2	STRATIFIED FLOW EXPERIMENTS .....	47
3.3	EXPERIMENTAL METHOD .....	47
3.3.1	<i>Measurement procedure</i> .....	47
3.3.2	<i>Data analysis</i> .....	49
3.3.3	<i>Uncertainty</i> .....	50
3.4	RESULTS AND DISCUSSION.....	52
3.4.1	<i>Images</i> .....	52
3.4.2	<i>Film thickness measurements</i> .....	55
3.5	CONCLUSIONS.....	63
<b>CHAPTER 4. TWO-PHASE FLOW VISUALIZATION IN AN EX-SITU PEM FUEL CELL CHANNEL .....</b>		<b>65</b>
4.1	EXPERIMENTAL METHOD .....	66
4.1.1	<i>Sample geometry and preparation</i> .....	66
4.1.2	<i>Procedure</i> .....	68

4.1.3	<i>Flow Visualization</i> .....	71
4.2	RESULTS AND DISCUSSION.....	73
4.2.1	<i>General trends</i> .....	73
4.2.2	<i>Comparison of flow conditions</i> .....	79
4.2.3	<i>Variation of flow structure with flow rate</i> .....	80
4.2.4	<i>Effect of corners on flow regime evolution</i> .....	82
4.2.5	<i>Implications for fuel cell channel design</i> .....	85
4.3	SUMMARY AND CONCLUSIONS .....	88
<b>CHAPTER 5. INSIGHTS INTO CONFOCAL VISUALIZATION FOR TWO-PHASE FLOW.</b>		<b>91</b>
5.1	BASICS OF CONFOCAL MICROSCOPY .....	91
5.2	CONSIDERATIONS FOR TWO-PHASE FLOW IMAGING .....	95
5.3	DEMONSTRATION OF SYSTEM .....	99
5.4	CONCLUSIONS .....	102
<b>CHAPTER 6. CONCLUSIONS AND FUTURE DIRECTIONS</b> .....		<b>103</b>
<b>APPENDIX A. ANALYTICAL SOLUTION TO STRATIFIED FLOW IN A RECTANGULAR CHANNEL</b> .....		<b>109</b>
<b>REFERENCES</b> .....		<b>117</b>

# List of Tables

Table 2.1: Channel Geometries .....	17
Table 4.1: Experimental conditions and fuel cell equivalents for serpentine channels	70
Table 4.2: Experimental conditions for straight channels with equivalent fuel cell parameters.....	86
Table 5.1: Key parameters for systems traditional for confocal imaging and two-phase systems .....	96
Table A.1: Boundary conditions for stratified flow solution .....	110
Table A.2: Interface conditions for stratified flow solution .....	111
Table A.3: Definition of parameters and non-dimensionalizations.....	111

# List of Figures

Figure 1.1: Transport processes in a PEM fuel cell.....	2
Figure 2.1: Flow regime maps from previous visualization studies in square cross-section microchannels .....	15
Figure 2.2: Layout of channel structures.....	16
Figure 2.3: Schematic of experimental setup. ....	18
Figure 2.4: Schematic of fluorescent imaging principle .....	20
Figure 2.5: Flow regime map for five types of channels of various dimensions and aspect ratios. ....	24
Figure 2.6: Representative images of plug flow in 50 and 100 $\mu\text{m}$ square channels...	26
Figure 2.7: Seven consecutive frames of high-speed images of plug formation at water injection inlet of 100 $\mu\text{m}$ square channel .....	27
Figure 2.8: Formation of a plug.....	30
Figure 2.9: Image of the formation of annular flow at the water inlet in a 50 $\mu\text{m}$ x 50 $\mu\text{m}$ square channel.....	31
Figure 2.10: Prevalence of stratified flow on the regime map and schematics of channel cross-sections in which it is observed. ....	34
Figure 3.1: Schematic of geometry for analytical solution .....	37

Figure 3.2: Velocity profile in liquid phase calculated from analytical solution to stratified two-phase flow in 500 x 45 $\mu\text{m}$ rectangular microchannel .....	38
Figure 3.3: Geometry for aspect ratio and GDL coverage area analysis.....	42
Figure 3.4: Decrease of channel coverage ratio with increasing channel aspect ratio. ....	43
Figure 3.5: Increase in pressure requirement for increasing channel aspect ratio over a range of stoichiometric ratios. ....	44
Figure 3.6: Deviation factor of gas-phase area model of stratified flow compared with a 2D analytical solution. ....	46
Figure 3.7: Process of image thresholding with an example image of stratified flow at the water injection location .....	49
Figure 3.8: Example images of stratified flow from 500 $\mu\text{m}$ x 45 $\mu\text{m}$ channels.....	53
Figure 3.9: Example images of stratified flow in 500 $\mu\text{m}$ x 400 $\mu\text{m}$ channels. ....	54
Figure 3.10: Variation of film thickness with inlet air superficial velocity in 500 $\mu\text{m}$ x 45 $\mu\text{m}$ channel .....	56
Figure 3.11: Variation of film thickness with superficial air velocity in 500 $\mu\text{m}$ x 45 $\mu\text{m}$ channels for a variety of water injection rates .....	57
Figure 3.12: Presentation of film thickness variation results from 500 $\mu\text{m}$ x 50 $\mu\text{m}$ channels according to non-dimensional parameters, film thickness fraction and ratio of volumetric flow rates. ....	58
Figure 3.13: Variation in film thickness with volumetric flow rate ratio in a 430 $\mu\text{m}$ x 240 $\mu\text{m}$ channel compared with the analytical solution .....	60
Figure 3.14: Variation of film thickness fraction with volumetric flow rate ratio in 500 $\mu\text{m}$ x 400 $\mu\text{m}$ U-shaped channel.....	63



Figure 4.1: Channel assembly. ....	67
Figure 4.2: Schematic of experimental setup. ....	69
Figure 4.3: Image decomposition .....	71
Figure 4.4: Representative images of two-phase flow structures .....	72
Figure 4.5: Viscous losses in straight and serpentine channels .....	73
Figure 4.6: Observed flow structures and general evolution of flow regimes. ....	75
Figure 4.7: Images of flow transitions from stratified flow on two walls to one wall. .....	77
Figure 4.8: Flow regimes in serpentine channels mapped against superficial air and water velocities .....	81
Figure 4.9: Flow regime map for straight channels with equivalent flow rates to serpentine channel conditions of Figure 4.8.....	84
Figure 5.1: Illustration of confocal imaging principle for (a) laser scanning microscopy and (b) spinning-disk microscopy.....	93
Figure 5.2: Schematic of spinning disk implementation using Nikon TE2000-U inverted microscope and Hyphenated Systems confocal unit .....	94
Figure 5.3: Comparison of optical path for reflected and fluorescent imaging of specularly-reflecting air-water interfaces. ....	97
Figure 5.4: Illustration of the effect of improper dye concentration in two-phase flow imaging using a confocal microscope. ....	99
Figure 5.5: Processing of fluorescent droplet images. Vertical slice of (a) raw data (b) 3 point 3D median filtered data (c) 5-point 3D median filtered data. ....	100

Figure 5.6: Results of reconstruction of droplet profile from confocal images of planes, or “slices” within the droplet.....	101
Figure A.1: Geometry for analytical solution to stratified flow in rectangular channel	
(a) liquid film on one wall (b) liquid film on two opposite walls .....	109

# Chapter 1. Introduction

## 1.1 Background and Motivation

Proton exchange membrane (PEM) fuel cells are a promising technology in the search for portable CO<sub>2</sub>-free energy conversion alternatives. In these devices, electricity is produced when hydrogen, encountering a catalyst, is separated into its ions at the anode. While protons pass through a semi-permeable membrane, electrons are forced to pass through an external circuit, producing electricity. At the cathode, the ions combine with oxygen to produce water which is typically evacuated through the gas delivery channels on the cathode side. While there are some variations in the construction and materials, a single fuel cell consists of the polymer electrolyte membrane, flanked on either side by catalyst layers and porous carbon paper gas diffusion layers (GDLs), and sandwiched between the anode and cathode bipolar plates which contain the gas delivery channels. Figure 1.1 shows the geometry of the fuel cell.

Water management is a performance-limiting concern for the operation and optimization of the PEM fuel cells. While the performance of the membrane depends on ample humidification, liquid water in the microporous layer, gas diffusion layer (GDL), and/or gas delivery channels impedes the flow of reactant gases to catalyst

sites and cripples cathodic reaction rates. Two-phase flow phenomena have been identified as concerns for flooding-induced performance degradation, cell voltage hysteresis, increased parasitic pumping losses, and the absence of predicted performance improvements [1-5].

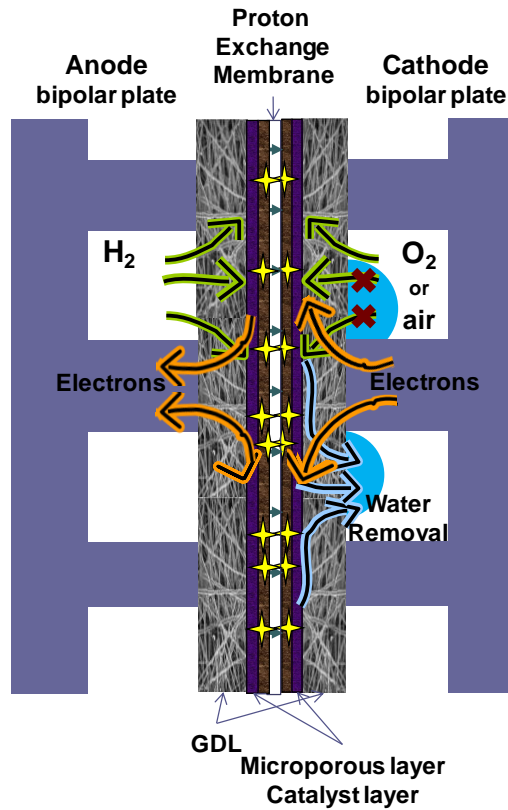


**Figure 1.1: Transport processes in a PEM fuel cell.**

While microchannels are proposed for use in PEM fuel cells with promised benefits of increased convective transport, flexibility of geometric design, and decreased resistive path lengths, these benefits have not been realized in practical systems [6 7]. One explanation for the unrealized performance improvements is an increased

propensity toward flooding in smaller channels where surface tension force becomes significant compared with viscous, inertial, and pressure forces [8].

The issue of flooding in the gas delivery channels of PEM fuel cells has been addressed in various ways, from in-situ and ex-situ imaging techniques (Section 1.3) to the development of novel designs and materials which provide wicking or pumping of liquid water from the electrode areas [9-11]. Yet the optimal design of fuel cell channels requires clear understanding of the interactions of air and water in small diameter channels. While many studies have considered the flow in small diameter tubes (Section 1.2), there remains a need for studies that consider two-phase flow in microchannel geometries that mimic conditions in fuel cell channels, where rectangular cross-sections, long channel lengths, distributed water introduction, and porous walls are defining characteristics. The present work uses experimental methods to study the physics of two-phase flow in geometries common to practical fuel cells which is critical to their performance.

## **1.2 Two-phase flow fundamentals**

Fluids moving through confined spaces such as microchannels experience a variety of forces, with body forces becoming less important relative to surface forces as the dimensions of the channels become small. In two-phase flow, surface tension at the air-water interface becomes an important parameter in the behavior of the fluid phases. The interplay of forces and geometry determine the structure and behavior of the air-

water interface, which can have a very important effect on the operation of a fluidic device.

The Navier-Stokes equations describe the momentum balance in each phase. For simplicity, the momentum balance is often expressed for two-phase flow in terms of the *Integral Momentum Equation*, which accounts for the viscous forces in the gas phase, the liquid phase, and at the interface.

$$-\frac{\partial P}{\partial x} = \tau_G \frac{S_G}{A_G} + \tau_L \frac{S_L}{A_L} + \tau_i \frac{S_i}{A_i} + \text{inertial} \quad (1)$$

where  $S_G$  and  $S_L$  are the wetted perimeters of the wall with the gas and liquid phases respectively,  $S_i$  is the perimeter of the gas-liquid interface in the cross-section,  $A_G$  and  $A_L$  are the cross-sectional areas of the gas and liquid phases,  $A_i$  is a cross-sectional area defined according to the particular formulation of  $\tau$ , where  $\tau_G$ ,  $\tau_L$ ,  $\tau_i$  are shear stress coefficients.

Yet this simple expression masks the complexity of definition of the appropriate shear stress coefficient,  $\tau$ , which must account for the configuration of the phases within the flow. Analytical predictions of these coefficients are not available, but some empirically and theoretically derived expressions have been presented in the literature [12]. A few studies have attempted to derive phenomenological expressions for the pressure drop in the channels based on flow regime physics [13 14], but these models have not been widely adopted as they require more detailed knowledge of the flow structure.

Surface tension forces can be important at the interface between the gas and liquid phases. In momentum and energy equations, surface tension forces are accounted for

at the boundary between the forces, where the curvature of the interface induces a pressure difference between the phases according to the *Young-Laplace Equation*,

$$\gamma C = P_1 - P_0 \quad (2)$$

where  $C$  is curvature of the interface,  $P_1$  and  $P_0$  are the bulk pressure on either side of the interface. At the contact line between the interface and the solid surface, a balance of forces dictates the equilibrium contact angle between the surface and the interface according to the surface energies of each interface, which is expressed as

$$\gamma \cos \theta_E = \gamma_{SO} - \gamma_{SL} \quad (3)$$

where subscript  $S$  refers to the solid phase,  $O$  refers to the gas phase, and  $L$  refers to the liquid phase.

Common flow structures in two-phase microchannels include intermittent regimes and separated flow regimes. In intermittent regimes, the air and water pass through the channel periodically and the liquid exists as discrete structures with a continuous or discontinuous gas phase around them; in this study, we refer to these regimes as ‘slug flow’ and ‘plug flow’, respectively. In separated flow regimes, the air flows through one region of the channel while water flows continuously through another region. A distinction is made based on to what extent the water covers the channel walls, with ‘annular flow’ corresponding to all walls covered, ‘stratified flow’ including one or two walls, and ‘dry’ meaning that water only flows in the corners of the channels.

Flow structure changes due to surface energy differences can occur stochastically, as the interface configuration spontaneously adjusts from one state to an energetically favorable state [15]. Surfaces that are not perfectly clean on a molecular level may

support a range of stable contact angles, bounded by advancing and receding contact angles, which are a function of surface characteristics and the fluid [16]. The effect of contact angle hysteresis has been shown to be significant in describing the motion of liquid plugs and slugs in gas flows in circular tubes and rectangular microchannels, and for droplets on flat surfaces [17-19]. Contact angle hysteresis has also been used to predict the departure of a droplet from a fuel cell gas diffusion layer [20].

Flow regimes are typically recorded on flow regime maps where superficial velocities of each phase are the key parameters, corresponding to the axes on the map. Many studies have examined two-phase flow in circular channels with diameters smaller than 1 mm, though the boundaries between the flow regimes do not all agree [21-30]. Some discrepancy is expected because the channel materials, geometries, and injection configurations are not consistent between experimental setups. These studies do not replicate the distributed liquid water introduction, long channel lengths, and porous boundary conditions of a PEM fuel cell. Additionally, the liquid flow rates of interest for these applications are much higher than those relevant to fuel cell operation. Pehlivan [31] provides a review of the two-phase flow regimes observed in mini channels as small as 800  $\mu\text{m}$ . His universal flow regime map based on experimental results from the literature does not extend to low water flow rates relevant for fuel cell channels. Nevertheless, air flow rate is the dominant parameter influencing flow regime transitions at the lowest reported water flow rates, a result which may be relevant for the lower water flow rates applicable to fuel cells.

In contrast with the number of studies in circular channels, very few studies have examined flow regime boundaries in rectangular channels, which are important for



practical devices. Only two studies present flow regime maps for rectangular cross-section channels with dimensions smaller than 1 mm [32 33]; these studies are discussed in more detail in Section 2.1. Chung et al. [33] performed similar experiments on channels with square and circular cross-sections of approximately 100  $\mu\text{m}$ ; they found a small shift in the flow regime boundaries between the two geometries. In vertically-oriented mini-channels of critical diameter less than 2.9 mm, Bi and Zhao [34] found that the flow through the corners of a rectangular channel caused different flow behavior than flow in circular channels where corner flow does not exist because of buoyancy effects. However, Garimella's models of slug flow in circular and square microchannels show a small difference in pressure gradient [35]. Perhaps the most important effect of the presence of corners in the cross-section is the potential establishment of capillary flow in the corner of the channel [36 37], which may have a significant effect on the fluid interactions depending on flow conditions. These effects are still not well understood.

The effects of surface properties on the flow have also not been systematically studied. In mini channels, two studies indicate that the wettability of the surface has a small effect on the observed flow regimes for moderately non-wetting materials, however for highly non-wetting surfaces, the effect becomes important [38 39]. In 1 mm square channels exhibiting annular flow, the effect of changing the surface tension of the liquid on the pressure drop was not significant [40], however this result may not apply to intermittent flow regimes where the triple point is expected to play a more significant role in the fluid-surface interactions.

## 1.3 Liquid water visualization in PEM fuel cells

Because water in the cathode channels of a PEM fuel cell can significantly impact its operation and two-phase flow is generally not well characterized in geometries relevant to fuel cells, various authors have developed techniques to visualize two-phase flow in actual and replicated fuel cells [41–42].

### 1.3.1 *In-situ*

Some two-phase flow characterization tools have been developed for in-situ fuel cell applications. In fuel cell components lacking optical access, neutron imaging, magnetic resonance imaging, and x-ray tomography allow for identification of liquid water through opaque surfaces. Neutron imaging is a promising technique for imaging of liquid water in an operating fuel cell [43–45]. Neutron radiography is basically a two-dimensional technique, requiring detailed analysis to distinguish between the anode and cathode. Boillat et al. have developed a system optimized for fuel cell imaging which has a resolution of 20  $\mu\text{m}$  in-plane and 200  $\mu\text{m}$  axially with an exposure time of 10 seconds by mounting the cell at a steep angle [46]. Studies by Pekula et al. and Li et al. show the accumulation of water at the corners of serpentine channels [47–48]. Owejan et al. and Zhang et al. have used neutron radiography to show the effect of GDL materials on the accumulation of water in operating fuel cells [49–50]. Neutron tomography allows for differentiation between cells within a stack, however it is a very time-consuming technique, requiring hours to collect a set of images [51–52]. The study of a fuel cell stack revealed less water accumulation in internal cells, likely due to thermal effects. X-ray imaging has captured the formation

of droplets and air-water interfaces with high resolution in single cells [53 54]. X-ray tomography and magnetic resonance imaging have been used to create three dimensional maps of the water concentration in the membrane and GDL layers with limited resolution [55 56].

Opaque bipolar plates, layers of porous materials with various surface properties, and non-uniformity of water production rate and location complicate the imaging and analysis of flow regimes in fuel cell channels. Yet fuel cells with modified geometries allow optical access into the gas distribution channels [57 58]. These cells have been used to correlate the appearance of liquid water with increases in gas pressure in the channels and voltage drops in the fuel cell [59-61]. Air flow rate is found to be a critical parameter affecting or preventing flooding [62 63]. In contrast to reported results of neutron imaging, Ous [64] observed water accumulation in the center of the channels, away from the corners. Kimball et al. [62] monitored the emergence of droplets in the channel and their subsequent coalescence and slug formation leading to flooding; the larger channels in their study exhibited gravity-dependent behavior. Spornjak's [65] results indicated that the materials, such as the microporous layer, have a significant effect on water appearance in the channels. In general, optical setups may interfere with typical reaction distribution because the electrical pathways are distorted when conductive bipolar plates are replaced with non-conductive glass plates for optical access. While much insight can be drawn from these studies in the correlation between liquid water and fuel cell performance, the precise flow conditions at any particular location in the cell are difficult to quantify due to non-uniformities in reaction distribution and subsequent uncertainties in local flow rates. The

discrepancies between these studies highlight the complexity of the interactions of the electrochemical and fluidic processes in fuel cell devices.

### **1.3.2 *Ex-situ***

Ex-situ experiments are proposed as a means of decoupling the electrochemistry from the fluidic system, allowing the physics of the two-phase flow to be examined with materials relevant to fuel cell systems without the added complexity of the operating system. However, the ex-situ experiments provide their own challenges for implementation and interpretation.

Comparison of in-situ and ex-situ experimental results is complicated by the definitions commonly prescribed in the literature for given operating conditions. A single stoichiometric ratio is often reported, but in reality the air flow rate is held at a fixed value and the current density or cell load is swept through a range of operating conditions. Therefore, the reported stoichiometric ratio is valid at only a particular representative current density. This procedure allows for similar fluidic conditions in each case however, the electrochemical activity and species concentration profile along the channel varies as more or fewer reactants are consumed. Despite these difficulties, ex-situ experiments offer the advantage of greater control of experimental conditions. Absent the electrochemistry of an operating fuel cell, these setups allow observation of the two-phase flow characteristics in fuel cell geometries while quantifying the local flow rates of both phases.

Various geometric configurations have been employed which simulate the conditions of a fuel cell in an ex-situ visualization experiment. Lu et al. [66] and

Zhang et al. [67] constructed parallel-flow systems with gas and liquid injection relevant to fuel cell conditions. Su et al. [68] studied flow in 5 mm square cathode channels by injecting water into the channels through a carbon paper layer from a single liquid reservoir, resulting in a lot of flow field flooding and water in the GDL and channels. Others have examined droplet departure from a GDL into a gas channel using short channel segments [69 70]. Gao et al. [71] used confocal microscopy to observe the emergence and coalescence of droplets as they emerge from a GDL surface.

Few experimental studies have considered fuel cell flow conditions in microchannels, which is significant as two-phase flow transitions are commonly considered to be functions of the superficial velocity of the phases. While flow rates in fuel cell channels are fixed by the current density and stoichiometry, flow velocities are then determined by channel dimensions. Many relevant non-dimensional parameters, such as Weber and capillary numbers, corresponding to the ratio of inertia and viscosity to surface tension, respectively, are often expressed in terms of superficial velocities. For fuel cell systems, where volumetric flow rates are fixed by operating conditions, the dimensions of the channel have a significant effect on these forces. Lee [72] constructed a GDL-integrated microchannel structure in which plug flow, annular and stratified flows are observed, depending on the Weber and capillary numbers of the two-phase flow.

## **1.4 Overview of this work**

This study examines two-phase flow in microchannels with rectangular cross-sections in order to gain insight into the physics of the interaction of air and water phases in rectangular microchannels applicable to practical devices, especially PEM fuel cells. In Chapter 2, fundamental aspects of two phase flow in microchannels of various aspect ratios are examined; flow structures are characterized on flow regime maps and compared with previous results. In Chapter 3, stratified flow, a commonly observed flow regime during the current study, is examined in more depth. Measurements of the film thickness of the stratified flow are compared with an analytically-based model of the flow. Chapter 4 describes the evolution of flow structure along the length of an ex-situ PEM fuel cell channel with distributed introduction of water into the channel through a porous GDL paper wall. Finally, Chapter 5 provides new insight into the use of confocal imaging techniques for the visualization of two-phase interfaces.

# **Chapter 2. Fluorescent visualization of two-phase flow regimes in rectangular microchannels**

## **2.1 Motivation**

Despite the importance of predicting the flow structure in microchannels of various geometries in order to optimize the performance of practical devices, previous visualization studies of two-phase flow in microchannels are restricted to channels of circular, square, or triangular cross-section with asymmetric pre-mixed injection conditions. This study examines flow regimes in channels with rectangular cross-sections of various aspect ratios and sizes with asymmetric water injection into the channel from one side wall injection location.

Microfabricated silicon microchannels replicate those found in PEMFC gas delivery systems, while water injected into the channels simulates liquid entering the cathode channel due to chemical reaction and electro-osmotic drag. This approach allows for a controlled water “production” without the unsteady, non-uniform behavior of actual fuel cell reactions. This is of particular importance to decouple the problem of water entrainment into the microchannels.

Two previously published visualization studies on two-phase flow in microchannels with square cross-sections present flow regime maps as shown in Figure 2.1 [32–33]. Both of these studies were performed on channels with axisymmetric injection conditions, where the air and water are mixed upstream of the test section. The flow regime data are summarized on a flow regime map where the axes represent the flow rates of air and water expressed as superficial velocities and the symbols correspond to the flow structure which was identified at these flow conditions. Generally, both sets of data show intermittent flow regimes (bubbly, wedging, and slug) occurring for low air flow rates, with separated flow regimes (annular and dry) prevailing at higher air flow rates. Despite this general agreement, discrepancies between the two flow regime maps exist at the boundary between the intermittent and stratified flow. In the smaller, shorter channels of Chung's paper, slug flow persists at higher air flow rates for a given superficial water velocity.



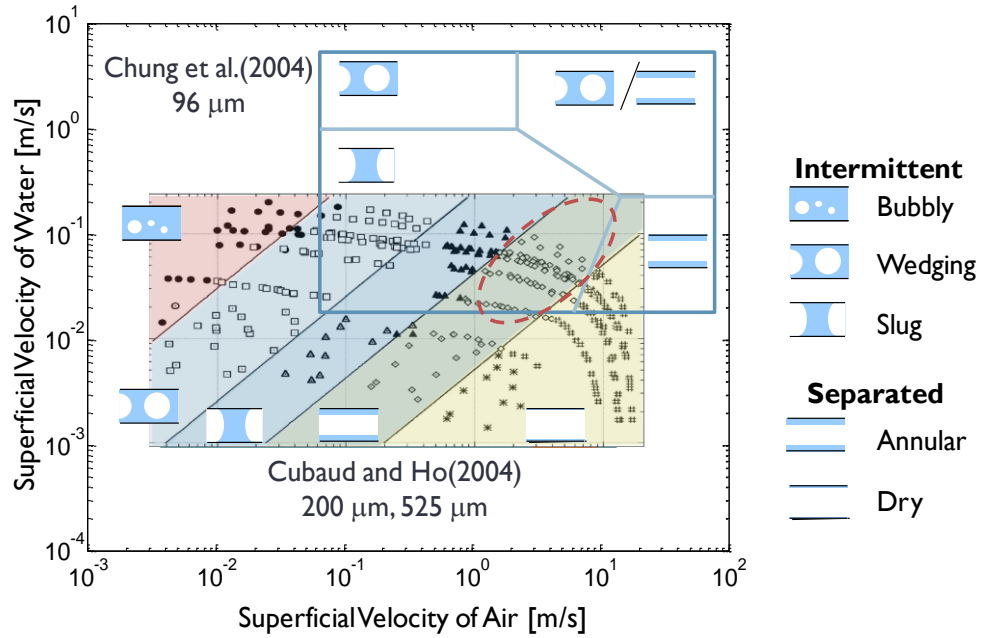


**Figure 2.1: Flow regime maps from previous visualization studies in square cross-section microchannels. Data points and shaded areas from Cubaud and Ho [32] are displayed on the figure, while Chung [33] data is simplified to the outlined regions. The region of discrepancy between these two regime maps is marked with a dashed circle.**

The data presented in this section and the next section corroborates and extends the flow regime boundaries suggested by previous studies, especially those shown by Cubaud and Ho. This work extends the body of flow regime data to include channels with rectangular cross-sections of various aspect ratios and with asymmetric side-wall injection conditions.

## 2.2 Experimental Method

### 2.2.1 Microfabricated experimental structures

The test structure layout is shown in Figure 2.2. A silicon wafer is processed with Deep Reaction Ion Etching (DRIE) to create channels, injection slots, and through holes for fluidic connections. A glass cover slide is anodically bonded to the wafer in order to seal and provide optical access to the channel [73]. Several channel layouts were employed for various tests. A summary of channel specifications is given in Table 2.1. All channels have a water injection slot on the side wall of the channel. The water injection slot intersects the channel at a right angle to the flow direction in the channel. The water injection slot is as deep as the channel. Channel depth is controlled by the etching time and is verified post-processing using a confocal microscope for depth measurement.

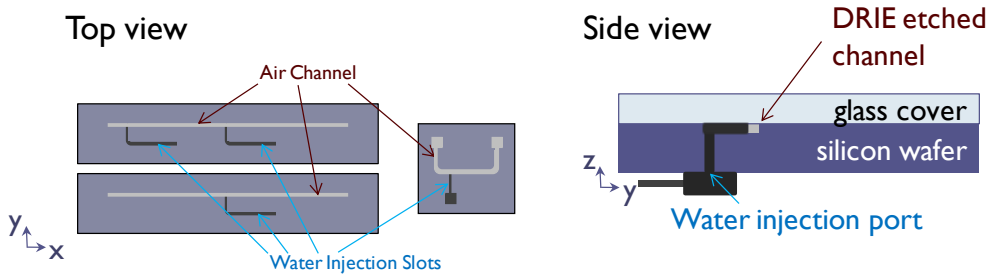


**Figure 2.2: Layout of channel structures.**

**Table 2.1: Channel Geometries**

<b>Symbol</b>	<b>Type</b>	<b>Width</b>	<b>Depth</b>	<b>Length</b>	<b>Needle Valve</b>
<b>Color</b>		<b>(<math>\mu\text{m}</math>)</b>	<b>(<math>\mu\text{m}</math>)</b>		<b>Location</b>
Green	U-shaped	50	45	2.5 cm	Downstream
Orange	Straight	103	95	6 cm	Upstream
Red	U-shaped	500	400	2.5 cm	Downstream
Blue	U-shaped	500	45	2.5 cm	Downstream
Purple	Straight	430	240	6 cm	Upstream

### 2.2.2 *Experimental apparatus*

Figure 2.3 shows the setup for controlling experimental parameters. The test structure is placed glass-side down on an inverted microscope. Fluidic connections are made on the backside of the chip with 1/8" OD (1/16" ID) Teflon tubing. Connections between tubing segments and measurement devices are made with Swagelok and Legris connectors; all connections are leak tested and efforts are made to eliminate bubbles from the system.

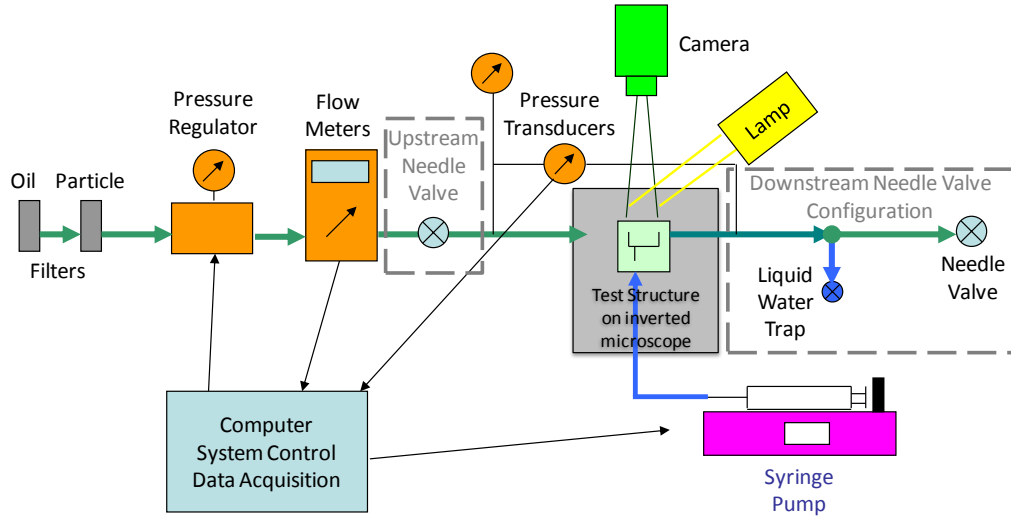


**Figure 2.3: Schematic of experimental setup. Dotted boxes mark the two alternate configurations used to control pressure drop across the chip as described in the text.**

A differential pressure transducer in-line parallel with the chip measures the pressure drop across the microchannel. Compressibility calculations verify that the error introduced by the contraction of the flow path from 1/8" OD Teflon tubing to the rectangular channel is negligible. For the U-shaped channels, the air flow rate is varied by adjusting a downstream needle valve under choked flow exit conditions. Tubing lengths downstream are minimized to reduce settling time between exit pressure conditions when the needle valve is adjusted. For the straight channel experiments, the downstream tubing and needle valve was replaced by a wicking material placed near the outlet to remove liquid more directly at the exit because it was observed that droplets in the outlet tubing were inducing fluctuations in the channels for the unsteady flow regimes observed under these flow conditions. These fluctuations were not observed for the steady flow which occurred in the U-shaped,

high aspect ratio channels. The air flow rate is measured using either a thermal mass flow meter (Sensirion EM1) or a laminar flow meter (Omega FMA 1601A, 0-10 ccm, 0-1 LPM, or 0-2 LPM), depending on the range of flow rates.

Images of the flow are captured with a CCD camera through the magnifying objective on the inverted Nikon microscope.

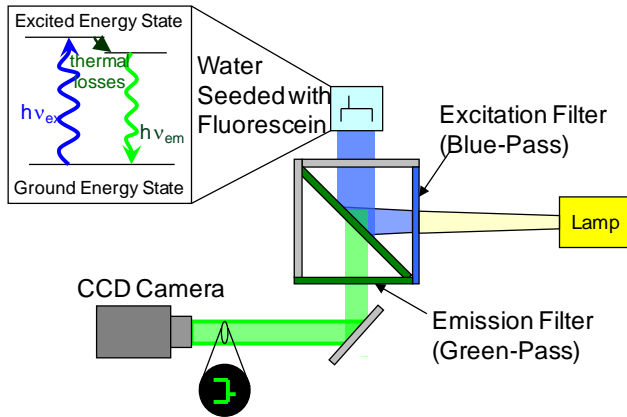
### ***2.2.3 Fluorescent imaging technique***

Fluorescent imaging provides detailed information about the flow regime and water film extent within the channel. Water injected into the channels is seeded with a 0.5 mMol concentration of Fluorescein dye to enable fluorescent visualization of the flow. Fluorescent excitation is achieved with a broadband metal halide lamp combined with an FITC filter cube on an inverted microscope as depicted in Figure 2.3. As shown, fluorescence imaging makes the air/water interfaces more clearly distinguishable and easily post-processed than with white light imaging. Figure 2.4 is a comparison of white light and fluorescence imaging of the injection region for a stratified flow in a microchannel.

Images are recorded using one of two CCD cameras. The CoolSNAP ES camera, with 1392 x 1040 pixels measuring 6.45  $\mu\text{m}$  each, allows for high resolution imaging. A 10x objective lens allows a 500  $\mu\text{m}$  channel width to be captured in a single image, with each square pixel corresponding to a 0.645  $\mu\text{m}$  by 0.645  $\mu\text{m}$  region, for 800 pixel resolution across the channel width. The Phantom v7.3 camera is a high speed camera, which is capable of capturing 6688 full 800 x 600 pixel frames per second. With a pixel size of 22  $\mu\text{m}$ , the resolution of this camera is significantly lower; however the

high speed capability can capture the high speed formation and motion of small flow structures in the channel. The high resolution camera is used for high-aspect ratio U-shaped channels where the flow is steady and stratified. The high speed camera is used for the more square channels, where the flow is sometimes intermittent with high speed features. Images are collected along the length of the channel by translating the microscope stage manually. For the long, straight channel, images of the stage position are collected simultaneously so that spatial variations in the flow can be correlated with their position along the channel.

### Fluorescent Imaging Principle



### Sample Images

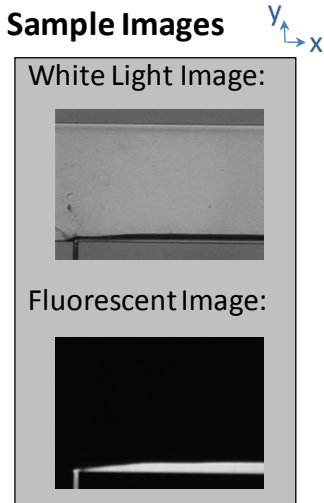


**Figure 2.4: Schematic of fluorescent imaging principle.** The dye molecules are excited by light of blue wavelengths. After thermal losses, the molecules emit light in the wavelength range of green light. An emission filter insures that only this emitted light is captured by the camera. In the resulting images, only the water appears bright, all background features are hidden. The sample images here show the injection region of a stratified flow in a microchannel.

## **2.3 Procedure**

Air flow conditions are established by setting the inlet pressure and/or adjusting the outlet needle valve. Water is introduced into the channel by starting the syringe pump, which has been carefully evacuated of air pockets and bubbles in the tubing. The flow structure is imaged once a steady condition has been achieved, as determined when air flow rate and pressure readings are not changing. The system was configured to reduce compressibility and steady conditions were established quickly. Measurements were typically recorded 30 – 60 seconds after the conditions were set. Water flow was stopped until the channel and tubing were cleared of residual liquid, then the next test conditions were established.

Measurements of pressure and flow rates were averaged off-line over the duration of the experiment. The uncertainty in the velocity measurement is derived from the quoted accuracy of the mass flow meters and channel geometries. The thermal mass flow meter has a quoted accuracy of  $\pm 3\%$  measured value. Velocities calculated from the thermal mass flow meter readings are reported with an accuracy of  $\pm 6\%$  MV, including uncertainties in the channel depth and air density from the pressure measurement. The uncertainty in the liquid velocity is due to the compressibility of the system and uncertainty in the volume flow rate of the syringe pump and the channel dimensions. The uncertainty is approximated as  $\pm 2\%$ , dominated by the measurement of channel dimension. The images and videos were examined after the experiments in order to categorize the observed flow structures.

As previously noted, the channels are etched in silicon using DRIE. This technique produces several effects which may impact the surface energy and topology of the

silicon. The etched walls can be scalloped, though efforts are made to reduce this effect according to the recipe used. There can also be residual coatings left on the surface of the channel which may impact the contact angles in the channels. This coating is persistent and difficult to remove, so it is assumed that all channels used for these experiments have similar surface properties.

## 2.4 Results and Discussion

### 2.4.1 *Flow Regime Maps*

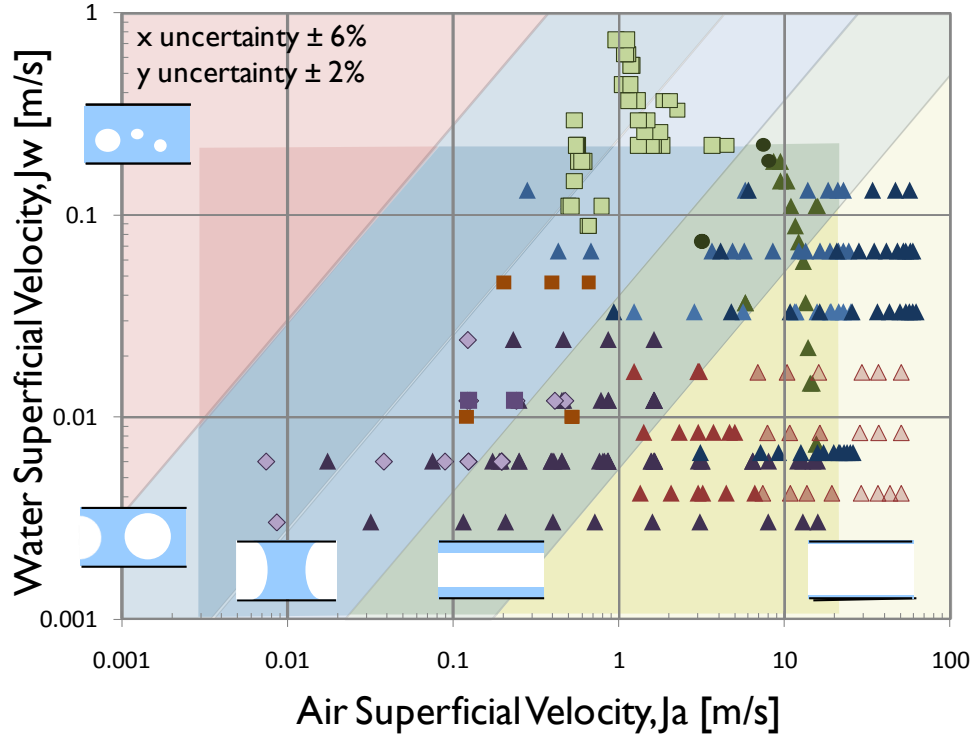
Flow structure data from the five types of channels examined in this study are summarized in Figure 2.5. This chapter provides more details about the specifics of the flow regimes summarized on this regime map. The data from the current study is overlaid with shaded regions which correspond to the boundaries of the study presented by Cubaud and Ho [32], with the darkly shaded region corresponding to the limits of that study and the lightly shaded area extending the power law transition criterion to higher air and water superficial velocities.

In Cubaud and Ho's study, flow regimes in square cross-section channels are reported for two different channel sizes. The flow structure regions are divided by power law relationships of superficial air and water velocities, shown as parallel lines on log-log axes of superficial velocities. As the ratio of air to water velocity increases, the flow regimes progress through the following sequence:



- bubbly flow – small air bubbles exist in a primarily liquid flow
- wedging and slug flow – large air bubbles spatially intermittently fill the channel. Cubaud makes a distinction between these two regimes, citing the presence of a thin liquid film around the air bubble in wedging flow; the absence of which yield slug flow. In this study, we group these flow regimes together into a single category of intermittent flow, named plug flow.
- annular flow – a gas core is surrounded by liquid film on the walls
- dry flow – liquid flows only in the corners of the channel and the walls of the channel are dry.

Four distinct flow regimes were observed in the channels under the range of conditions tested. In most cases, a single flow regime is observed along the length of the channel. Plug, annular, and stratified flows are marked with square, circular, and triangular symbols, respectively. Under certain flow conditions, instability in the film causes transition from stratified flow to plug flow downstream of the water injection. This transitional regime is also noted on the flow regime map in as diamond shaped symbols.



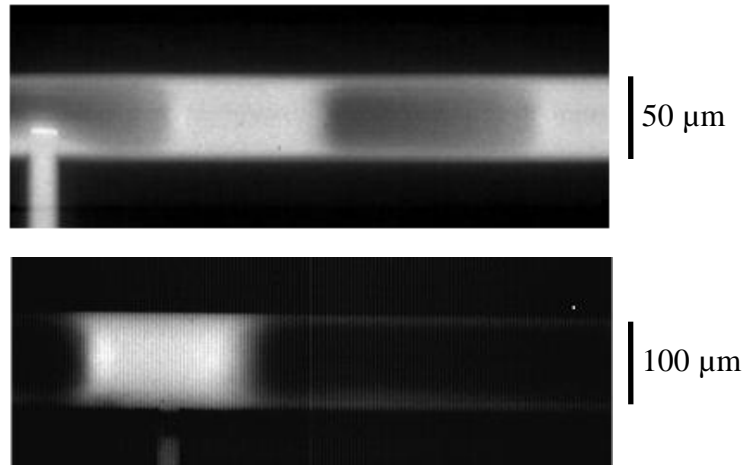
Symbol Shape	Observed Flow Regime	Symbol Color	Channel Dimensions
	Plug	Green	50 x 45 $\mu\text{m}$
	Annular	Orange	103 x 95 $\mu\text{m}$
	Stratified	Red	500 x 400 $\mu\text{m}$
	Transition	Blue	500 x 45 $\mu\text{m}$
<b>Shaded Areas:</b> Published Reference		Purple	430 x 240 $\mu\text{m}$

Figure 2.5: Flow regime map for five types of channels of various dimensions and aspect ratios. Data from the current study are presented overlaid with the regime boundaries published in [32]. The more darkly shaded region corresponds to the actual boundaries of the published study; the lightly shaded region extends these transition criteria to encompass the data of the current study.

General analysis of the flow regimes indicates overall agreement of the current data with the flow regime map presented by Cubaud, particularly in the nearly-square cross-section channels, where intermittent flow regimes (shown as square and diamond markers in Figure 2.5) generally fall within the blue shaded region. On the other hand, stratified flow regimes, which were not observed in Cubaud's study, are present under a broad range of conditions in these studies. Because of the prevalence of stratified flow in these channels, a detailed examination of the physics of this flow structure is performed in Chapter 3.

### **2.4.2 *Plug flow***

The current results corroborate the boundaries of superficial velocity conditions which result in plug flow formation in square cross-section microchannels proposed by Cubaud for channels of smaller dimension. The original study used channels with side lengths of 200  $\mu\text{m}$  and 525  $\mu\text{m}$ , this study reports plug flow in 50  $\mu\text{m}$  and 100  $\mu\text{m}$  channels, under the same superficial velocity conditions as reported for the larger channels. This agreement corroborates the use of this superficial velocity metric for flow regime mapping of air-water flows. Figure 2.6 shows representative images of plug flow in the 50  $\mu\text{m}$  and 100  $\mu\text{m}$  channels.



**Figure 2.6: Representative images of plug flow in 50  $\mu\text{m}$  and 100  $\mu\text{m}$  square channels. Flow is left to right, water appears bright in the image and enters the air channel from the injection slot on the bottom of the image. These images are captured with the Phantom v7.3 high-speed camera.**

### ***Plug formation at inlet***

Figure 2.7 shows the formation of a plug at the water injection slot on the side of a 100  $\mu\text{m}$  square channel. As water is injected, the liquid grows laterally as a film nearly symmetrically distributed about the injection location. Then at some instant, the film bulges and quickly deforms toward the opposite wall wicking water from the film that had spread laterally and forming a plug which spans the channel height, but is narrower than the film had been. The plug then moves downstream, growing in size until it detaches from the water injection location and moves downstream. The process repeats cyclically. In the sample case shown in Figure 2.7, the growth of the film after the previous slug had detached occurs over approximately 16 frames (5.33

ms), the rapid deformation occurs in less than 2 frames (666  $\mu$ s), and the slug grows while attached to the water inlet during 7-8 frames (2.33-2.66 ms).

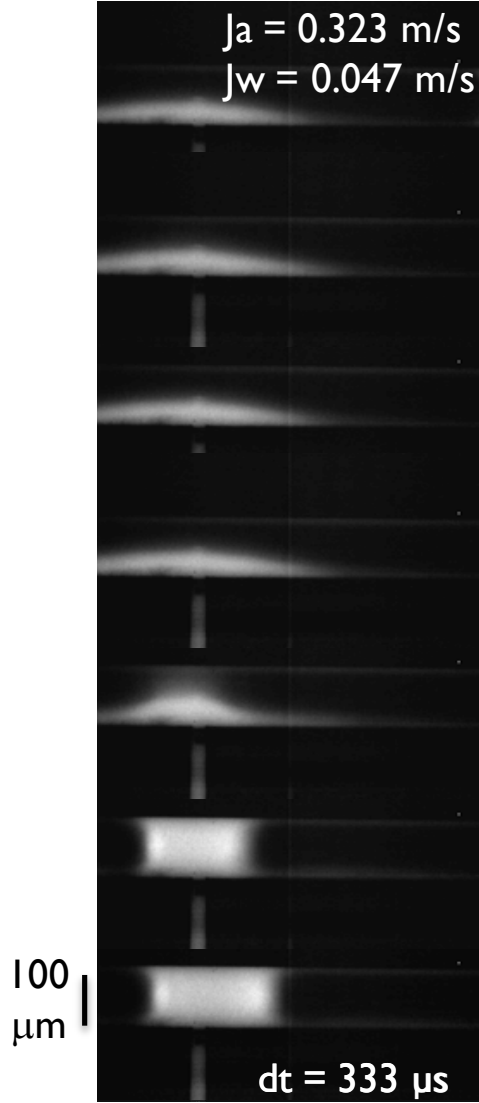


**Figure 2.7: Seven consecutive frames of high-speed images of plug formation at water injection inlet of 100  $\mu\text{m}$  square channel.**

This phenomena is similar to the transition discussed by Gauglitz et al. [74] for the spontaneous formation of liquid ‘lenses’ from an annular film around the perimeter of

a circular microchannel. Gauglitz identifies a thickness based transition criterion which corresponds to the geometry where it is energetically favorable for the liquid to exist as a “lens” or “plug” rather than an elongated disk. At this point, the liquid becomes unstable and may spontaneously transition to a stable geometry. Gauglitz predicts a critical thickness at which an annular film in a circular microchannel becomes unstable at 12% of the channel radius; reported empirical results give a critical film thickness of 9%. A similar measurement is carried out for several cases of plug formation in the current geometry, which differs significantly from the previous studies because of the following properties:

- The channel cross-section is rectangular
- Water is injected from the side wall and significant shear forces exist at the air water interface
- The film is discontinuous film at the water injection location after the previous plug moves downstream

The film thickness just before transition to plug is measured as 33% of the channel height. There exists a need for further investigation into the conditions for the formation of plug flow at a side wall injection, including considerations of the effect of air shear and inertial forces on the plug formation, the critical film spreading length for formation of a plug, as the water in this spreading air provides the necessary volume of liquid required to create and sustain a plug across the channel, and lift

forces due to the acceleration of the gas phase through the constriction caused by the liquid slug.

### ***Plug formation from film instability***

A similar yet distinct means of plug formation was observed in a transition from a stratified film. This phenomenon is marked in Figure 2.5 as diamonds. This regime occurs in the conditions on the flow regime map where Cubaud observed plug flow, but in the current experiments in the 430  $\mu\text{m}$  x 240  $\mu\text{m}$  channels, we have observed either stratified flow or this transitional flow regime between stratified and plug flow. More discussion of this result is presented in the following section.

Figure 2.8(a) shows consecutive frames from high-speed images of the instability of a film forming a plug which then travels downstream. A small disturbance in the film is amplified and grows to fill the channel, while the water is wicked from the film adjacent to the disturbance, creating a local depression in its profile. This process looks notably similar to a known instability in stratified flows in macroscale tubes, the Kelvin-Helmholtz instability. The illustration from Taitel's paper [75] is shown in Figure 2.8(b). Taitel described the phenomena and developed a stability criterion based on a linear analysis of the stability of the momentum equation to small perturbation in film thickness for a two-phase system where inertial and gravity forces dominate [75]. The criterion is given by

$$g \leq \frac{\rho_G}{\rho_L} \left( \frac{W_G}{\rho_G A_G} \right)^2 \frac{A'_L}{A_G} \quad (4)$$

where  $A'_L$  is the perturbation to the liquid-phase area,  $A_G$  is the gas-phase area, and  $W_G$  is the mass flow rate of the gas phase. Other researchers have investigated this phenomenon in macroscale channels using non-linear stability analysis and including viscous effects [76-79].

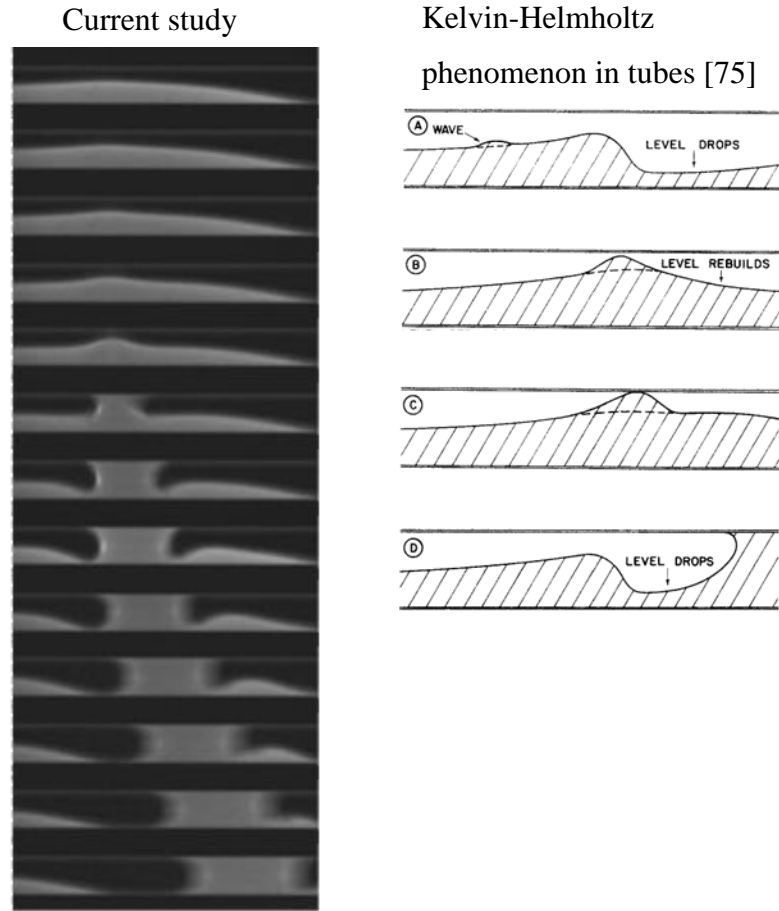


**Figure 2.8: (a) Images of the formation of a plug from a disturbance in a stratified film in a 430  $\mu\text{m}$  x 240  $\mu\text{m}$  channel. The time between images is 500  $\mu\text{s}$ . ( $J_{\text{air}} = 0.20$  m/s,  $J_{\text{water}} = 0.006$  m/s) (b) The process of slug formation by Kelvin-Helmholtz instability in a pipe as illustrated by Taitel and Dukler [75].**



Previous workers have not reported stratified flow in gas-liquid microchannel flow, therefore the stability of these flows and the formation of plugs from these films have not been studied. In microchannel flows, the effect of surface tension must also be considered with viscous and inertial forces creating lift around the disturbance. When surface tension is significant, a minimum radius of curvature is a likely criterion, while lift forces suggest a criterion related to the film thickness deviation, and viscous dissipation may dictate a minimum film thickness. More research is needed to complete a full stability analysis on this system.

### 2.4.3 *Annular flow*

An annular flow regime is observed only under a few conditions tested in the 50  $\mu\text{m}$  x 50  $\mu\text{m}$  channels. These points are marked in Figure 2.5 as circles and fall within the region where Cubaud also observed annular flow. The conditions where annular flow is observed in the current study are clustered close to the boundary with the plug flow regime. At higher air flow rates -- moving to the right on the regime map -- the current geometry favors stratified flow over annular flow.

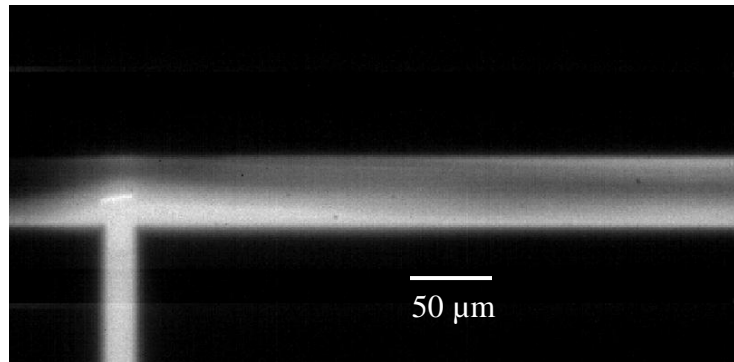


**Figure 2.9:** Image of the formation of annular flow at the water inlet in a 50  $\mu\text{m}$  x 50  $\mu\text{m}$  square channel.

The process of formation of annular flow can be seen at the water injection location. Under the conditions where annular flow exists, water can be seen entering the channel from the injection location and starting to protrude into the channel, feigning formation of a plug. Rather than forming a cohesive plug, however the surface tension of the water is not strong enough to overcome the inertial force of the air. The liquid plug is broken and water is forced to the walls and corners of the channel. Gas flows through the core, creating an annular flow.

The non-dimensional parameter which characterizes the relative magnitude of internal forces to surface tension forces is the Weber number. The gas phase Weber number formulation is given in Equation (5). The 1<sup>st</sup> order dependence on channel diameter comes from the derivation of the Weber number, where the inertia of the gas phase acts over the channel area, while surface tension is a line force which acts along the interface.

$$We_G = \frac{\rho_G U_G^2 D}{\sigma} = \begin{cases} 4 - 8 & \text{tubes in microgravity [80]} \\ 0.01 - 0.05 & \text{current data in } 50 \text{ } \mu\text{m} \times 45 \text{ } \mu\text{m} \\ & \text{rectangular channels} \end{cases} \quad (5)$$

Previous studies on two-phase flow in small tubes in microgravity have experimentally determined that a gas-phase Weber number between 4 and 8 describes the minimum gas flow which causes a transition from plug flow to annular flow [80]. In these 50  $\mu\text{m}$  x 45  $\mu\text{m}$  channels, the critical Weber number, measured experimentally, is in the range of 0.01 to 0.05. This small value denotes that a much lower flow rate of air is required to overcome the surface tension of the liquid phase in these rectangular microchannels. The data of Cubaud also demonstrates transition at a

gas-phase Weber number which is up to ten times larger than the current study. The data of Chung [33] transitions at a Weber number around 2, though Chung's data is collected at a higher water flow rate than the current study and that of Cubaud [32]. We find that the current study and Cubaud's study are both more susceptible to transition to annular flow and allow a significantly smaller amount of air to break apart plug flow than predicted by Zhao [80] or seen in Chung's study.

#### ***2.4.4 Stratified flow***

Stratified flow is observed in channels of all dimensions and aspect ratios in this study. For clarity, the stratified flow points on the regime map are shown in Figure 2.10, along with schematics of the cross-sectional shape and relative size of the channels in which stratified flow was observed.

This represents the first time that stratified air-water flow has been identified in square microchannels, especially those as small as  $50\text{ }\mu\text{m} \times 45\text{ }\mu\text{m}$ . The appearance of stratified flow in these channels is attributed to the asymmetric side-wall injection conditions of the current experiment. This flow structure appears under the air-water flow conditions that correspond to annular and dry flow regimes on Cubaud's map.

In the higher aspect ratio channels, the stratified flow structure dominates. This study represents some of the only reported flow regime data for high aspect ratio channels with air water flow and the results suggest that the high aspect ratio channel, in conjunction with the side-wall injection scheme, promotes flow stratification. As noted in Section 2.4.2, stratified flow exists under conditions when either annular or plug flow are expected to occur in the  $430\text{ }\mu\text{m} \times 240\text{ }\mu\text{m}$  channel. In the very high

aspect ratio channels measuring  $500\ \mu\text{m} \times 45\ \mu\text{m}$ , stratified flow persists well into the regime where plug flow is expected to occur according to the maps for square channels. These trends suggest a shift in the flow regime boundaries toward higher water flow rates or lower air flow rates for high aspect ratio channels.

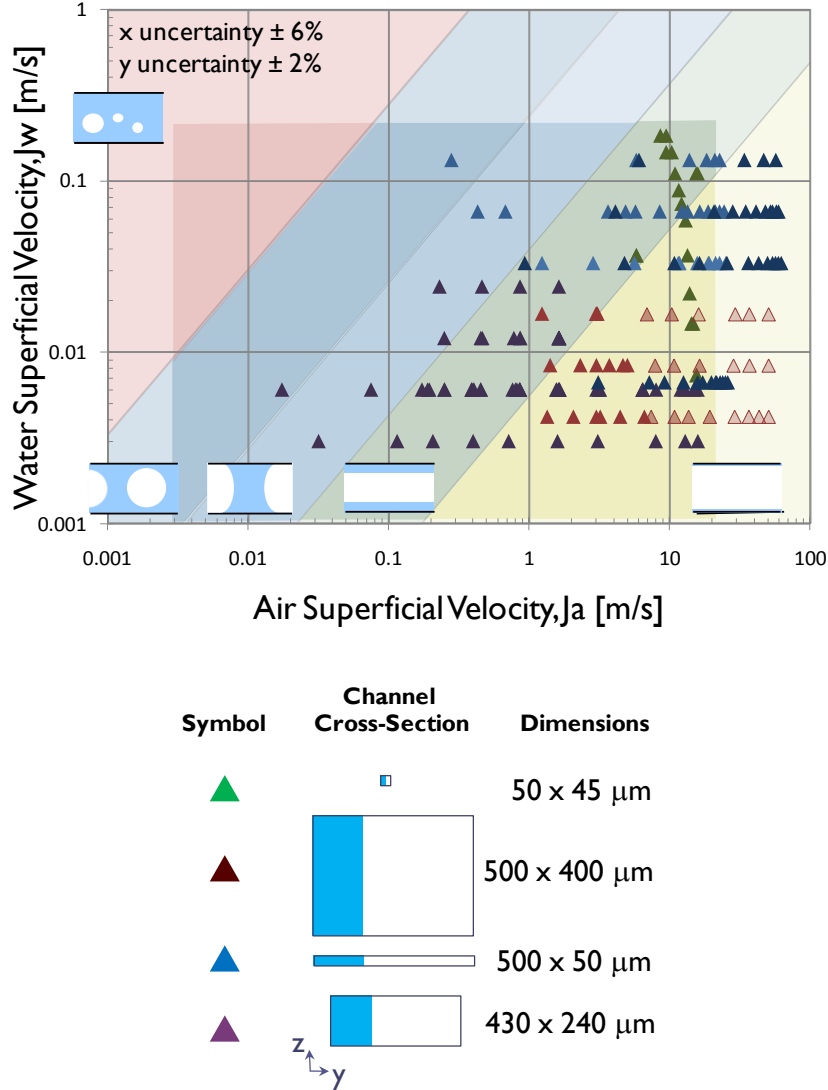


**Figure 2.10: Prevalence of stratified flow on the regime map and schematics of channel cross-sections in which it is observed.**

### **2.4.5 Conclusions**

Flow structure mapping for a variety of channel sizes and aspect ratios corroborates and extends flow regime maps presented in the literature for square cross-section channels. Plug, annular, stratified, and transitional flow regimes are identified, with stratified flow being both prevalent in high aspect ratio channels and previously unseen in square-cross section channels. Direction for further analysis of these results was presented.

## Chapter 3. Stratified flow physics

As described in the previous chapter, stratified flow was commonly observed in the rectangular channels with side-wall water injection used for the fundamental study of liquid-gas interactions in hydrophilic channels with side-wall water injection. This section develops a detailed study of the physics of stratified flow including presentation of an analytical model of flow supported by measurements of the structure of the stratified film for a variety of air and water conditions in channels of three different dimensions and aspect ratios. The measurement technique and some results have been published previously [81].

### 3.1 Analytical studies of stratified flow

An analytical solution to the velocity distribution in two-phase stratified flow in a rectangular duct is useful for gaining insight into the interaction of the air and liquid phases in the experiments. A solution was published in dimensional form by Tang and Himmelblau [82]. We build on this analysis to extract insight into the scaling arguments, ascertain validity limits for simplified models, and examine the effect of channel size and aspect ratio. Using an analytical solution, we can also examine

trade-offs relevant to fuel cell operation and predict preferable geometries and operating conditions.

A Fourier Sine transform is used to solve the incompressible Navier-Stokes equation for the velocity profile in each phase,

$$\nabla^2 V_i = -\frac{1}{\mu_i} \frac{\Delta P}{\Delta L}. \quad (6)$$

The geometry of the problem is depicted in Figure 3.1

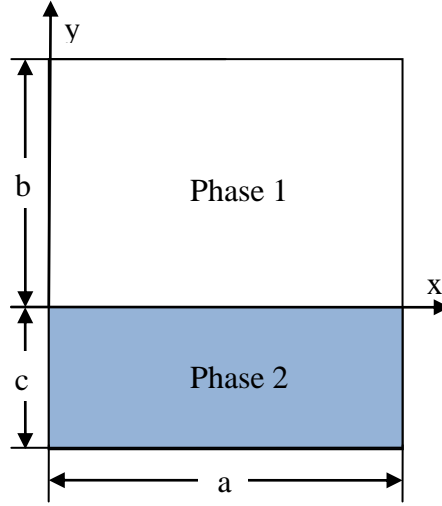


**Figure 3.1: Schematic of geometry for analytical solution**

The solution of the inverse transform is given by

$$w_i = \frac{2}{a} \sum_{n=1}^{\infty} \hat{w}_i \sin \frac{zX}{a}, \text{ where } z = \pi(2n+1) \quad (7)$$

where  $\hat{w}$  is the solution to the sine transform and has the form

$$\hat{w}_1 = A \sinh \left[ \frac{z(b-y)}{a} \right] + B \cosh \left[ \frac{zy}{a} \right] + \frac{2a^3(\Delta P/\Delta L)}{z^3 \mu_1} \quad (8)$$

$$\hat{w}_2 = C \sinh\left[\frac{z(c+y)}{a}\right] + D \cosh\left[\frac{zy}{a}\right] + \frac{2a^3(\Delta P/\Delta L)}{z^3 \mu_2} \quad (9)$$

for phase 1 and phase 2, respectively. The details of the solution and values of the constants are given in Appendix A.

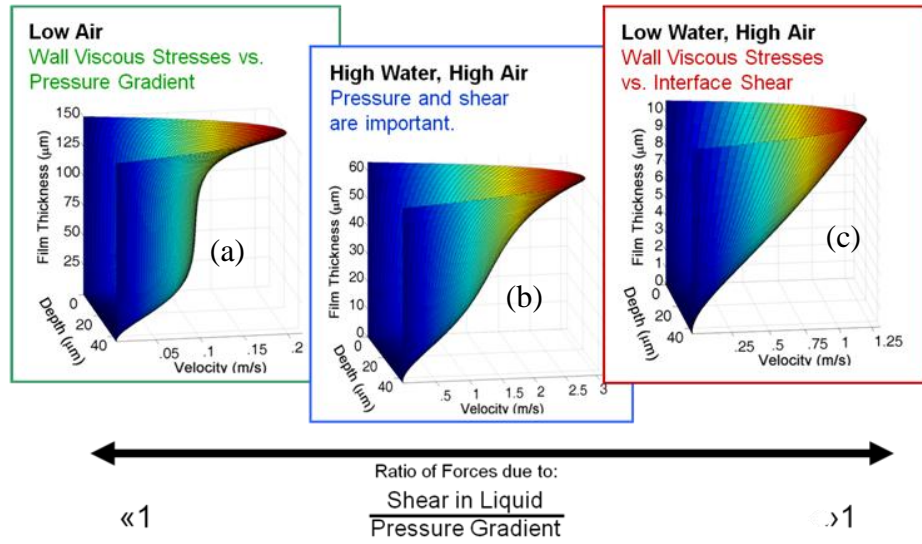


**Figure 3.2:** Velocity profile in liquid phase calculated from analytical solution to stratified two-phase flow in 500 x 45 μm rectangular microchannel. (a) a primarily pressure driven profile indicative of high water injection rates with low imposed air pressure drop (low air flow rates). (b) a combined shear-pressure driven profile as seen for both high air flow and high water flow rate conditions. (c) a shear driven profile as observed for high pressure drop (high air flow rate) low water injection rate conditions.

Velocity profiles obtained with the analytical solution show the effect of various forces on the liquid layer, with shear forces affecting the pressure driven flow significantly from the interface to a depth approximately equal to the width of the



channel. Figure 3.2 shows representative velocity profiles in the liquid film of a co-current air-water film. The profiles are obtained with an analytical solution which is calculated for the experimentally observed pressure drop / film thickness conditions. Figure 3.2(a) shows a case with a thin water film and a high flow rate of air (high pressure drop). Under these circumstances, the water flow has a shear driven profile, like that of a Couette profile between the bottom wall and the air-water interface. Friction with the side walls restricts the flow near the walls in the narrow direction, but shear forces dominate the profile at the centerline. This results in a nearly linear velocity profile at the centerline, with a curved profile between the sidewalls. For thicker films, on the other hand, the profile shows characteristics of the pressure-effect on the flow. Figure 3.2(b) shows a high water flow rate, high pressure drop case where both pressure and shear forces influence the water profile shape. The profile largely resembles that of a pressure-driven free interface flow with some additional shearing at the surface. The side walls also restrict the flow to a parabolic profile in the channel depth dimension, but the centerline profile is markedly different than the previous figure. The centerline has a curved profile indicative of a pressure-driven profile transitioning to a layer where the liquid film is affected by shear forces from the air. Because the flow is always constrained by the wall forces, the thickness of this affected layer is on the order of the smallest channel dimension. Figure 3.2(c) shows a case for low pressure drop and high water injection rates. Under these conditions, pressure forces are dominant and the bulk of the water layer exhibits the shape of a purely pressure driven profile in a channel where the smallest dimension

constraints the flow. Again, shear forces affect a small layer of fluid near the interface, pulling this fluid in a thin layer at higher velocities.

### 3.1.1 *Non-dimensionalization and aspect ratio effects*

The key insight arises when this solution is non-dimensionalized according to the ratio of viscosities, the fraction film thickness, and channel aspect ratio, or  $\hat{\mu} = \mu_2/\mu_1$ ,  $\hat{h} = c/(b+c)$ , and  $AR = (b+c)/a$ , respectively. A common factor is extracted from each term, and the function of the velocity profile breaks into two distinct parts, as expressed in (10). The shape is a function of only non-dimensional parameters, namely the viscosity ratio, film thickness, and channel aspect ratio. The magnitudes of velocities are scaled by the pressure gradient, the width of the channel, and one of the viscosities. (The extraction of  $\mu_2$  for the non-dimensionalization of  $\hat{w}^*$  is arbitrary. A choice of  $\mu_1$  for non-dimensionalization would result in a corresponding formulation of  $\hat{w}^*$ ).

$$w_i = \underbrace{\frac{4a^2}{\mu_2} \left( \frac{\Delta P}{\Delta L} \right)}_{\substack{\text{Magnitude} \\ \text{Scaling} \\ \text{Factor}}} \underbrace{\sum_{n=1}^{\infty} \hat{w}_i^* \sin \frac{ZX}{a}}_{\substack{\text{Profile} \\ \text{Shape} \\ f_i(\hat{\mu}, \hat{h}, AR)}} \quad (10)$$

Volume flow rates are calculated by integrating the velocity profile of each phase. The scaling factor drops out of a ratio of volumetric flow rates, leaving a function of only the non-dimensional parameters,  $\mu$ ,  $h$ , and  $AR$ . This means that for a given geometry and set working fluids, the film thickness fraction fixes the volumetric flow

rate ratio for the two fluids, and vice versa. This eliminates many of the variables in the relationship and simplifies an analysis of this system.

$$Q_i = \iint v_i d\hat{x}d\hat{y} \quad (11)$$

$$\frac{Q_a}{Q_w} = \hat{q} = \frac{\frac{4a^2}{\mu_2} \left( \frac{\Delta P}{\Delta L} \right) \iint \sum \bar{v}_a^* \sin p\pi\hat{x} \cdot d\hat{x}d\hat{y}}{\frac{4a^2}{\mu_2} \left( \frac{\Delta P}{\Delta L} \right) \iint \sum \bar{v}_w^* \sin p\pi\hat{x} \cdot d\hat{x}d\hat{y}} \quad (12)$$

$$\hat{q} = f(\hat{\mu}, \hat{h}, AR) \quad (13)$$

For example, an interesting result of this analysis is insight into the effect of channel aspect ratio on the fractional film thickness (which corresponds to a GDL coverage ratio in a fuel cell). The direct relationship between the ratio of volume flow rates and the fractional film thickness for a given ratio of air to water flow rates means that there is a very simple relationship between the liquid coverage ratio and the channel aspect ratio for a given set of operating conditions. The geometry of the problem is shown in Figure 3.3.

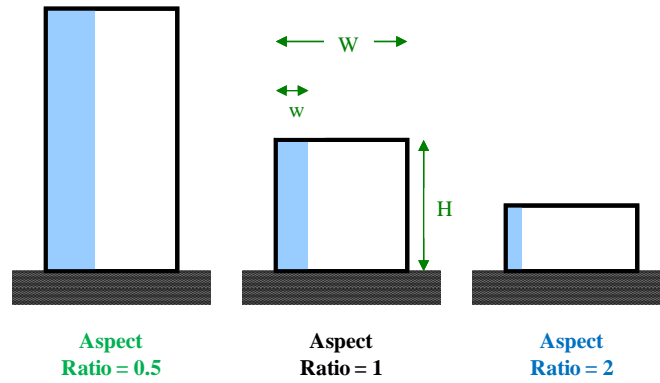


**Figure 3.3: Geometry for aspect ratio and GDL coverage area analysis.**

The fractional film thickness is calculated for the same air-water flow rate ratio (which corresponds to equivalent operating stoichiometry) in channels of various aspect ratios according to (12). The results are shown in Figure 3.4. The coverage of the liquid film decreases with increasing stoichiometric ratio, as expected. Interestingly, the channel coverage ratio also decreases by small margin as the channel aspect ratio increases.

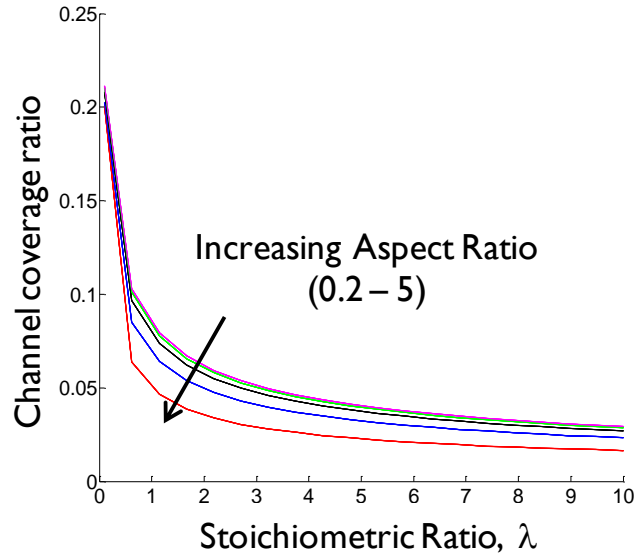


**Figure 3.4: Decrease of channel coverage ratio with increasing channel aspect ratio.**

There is, of course, a trade-off for this design problem. If we fix the channel width to a constant value, as this represents the GDL contact area in the fuel cell, the increase in channel aspect ratio corresponds to a decrease in channel height. We fix the actual flow rates to correspond to a certain current density and stoichiometric ratio and we suffer a severe increase in pressure gradient required to move the fluids through the channel according to the magnitude scaling factor as given by (10). In fact, a decrease of 40% in the channel coverage ratio requires an increase in supply pressure of a factor of 30!

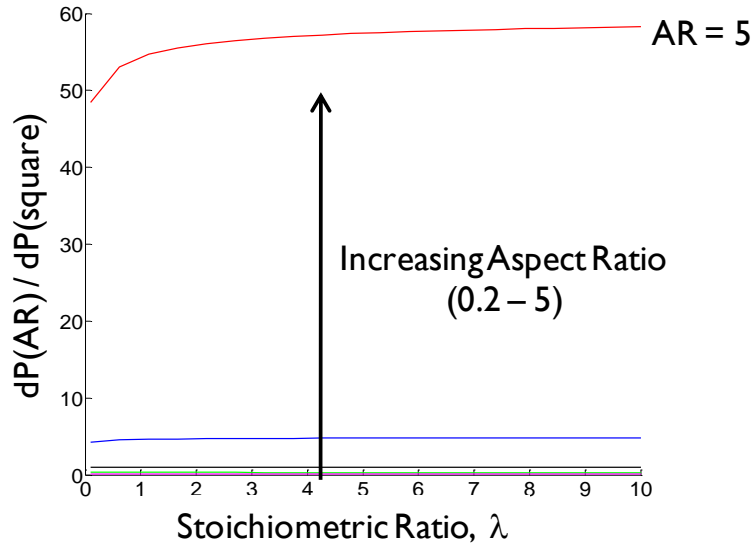


**Figure 3.5:** Increase in pressure requirement for increasing channel aspect ratio over a range of stoichiometric ratios.

### 3.1.2 Assessment of a simplified model

The analytical solution can be used to predict the limits of validity of other simplified models of stratified two-phase flow. Lee [72] has proposed a variation of the Taitel assumption which states that the pressure gradient of stratified flow in a rectangular channel can be calculated according to single phase flow of the gas phase in a channel of reduced dimension, treating the liquid phase as a solid wall. He presents data from a  $500\ \mu\text{m} \times 45\ \mu\text{m}$  channel which is well-described by this model. In order to determine the limits of validity of this simplified model for channels of various aspect ratios, we compare predicted pressure gradients and air flow rates in a channel of reduced area to that of two phase flow using the analytical solution. The

multiplicative terms drop out from the ratio of the solutions, so there is a direct proportionality between the flow rate and the pressure gradient.

We define a ‘Deviation Factor’ which represents the ratio of the air flow rate in a single phase air channel of reduced dimension to the air flow rate in the air region of the stratified flow equation in the 2D two-phase analytical solution. This is equivalent to an inverse ratio of the pressure gradients in the channels. The deviation factor is defined as

$$\frac{\hat{Q}_{SP}}{\hat{Q}_{TP}} = \frac{\left(-\frac{\Delta P}{\Delta L}\right)_{TP}}{\left(-\frac{\Delta P}{\Delta L}\right)_{SP}} = \frac{\iint \sum_{SP} d\hat{x}d\hat{y}}{\iint \sum_{TP} d\hat{x}d\hat{y}} \quad (14)$$

where the integration represents the integration of the velocity profile over the region indicated and the summation represents the summation of Fourier series terms for the solution of the single phase (SP) or two phase (TP) analysis.

When the deviation factor is equal to 1, the gas-phase area model and the analytical solution are identical. When the deviation factor is less than 1, for a given volume flow rate of air, the model over predicts the pressure drop in channel, because the moving interface lubricates fluid flow and reduces shear on the gas at this interface. Alternatively, a deviation factor less than 1 means that the model under predicts the volume flow rate of air for a given pressure drop.

The results of this analysis are shown in Figure 3.6 for a range of channel aspect ratios and fractional film thicknesses. When the fraction film thickness is less than half the channel width, the gas phase area model is accurate within 10% for all channel aspect ratios. When the film thickness increases beyond this point, however, significant deviations become apparent especially in low aspect ratio channels which approach the limiting case of flow between two infinite plates. However, it is probably not reasonable to assume that the geometry of the flow is well approximated by a simple flat-interfaced stratified flow geometry under these conditions and this analysis breaks down for other flow structures. For the high aspect ratio channels, the gas-phase area assumption approximates the flow very well to fractional film thickness as great as 0.7 to 0.8.

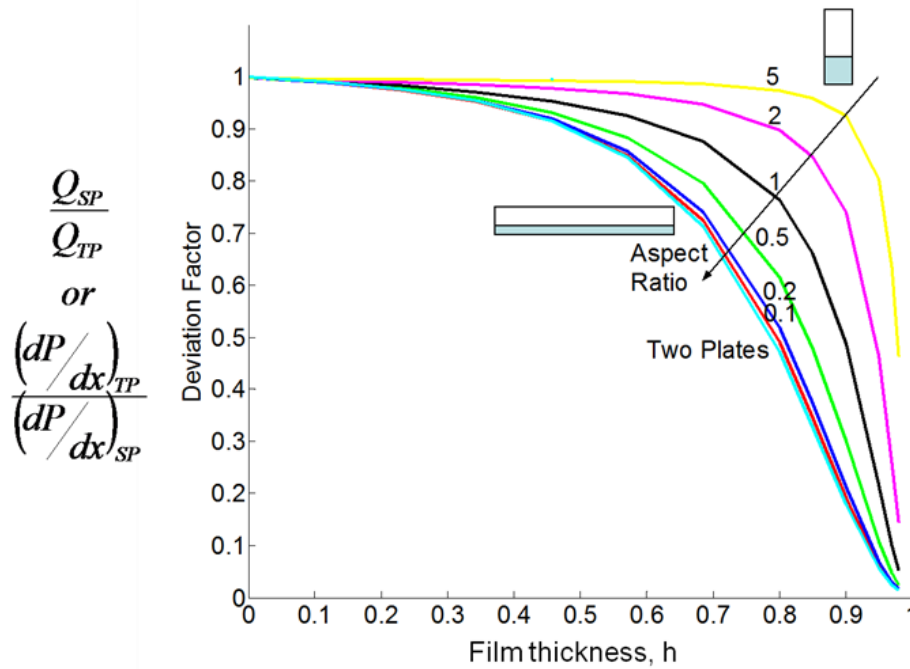


**Figure 3.6: Deviation factor of gas-phase area model of stratified flow compared with a 2D analytical solution.**



## 3.2 Stratified flow experiments

A fluorescence technique is developed to measure the liquid film thickness variation of stratified flows. The water, seeded with Fluorescein dye, is imaged through a microscope onto a CCD camera. Liquid film thickness is determined by counting pixels with intensities above a threshold which was determined by examining the intensity profile. Uncertainties due to setting the threshold intensity are considered. Film thickness data is shown as a function of air and water flow rates and compared with the predictions of a separated two-phase flow model. Significant trends in the data which characterize the flow regime are discussed.

These data are critical for improving models for two-phase transport in PEM gas delivery microchannels. The technique developed here provides important information about the interactions between the gas and liquid phases in the microchannels, a major driving force behind heat and mass transport management within the fuel cell.

## 3.3 Experimental Method

### 3.3.1 *Measurement procedure*

Fluorescent images are captured at multiple water flow rates for fixed inlet air pressures and varying exit pressures. In the U-shaped channels, the inlet pressure was set at 15 psig and at 30 psig. The pressure drop was controlled with the outlet needle valve configuration. For an inlet pressure of 15 psig, average inlet air velocities

ranging from less than 1 m/s to greater than 25 m/s were achieved. For an inlet pressure of 30 psig, maximum air velocities approach 60 m/s. Dry, filtered air is used for the experiments. At each exit pressure, images of the flow are captured once the system achieves a steady condition. Between settings, the channel is evacuated of water by opening the exit valve to the atmosphere and allowing dry air to clear the water film. This prevents any surface tension induced hysteresis from the previous flow configuration.

Under some stable flow conditions, fluorescent images are taken at a single location approximately halfway between the water injection slot and the downstream bend of the channel. At low air velocities, when large fluctuations in the film thickness along the length of the channel were observed, multiple locations along the length of the channel are imaged. Under high air flow rates, a downstream instability develops in the film, causing the appearance of wisps of liquid departing from the film into the air stream. In these cases, the film thickness is measured closer to the water injection point where a stable film adheres to the wall.

Absolute and differential pressure and mass flow rate measurements are also recorded at each flow condition. Pressure measurements were collected and averaged in sets of 100 readings. Mass flow rates were measured at 12.5 Hz and averaged over at least 30 seconds.

### 3.3.2 Data analysis

Average inlet air velocity values are calculated from the measured mass flow rates. The mass flow rate is divided by the temperature and pressure dependent air density and the cross-sectional area of the gas channel.

Film thickness measurements are extracted from fluorescent images of the flow using a threshold-intensity pixel-counting technique. After subtracting the average background intensity from each image, the profile of the intensity was examined at a typical flow cross-section. From this profile, two threshold values of intensity were determined, representing a low and a high intensity reading which might reasonably represent the edge of the film. Typical background intensity was 100; typical film intensity was 900. The threshold values were set as 30% and 70% of the peak intensity increase over the background.

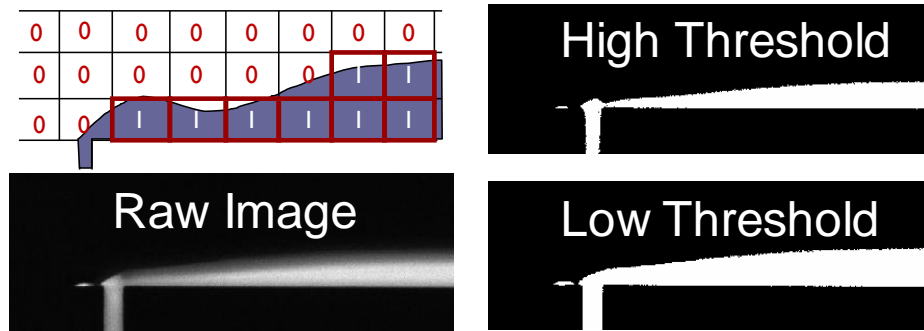


**Figure 3.7: Process of image thresholding with an example image of stratified flow at the water injection location. Two threshold intensity values are used to bracket the uncertainty in the film thickness. The schematic depiction of the technique exaggerates the pixel size.**

For each threshold value, images are processed such that each pixel with intensity greater than the threshold is assigned a binary value of 1, otherwise the pixel is assigned a value of 0. Figure 3.7 illustrates the transformation of a raw image into high and low threshold binary images. In this manner, the film thickness at each cross-section of the channel is easily calculated by summing a column of pixels. The schematic exaggerates the pixel size relative to the film thickness; in these studies, images were collected with cross channel resolutions of 100 to 775 pixels, depending on the camera and magnification of the objective. The particular resolution is noted with the results for each channel configuration. The recorded film thickness averaged over the cross section along the length of the channels.

### **3.3.3 *Uncertainty***

#### ***Velocity***

The uncertainty in the velocity measurement is derived from the quoted accuracy of the mass flow meters and channel geometries. Two mass flow meter readings were compared: a thermal mass flow meter with a quoted accuracy of  $\pm 3\%$  measured value, and a laminar pressure drop flow meter with an accuracy of  $\pm 0.015$  SLPM. Velocities calculated from the thermal mass flow meter readings are reported with an accuracy of  $\pm 5\%$  MV, including uncertainties in the channel depth and air density. There is a constant velocity offset of 1.2 m/s between the two flow meter readings.

#### ***Film Thickness***

There are several sources of uncertainty in this optical measurement technique. Less significant sources include the two-dimensional nature of the measurement which

yields depth-averaged fluorescence intensities that are a function of the depth of field of the microscope objective as well as limitations of resolution due to finite pixel dimensions. In some cases, optical effects cause unphysical variations in fluorescent intensity near the edge of the film likely due to internal reflection by incident, scattered, and emitted light. These fluctuations may be an obstacle when extracting quantitative information from fluorescent intensity, but they do not significantly affect this thresholding technique.

Uncertainty due to threshold value setting for the film becomes significant at high air flow rate, low water flow rate cases as shown in Fig. 4. Under these conditions there is a grey region of nearly 10  $\mu\text{m}$  between the film thickness measured by high and low threshold values. This interesting phenomenon may be due to the presence of a meniscus or 3-dimensional shape of the fluid film, which causes regions of lower fluorescent intensity at the top and bottom of the channel and blurs the appearance of the interface in the two-dimensional imaging technique, which is focused near the vertical center of the channel. Other means of capturing this flow phenomenon and reducing this uncertainty are being investigated. The results presented in this paper use the average of the thicknesses calculated from the two threshold values. The error bars for this uncertainty are shown at high air velocities.

Error bars on low air velocity, large film thicknesses represent the conditions of high water flow rate and low air flow rates creating stationery waves in the film along the length of the channel. The magnitude of these waves varies with flow conditions. A transition occurs for high air flow rates and stationery waves are not observed for these thinner films.

## 3.4 Results and discussion

### 3.4.1 Images

Figures 3.8 and 3.9 show sample images from two of the channels where stratified conditions are observed. Figure 3.8 shows stratified flow in  $500\text{ }\mu\text{m} \times 45\text{ }\mu\text{m}$  channels. The imaging location is between the water injection location and the curve of the U-shaped channel. The variation in the structure of the flow is evident from these images, where the two images in the top row exhibit large fluctuation in the film thickness. These images are taken in conditions where the gas flow rate is low. The gas-phase Weber number of the top images are  $3 \cdot 10^{-4}$  and 0.05, while the Reynolds numbers are 3 and 35, respectively. The low Weber numbers indicated that surface tension is a dominant force, which is evident in the behavior of these interface. The interfacial structures are stationary and stable over minutes of constant flow conditions. When the water flow is stopped and restarted, the exact location of the interface changes, but the presence of stationary waves is consistent when the flow is restarted. The particular configuration of the initial impingement of liquid into the dry channel appears to establish a specific interface profile. Once this interface has been established, it seems pinned to that configuration as long as water remains in the channel. When the air flow rate is increased beyond a certain value, the interface can be moved and reconfigured, however the film is remarkably stable except to large increases in gas flow, indicating that the contact line pinning is important.

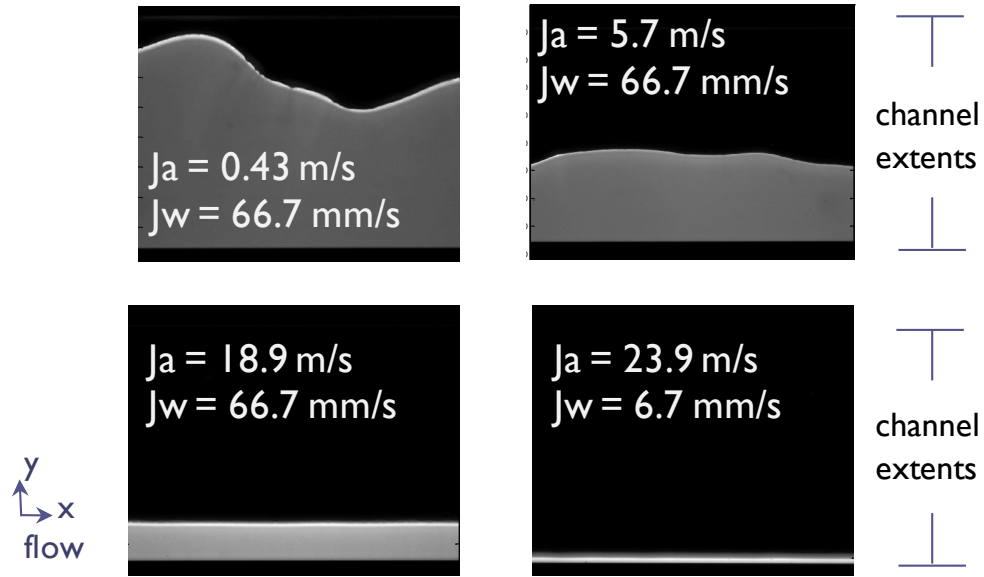


**Figure 3.8: Example images of stratified flow from 500  $\mu\text{m}$  x 45  $\mu\text{m}$  channels. The channel extents marking shows the 500  $\mu\text{m}$  scale of the images, which corresponds to 775 pixels. The top two images show flows with large stationary waves. The bottom two images show films with smooth stationary interfaces.**

The bottom images in Figure 3.8 show flow in the channel with a smooth air water interface. These images are taken under higher air flow conditions than the top images, with gas-phase Weber numbers of 0.5 and 0.9, and Reynolds numbers of 115 and 145, respectively. As the gas-phase Weber number increases, the inertial force of the air becomes more significant compared with the surface tension forces of the air-water interface and the interface becomes smooth.

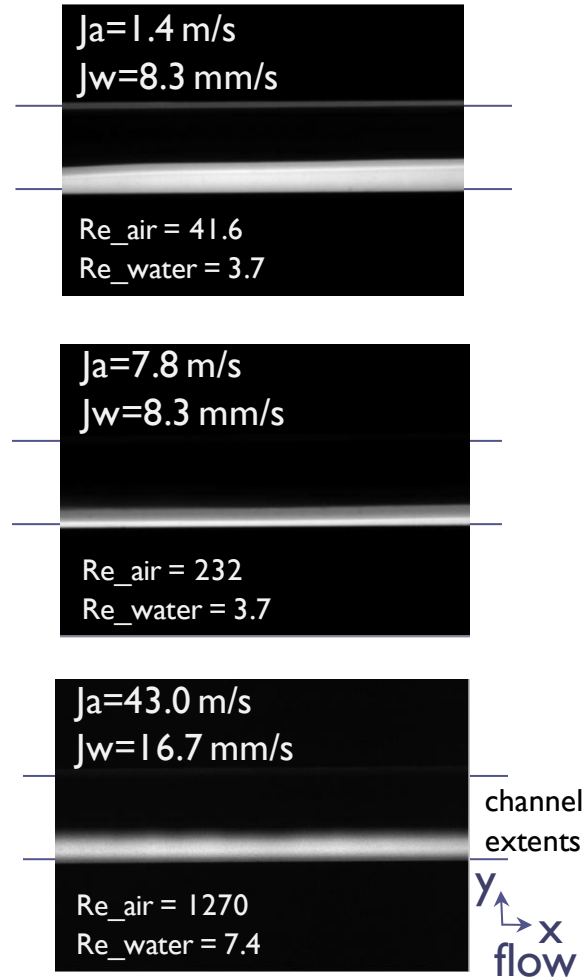


**Figure 3.9:** Sample images of stratified flow in  $500\ \mu\text{m} \times 400\ \mu\text{m}$  channels. The channel extents marked on the image correspond to the  $500\ \mu\text{m}$  dimension, which has a resolution of 310 pixels across the channel width.

Figure 3.9 shows sample images from the  $500\ \mu\text{m} \times 400\ \mu\text{m}$  channels. In these three images, the interface is flatter but the appearance of the interface varies. The focus adjustment of the microscope was tested to be sure that this blurriness of the interface in the bottom image, for example, was not due to improper focusing of the



microscope. Instead, the variation in appearance of the interface may represent a difference in the actual structure of the interface. The bottom image represents the highest air flow rate tested, corresponding to a Reynolds number of 1270 for the gas phase, so this is not expected to be an effect of turbulence of the air phase. More detailed imaging of this interface would be helpful to understand this effect. The Weber numbers of the flow in the  $500\text{ }\mu\text{m} \times 400\text{ }\mu\text{m}$  channels range from 0.01 to 20, with transition to the blurry interface like that of the bottom image in Figure 19 occurring for Weber numbers greater than 2. The liquid phase Reynolds numbers of the blurry interface conditions based on the superficial velocity and hydraulic diameter of the channel are less than 10.

### ***3.4.2 Film thickness measurements***

The horizontal extent of the liquid film is measured according to the threshold-intensity pixel counting technique described in Section 3.3.2. Under all experimental conditions tested, the trend is consistent that the measured film thickness decreases with increasing air velocity, or correspondingly, increasing pressure drop along the channel. The variation of film thickness in a  $500\text{ }\mu\text{m}$  by  $45\text{ }\mu\text{m}$  channel with a constant superficial water velocity of  $67\text{ mm/s}$  and inlet air velocities up to  $25\text{ m/s}$  is shown in Figure 3.10. Two types of uncertainty bars are reported on this figure. Those below an inlet air velocity of  $11\text{ m/s}$  correspond to the actual peak-to-peak variation in the film thickness measured from images taken along the channel. Those for higher air velocities indicate the range of uncertainty associated with setting the threshold intensity value for the film.

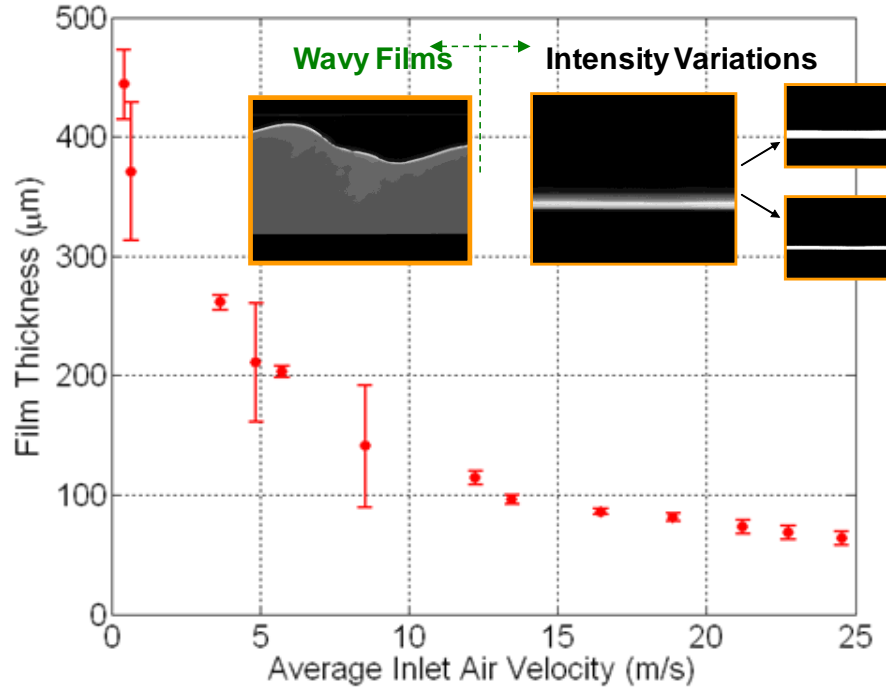


**Figure 3.10: Variation of film thickness with inlet air superficial velocity in  $500\ \mu\text{m} \times 45\ \mu\text{m}$  channel. Water superficial velocity is  $67\ \text{mm/s}$ .**

Drawing insight from the analysis of Section 3.1, we note that wavy films correspond to the velocity profiles for thick films, those which take on the profile of a pressure driven flow with a thin layer of liquid pulled by shear forces at the interface. Films with smooth interfaces exhibit velocity profiles dominated by the interface shear.

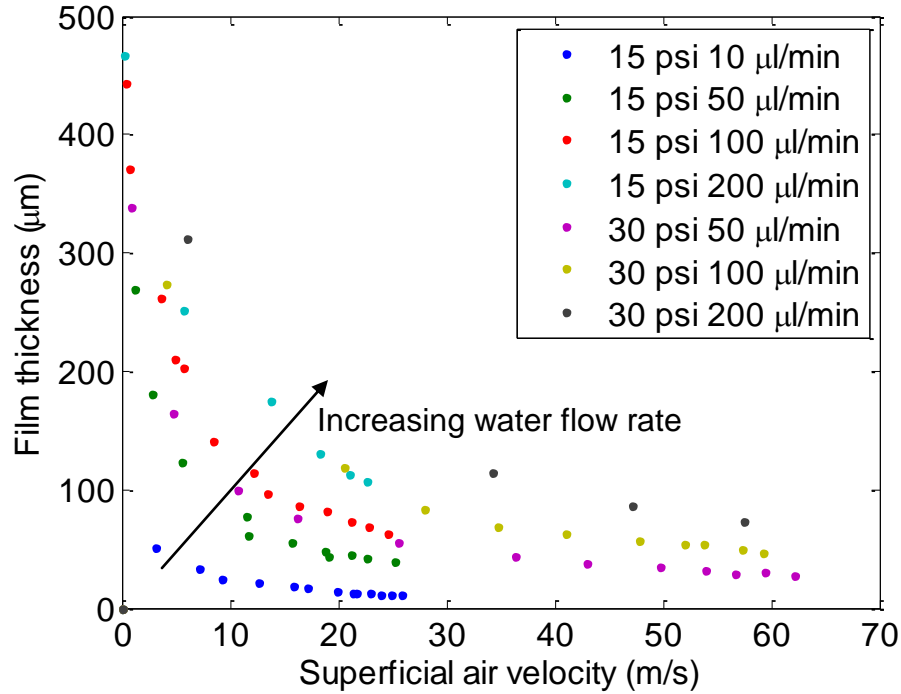


**Figure 3.11: Variation of film thickness with superficial air velocity in 500  $\mu\text{m}$  x 45  $\mu\text{m}$  channels for a variety of water injection rates (superficial water velocities range from 7 to 130 mm/s) and two inlet air pressures. The film thickness is captured with a resolution of 775 pixels across the channel width, or 0.645  $\mu\text{m}$ .**

Figure 3.11 shows the variation of film thickness with increasing air velocity for a variety of water flow rates. For a given water injection rate, the liquid film thickness decreases non-linearly as air velocity increases. When the film is thick, it is very sensitive to the air velocity. Slight increases in air velocity result in substantial decrease of the film thickness. At high air flow rates, the water film thickness asymptotes toward a minimum film thickness. Further increases in air flow rate no longer affect a substantial increase in the water velocity, seen as a decrease in liquid film thickness. Higher water injection rates increase the film thickness for a given air

flow rate. This effect is most prominent when water injection rates are low and changes in injection rate produce larger increases in film thickness.

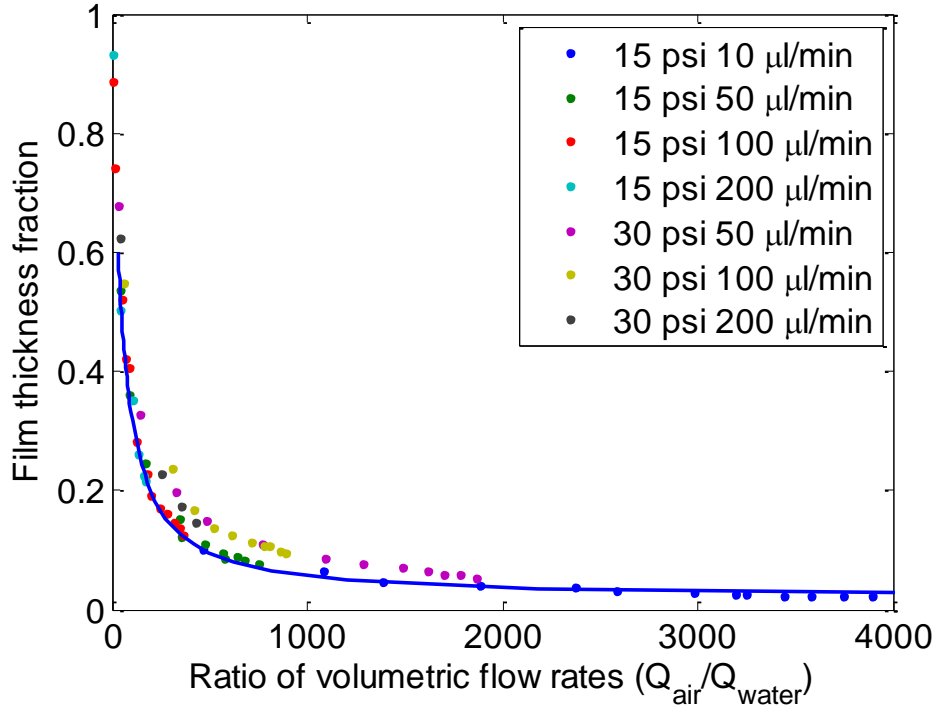


**Figure 3.12: Presentation of film thickness variation results from 500  $\mu\text{m}$  x 45  $\mu\text{m}$  channels according to non-dimensional parameters, film thickness fraction and ratio of volumetric flow rates.**

The film thickness measurements are non-dimensionalized and compared with the analytical solution presented in Section 3.1. The film thickness is non-dimensionalized by the channel width; the superficial velocities are non-dimensionalized as a ratio of volumetric flow rates. This non-dimensionalization collapses the data from the various water injection rates onto nearly the same curve, as shown in Figure 3.12. These data match the prediction of the analytical solution well, providing support of

the assumptions of the analytical solution to describe stratified air-water flow in these high-aspect ratio channels.

The non-dimensional film thickness data are shown in Figure 3.13 and Figure 3.14 for stratified flow in the more square channels, the  $430\text{ }\mu\text{m} \times 240\text{ }\mu\text{m}$  channel and the  $500\text{ }\mu\text{m} \times 400\text{ }\mu\text{m}$  channel. These data are plotted on log-linear axes for clarity. Here, the two types of uncertainty that have been discussed previously are plotted for each data point. The lighter lines represent the actual thickness variation measured in the images recorded along the length of the channel. The dark blue lines correspond to the variations in setting the threshold intensity for the thickness.

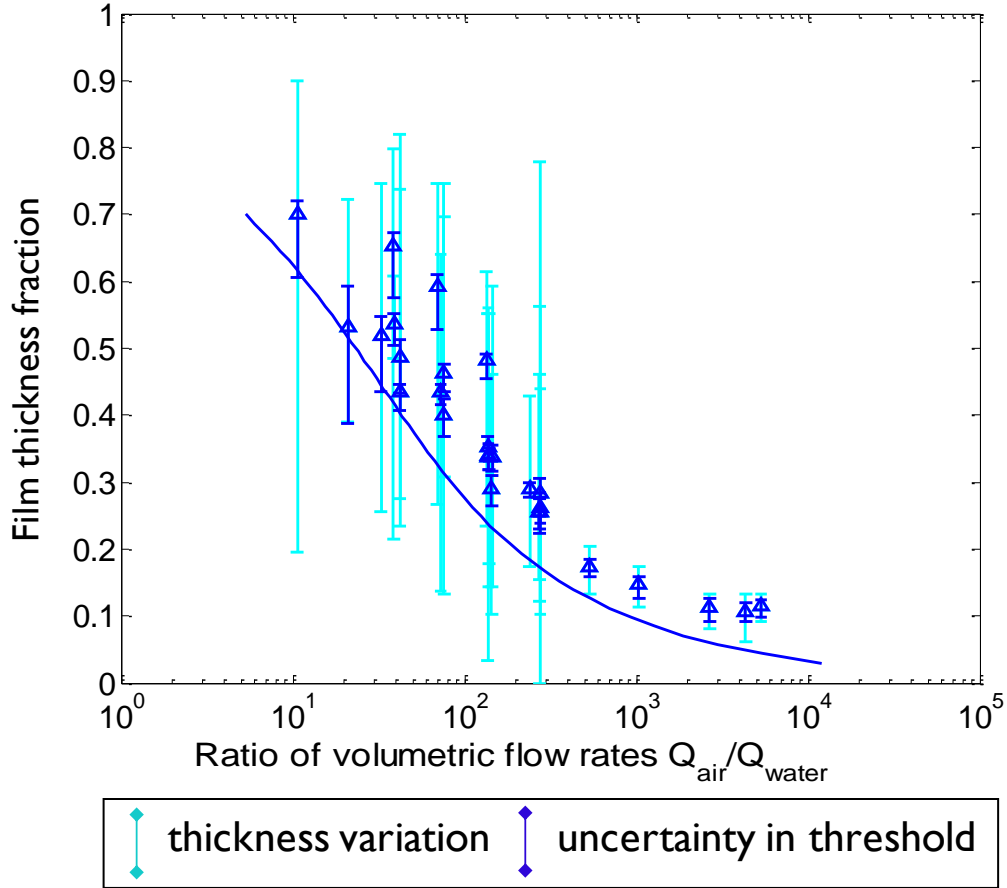


**Figure 3.13: Variation in film thickness with volumetric flow rate ratio in a 430  $\mu\text{m}$  x 240  $\mu\text{m}$  channel compared with the analytical solution shown as a solid line. The channel is imaged with a resolution of 100 pixels across the 430  $\mu\text{m}$  channel width using the Phantom high speed camera.**

The data for the 430  $\mu\text{m}$  x 240  $\mu\text{m}$  channel are shown in Figure 3.13. The Reynolds numbers of these flows range from 0.6 to 330, the liquid Reynolds number ranges from 1 to 2, based on superficial velocities and full channel hydraulic diameter. In these channels, large variations in the film thickness exist up to a flow rate ratio of 300, which corresponds to a gas-phase Weber number of 0.02 for the particular flow rates of this experiment. At air flow rates above this threshold, the films smooth and

the variation in the actual film thickness is comparable to the uncertainty due to the intensity threshold. The data nearly collapse to a single curve, though there is more scatter among the data at lower flow rate ratios which corresponds to the conditions where the film thickness changes most rapidly with changes in air flow rate.

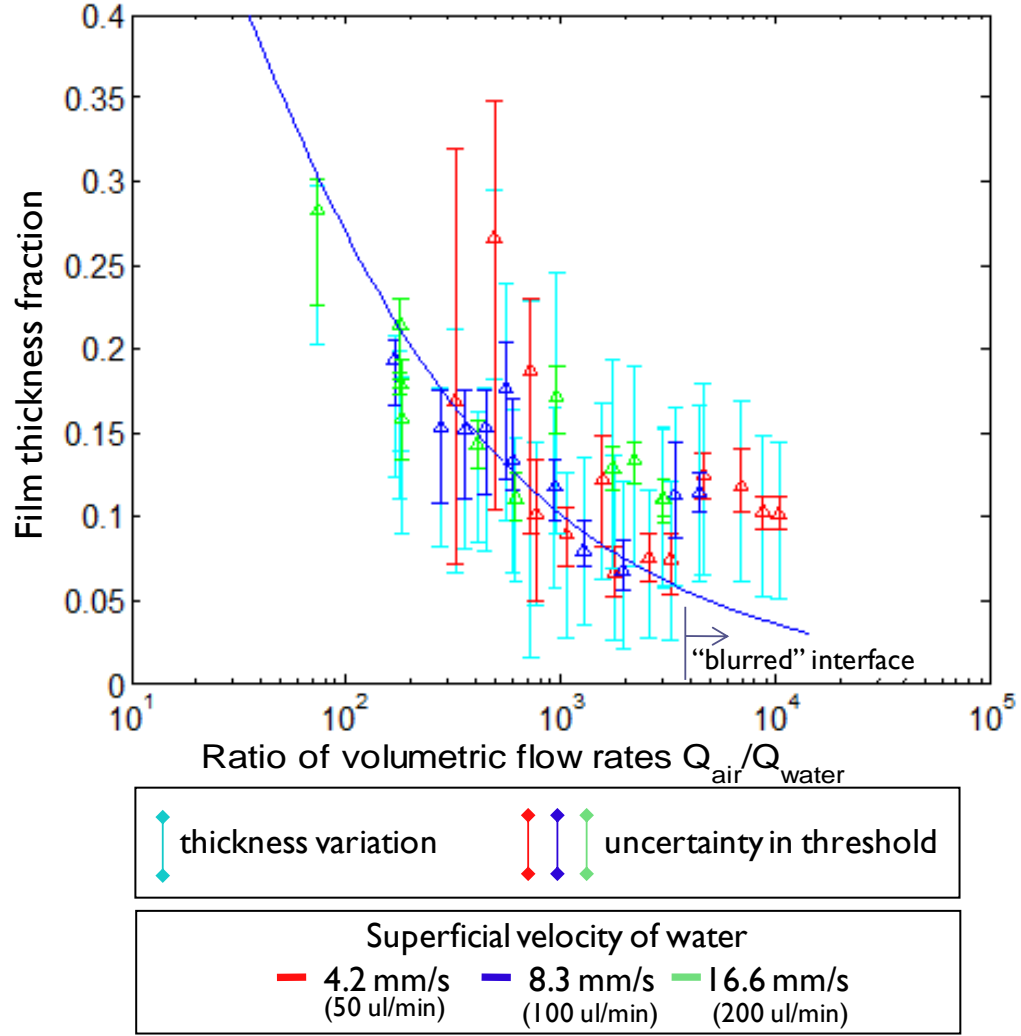
The data follow the trend predicted by the analytical solution as shown by the solid line on Figure 3.13, yet the solution slightly under predicts the measured film thicknesses. This effect is likely due to curvature of the interface which increases the apparent film thickness due to the presence of a meniscus of water on the glass and channel surfaces. The analysis and integration of the velocity profiles assume that the interface between the phases is flat. This imposes both a minimum surface for interaction of the air and water phases, it also maximizes the liquid volume for a given film thickness at the wall (assuming this is the point of largest film thickness). If the effect of the meniscus is not captured in the interface, the measurements will overestimate the actual film thickness when interfacial curvature is considered.

Figure 3.14 shows the data for the largest channels in this study, which are nearly square, measuring 500  $\mu\text{m}$  wide x 400  $\mu\text{m}$  deep. Stratified flow appears in these channels under all conditions tested. Note that the scale on this figure is expanded in the vertical direction compared with the previous channels. Because a flow rate ratio lower than 60 was not achieved in these channels, the films never grow thicker than 30% of the channel width. The large variations in film thickness that characterized the flow for low flow rate ratios in high aspect ratio channels were not observed in these channels under the tested conditions. This may be due to a lack of data at lower flow rate ratios. One noted change in the structure of the liquid film was a blurring of the

film at flow rate ratios greater than 4000. At this point, the film appearance changes from similar to that of the middle image in Figure 3.9 to similar to the bottom image in the same figure. At this point, the measured film thickness increases, an artifact of the extent of the blurred image of the film. This blurring did not improve with an adjustment of the microscope focus; rather it seems to be an indication of some change in the structure or imageability of the film due to interference of the channel walls, for example.

With the exception of the points taken from measurements of the blurred interfaces, the data in the  $500\text{ }\mu\text{m} \times 400\text{ }\mu\text{m}$  channels follows the general trend of the analytical solution, with more scatter in the data than seen in the  $500\text{ }\mu\text{m} \times 45\text{ }\mu\text{m}$  case. The data appears slightly bifurcated, with some data following the analytical solution closely, but another set of data points from each water injection condition having larger film thicknesses than predicted by the analytical solution. Following the argument presented for the  $430\text{ }\mu\text{m} \times 240\text{ }\mu\text{m}$  case, this could be an artifact of the curvature of the interface, which may lead to a overestimate of the film thickness compared to a model based on a flat interface. This brings into question the validity of the assumption of the flat interface model for the analysis of two-phase flow in nearly square microchannels. Nevertheless, the trend is similar and the results match reasonably well for the conditions tested, confirming that the analytical solution presented is a reasonable approximation of these flows.





**Figure 3.14: Variation of film thickness fraction with volumetric flow rate ratio in 500  $\mu\text{m}$  x 400  $\mu\text{m}$  U-shaped channel compared with analytical solution to stratified flow with flat interface. The full channel width corresponds to 310 pixels.**

### 3.5 Conclusions

This section presented data and analysis of stratified flow in rectangular microchannels, offering insight into the physics of this previously unreported flow regime. We have measured liquid film extent in stratified two-phase microchannel

flows for the purpose of characterizing flow regime parameters and transitions. Film thickness data vary strongly with air velocity and are consistent with a stratified flow model which was also presented. This information was used to verify model predictions of the two-phase flow and validate the limits of applicability of this simplified model.

## **Chapter 4. Two-phase flow visualization in an ex-situ PEM fuel cell channel**

In order to examine two-phase flow in a microchannel more closely replicating the geometry and materials of a fuel cell, an ex-situ setup was constructed for the visualization of the evolution of flow regimes along a long, serpentine microchannel with distributed water injection through a carbon paper wall [83 84]. The present work bridges the gap between in-situ experiments on operating fuel cells and two-phase flow experiments in different geometries. Liquid water is introduced into the channel through the porous carbon paper gas diffusion layer which flanks one channel wall, thereby allowing for the characterization of flow regime transitions with known flow rates. Unlike visualization of operating fuel cells, this setup allows for precise control of both liquid and gas flow rates and injection conditions. Compared with other ex-situ experiments, this study incorporates channels with smaller cross-sectional dimensions than many previous fuel cell related studies. Compared with fundamental two-phase flow studies in microchannels, this study better replicates the characteristics of fuel cell channels, including longer channel lengths and distributed water introduction. The channel dimensions of 500  $\mu\text{m}$  x 500  $\mu\text{m}$  square channels

were chosen as a trade-off between the projected performance improvements of microchannels and expected issues with flooding and clogging in small channels. Understanding the flow regimes in these channels, which are smaller in dimension and cross-sectional area than standard fuel cell channels, provides insight into the possible use of microchannels for fuel cell applications. The smaller separation between channel walls means that a larger percentage of the droplets entering the channel will come in contact with a channel wall, potentially leading to more favorable flow regimes at the expense of larger viscous losses. This study provides insight to key two-phase flow structure transitions of importance for performance-critical water management in PEM fuel cell channels.

## **4.1 Experimental method**

### ***4.1.1 Sample geometry and preparation***

A single serpentine channel replicates flow conditions associated with fuel cell gas delivery channels as shown in Figure 4.1. A channel with a 500  $\mu\text{m}$  x 500  $\mu\text{m}$  square cross-section is machined in acrylic. The channel follows a 60-cm long serpentine layout incorporating five long segments and four short turns. The fourth wall of the channel is comprised of a 2 mm wide, 190  $\mu\text{m}$  thick ribbon of porous carbon paper GDL which follows the channel geometry and fits into a latex gasket which is carefully patterned using a CO<sub>2</sub> laser ablator. The GDL paper is pressed against the channel structure with an acrylic slab using 44 evenly spaced bolts for even distribution of pressure. Water is injected into the channel at eight locations using a

multi-syringe pump (Harvard Instruments) via 500  $\mu\text{m}$  diameter holes through the bottom acrylic slab on the backside of the carbon paper wall, causing water flow through the GDL into the channel.

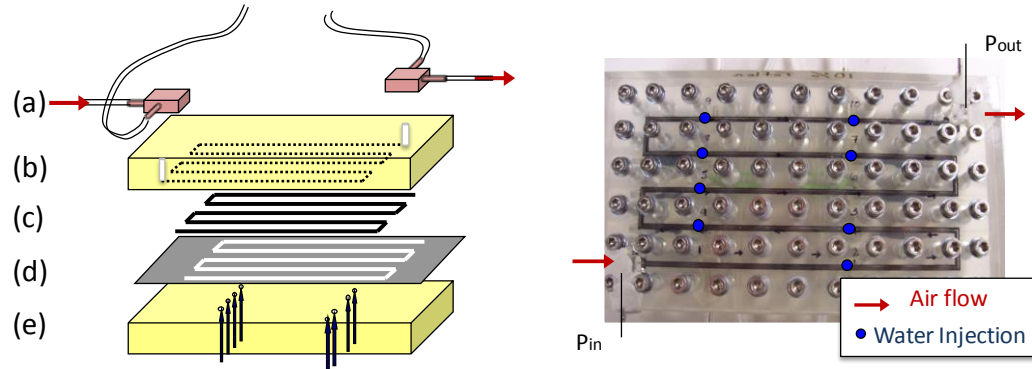


**Figure 4.1: Channel assembly.** The following layers are sandwiched together to create a sealed serpentine channel with distributed water injection through the porous GDL layer: (a) connections to air tubing and pressure transducers, (b)  $\frac{1}{4}$ " cast acrylic with 500  $\mu\text{m}$  x 500  $\mu\text{m}$  x 60 cm channel, (c) 190  $\mu\text{m}$  thick x 2 mm wide Toray Carbon Paper GDL (0, 10 wt% Teflon), (d) Latex gasket, (e)  $\frac{1}{4}$ " cast acrylic with 300 – 500  $\mu\text{m}$  diameter water injection holes.

Various injection configurations were considered before discrete liquid injection was chosen. While an ex-situ setup does not perfectly replicate the molecule-by-molecule production of water of operating fuel cells, the visualization of operating fuel cells show the water entering the channel in the form of droplets [e.g. 64]. The approximation of water introduction from discrete points still provides some insight into the overall flow behavior once the water has entered the channel. Other injection geometries incorporating reservoirs or channels behind the GDL layer suffered from the preferential flow of air through the GDL pores and small channels. In these

geometries, liquid water cannot be made to completely fill injection reservoirs when a pressure gradient is applied across the device; air is unavoidably entrained into these cavities and flows through the channels and the injection reservoirs in parallel. Consequently, liquid injection was very unevenly distributed and local conditions were difficult to characterize. Compared with reservoir or channel injection, the discrete injection scheme provides control of the local water flow rate and facilitates observation of changes in the flow structure as more water is introduced as the two-phase flow progresses downstream. The channels were carefully polished with plastic polishing compound (Novus). In order to examine the influence of corners on the flow regime transitions, samples with 11 cm long straight channels are also constructed. These channels are similarly milled in acrylic, with eight water injection locations evenly spaced along the length.

Toray GDL papers (TGPH-090) with and without impregnation with a 10 wt% Teflon solution are used in order to examine the effect of GDL hydrophobicity on the flow observed in the channels. Toray GDL paper is a commercially available material commonly used in fuel cell manufacture. The specific formula for hydrophobic coatings is proprietary and varies significantly from manufacturer to manufacturer. The use of this teflonated GDL is intended to provide qualitative evidence of the influence of hydrophobicity of the porous material on the flow in the channels.

### **4.1.2 Procedure**

Figure 4.2 shows the experimental setup delivering air and water to the channel structure. Air and water flow rates are chosen according to the operating conditions of

a PEM fuel cell. Upstream air pressure is held constant at a gage pressure of 1 atm. Downstream pressure is regulated with a needle valve at the exit in order to establish the desired flow conditions. Inlet and differential pressures are measured using diaphragm differential pressure sensors (Validyne). Air flow rate is measured with flow meters located in-line upstream of the test section (Sensirion thermal mass flow meter and Omega laminar-passage air flow meter). Liquid injection is metered with a syringe pump (Harvard PHD 2200) fitted with a multiple syringe rack holding eight identical glass syringes (Hamilton Gastight 1 mL). Care was taken to evacuate all syringes, tubing, filters, and connectors of air bubbles to reduce the capacitance of the system. Hard-walled Teflon tubing was used for the same reason.

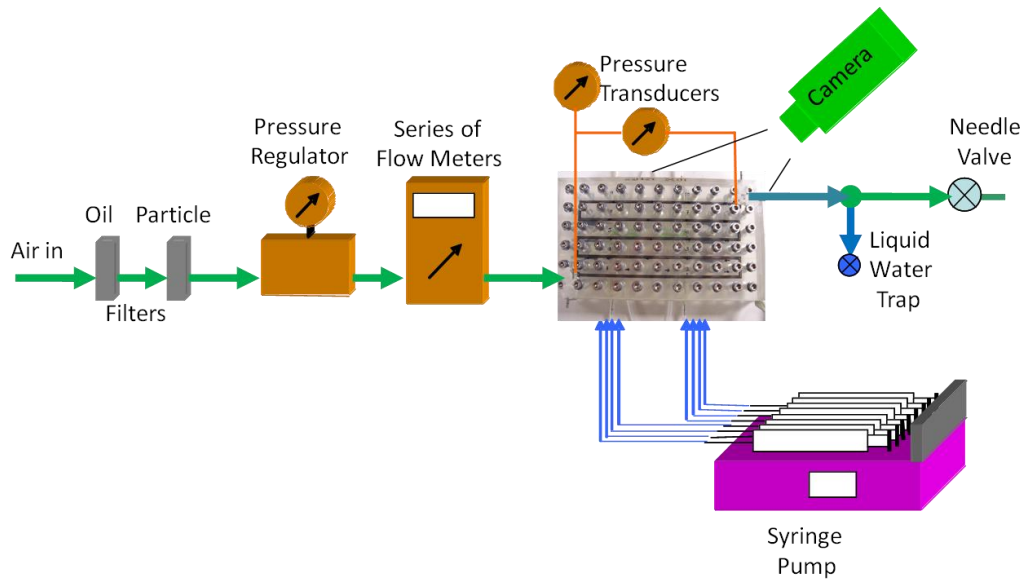


**Figure 4.2: Schematic of experimental setup.**

Experimental parameters correspond to reasonable operating conditions for PEM fuel cells as enumerated in Table 4.1. Water is injected at rates equivalent to current

densities,  $i$ , between 0.5 and 2 A-cm<sup>-2</sup>. The equivalencies are calculated according to equations (15) and (16), assuming an osmotic drag coefficient,  $\alpha$ , of 0.5 molecules of water per proton and an effective land area equal to the channel area. Air flow rates correspond to equivalent stoichiometric ratios,  $\lambda$ , from 1 to 4.

**Table 4.1: Experimental conditions and fuel cell equivalents for serpentine channels**

			<u>Q<sub>a</sub> / Std. L min<sup>-1</sup></u>			
I	Q <sub>w</sub>	Q <sub>w</sub> /inj.	Stoich. Coeff.			
A cm <sup>-2</sup>	μl min <sup>-1</sup>	μl min <sup>-1</sup>	1	2	3	4
0.5	33.6	4.21	0.088	0.176	0.264	0.352
1	67.3	8.41	0.176	0.352	0.528	0.704
2	134.6	16.83	0.352	0.704		

$$Q_{water} = i \cdot \frac{(1 + \alpha)}{2F} \frac{M_{H_2O}}{\rho_{H_2O}} \cdot (2 \cdot W \cdot L) \quad (15)$$

$$Q_{air} = i \cdot \frac{(2 \cdot W \cdot L)}{0.21 \cdot F} \frac{M_{air}}{\rho_{air}} \lambda \quad (16)$$

Between experiments, dry air flows through the channel for at least 30 minutes to provide consistent starting conditions by drying the GDL of accumulated water from the previous test. The air flow rate is established by setting the downstream needle valve. Then liquid water injection begins. Pressure and air flow rates are recorded while images of the channel are captured using a 1392 x 1040 pixel CCD camera



(Nikon Coolsnap ES) once flow conditions appear steady after several minutes. Two hundred images are collected sequentially to create movies of the flow in the channel. The data and image collection is repeated after 10-15 minutes of flow to ensure that flow conditions are not changing. Other researchers have found that the time scale of significant water accumulation in GDL papers is on the order of minutes [85].

### 4.1.3 Flow Visualization

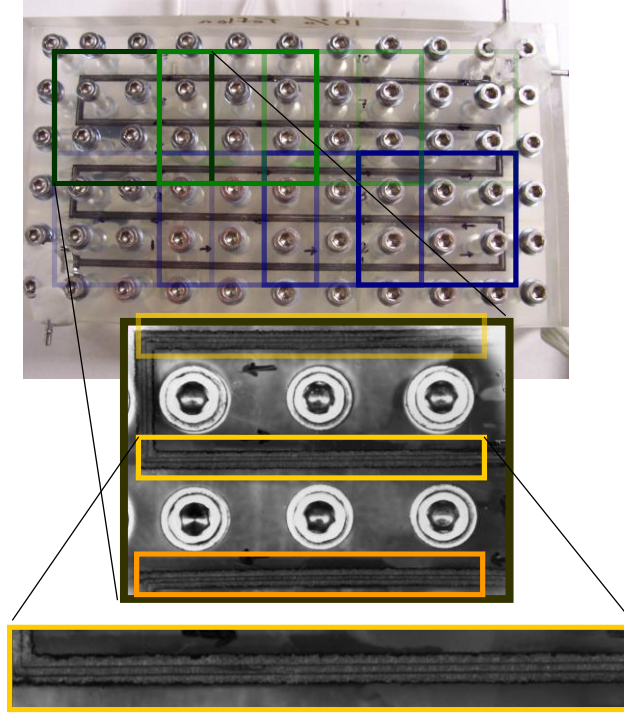


**Figure 4.3: Image decomposition. (a) The entire channel imaged at high demagnification, (b) one of the eight images of the channels, and (c) one channel segment extracted from an image.**

The entire channel is visualized in several images by moving the flow structure with respect to the camera, which is fitted with a macrophotography lens. For the

serpentine channels, eight separate sets of images are collected. Images are decomposed into channel segments, as illustrated in Figure 4.3, in order to examine the flow as it progresses along the length of the channel.

For analysis of the flow regimes, the flow structure in each channel segment was examined and categorized. Figure 4.4 shows representative images of the flow structures that were observed in the channels. Stratified flow is steady and the position of the interface does not vary with time for given operating conditions, while plug and slug flow show transient variation of the air-liquid-solid interfaces. Wavy flow has a constant liquid-solid interface at the channel wall, but a varying liquid-gas interface. For fluidic analysis, local air and water flow rates are calculated along the channel based on the inlet air flow rate and the total quantity of water injected upstream of the imaging location, such that at one test condition, there is a single air flow rate but eight local water flow rates due to the eight water injection locations.

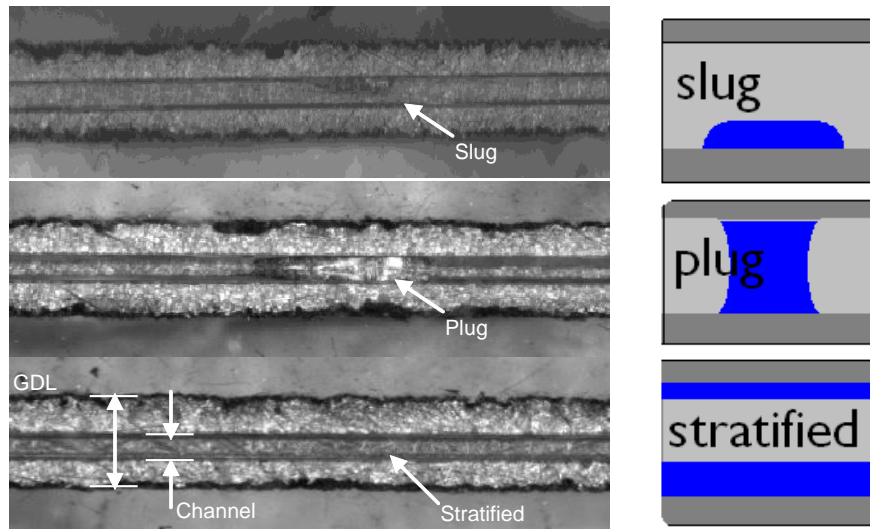


**Figure 4.4: Representative images of two-phase flow structures: slug, plug, stratified.**

## 4.2 Results and discussion

### 4.2.1 General trends

Measurements and images are analyzed to characterize the system performance, channel characteristics, and two-phase flow structures. The channels are characterized using pressure drop and flow rate measurements. Images of the channel under various operating conditions are analyzed to evaluate the evolution of the two-phase flow structure.

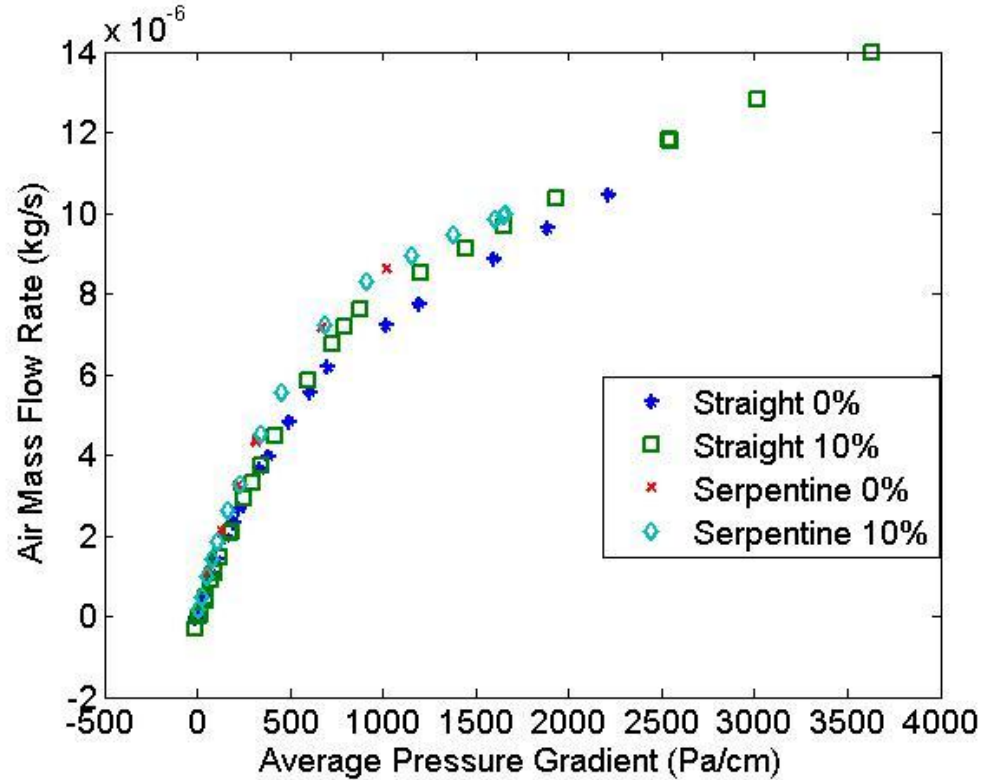
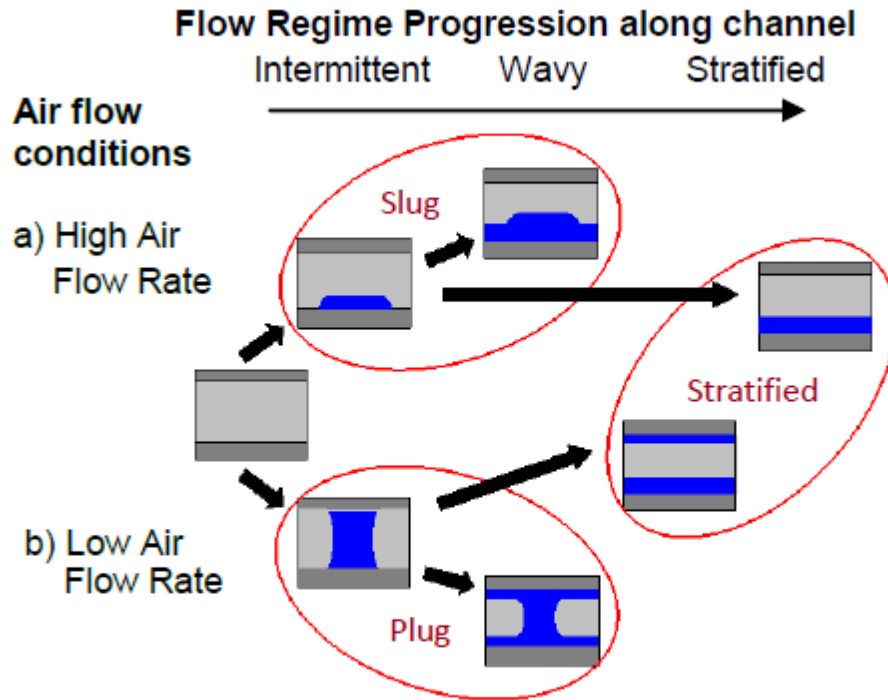


Figure 4.5: Viscous losses in straight and serpentine channels with no water injection. Open symbols indicated teflonated GDL samples. Closed symbols are non-teflonated GDL samples.

The straight and serpentine channels exhibited similar viscous losses as shown in Figure 4.5. Here the average pressure gradient is defined as the total pressure drop divided by the length of the channel. Gas pressure is measured at the inlet and the outlet of the channel. There was no significant difference in the pressure vs. flow rate curves between the two types of GDL tested. The similarity in the viscous loss curves for serpentine and straight channels indicates that minor losses due to the 90 degree corners are not significant. The non-linear relationship between pressure drop and air flow rate indicates that density changes cannot be neglected. However, a variable density relationship using the ideal gas law significantly under predicts the air flow rate for a given pressure drop. Air flow through the gas diffusion layer flanking the channel partially explains this discrepancy. Water introduction caused a very slight decrease in flow rate for a given pressure drop (compared to a dry channel) for both samples.

The flow structure is examined along the length of the channel for each operating condition. As expected, the structure of the liquid water depends upon the properties of the channel wall, the amount of water in the channel, the air flow rate, and to some extent, the distribution of water injection. While there are general trends in the progression of flow regimes and the conditions under which they are observed, a strong stochastic element exists due to the complicated fluidic interactions in the serpentine geometry with a textured, porous wall and non-uniform surface properties. More water is seen in the channels of the structures constructed with GDL containing Teflon. This difference may result from variations in flow structure and liquid water

velocity in the channels or may indicate that more liquid water flows through the hydrophilic GDL so that less water is forced into the channels.



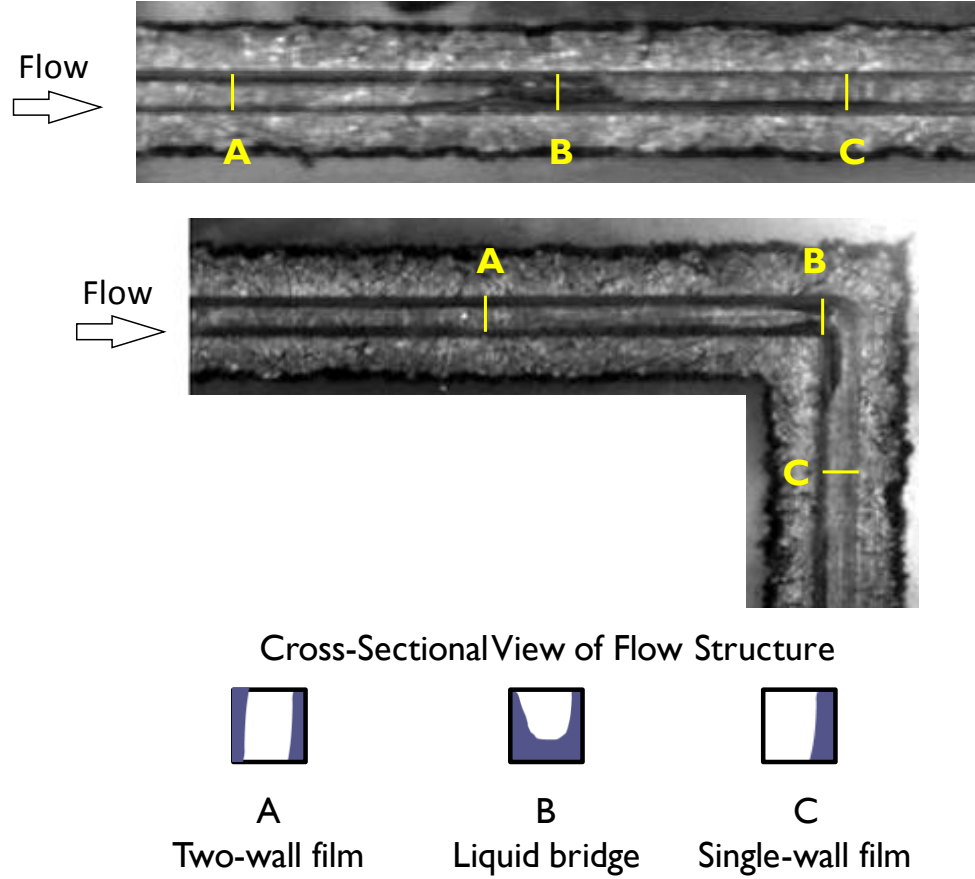
**Figure 4.6: Observed flow structures and general evolution of flow regimes.**

Figure 4.6 provides a qualitative overview of flow structure observations according to air and liquid flow conditions. The horizontal axis corresponds to a progression along the channel and a corresponding increase in local water flow rate as additional liquid injection locations are encountered. The upper and lower branches represent flow structures occurring under relatively higher and lower air flow conditions. Black arrows between images represent common transitions between flow regimes as more liquid is encountered in the channel. The dry channel transitions to intermittent flow, a regime where water moves through the channel in discrete packets droplets, slugs, or

plugs. Intermittent flow becomes wavy flow when the water travels down the channel as an abrupt thickening of a liquid film on the side walls of the channel. Finally, a stratified flow ensues when the sidewall film becomes steady and no significant oscillations are observed at the interface. Stratified flow exists most commonly at the furthest downstream locations, while slug/plug flow is rarely observed downstream of the first several injection locations.

These trends suggest that stratified flow is hydrodynamically preferred to intermittent flow regimes, provided there is enough liquid flowing in the channel to maintain such a film. When a slug or plug travels, the three-phase interface moves so surface tension forces must be overcome. Once the liquid forms a film along a channel wall, this force is eliminated in the flow direction and the gas-liquid surface area is minimized. The water is propelled by the pressure gradient in the channel and shear forces from the air. A liquid film provides the most efficient means of water evacuation from the channels.

One of the most common transitions is a change in structure of stratified flow from occurrence on two channel walls to occurrence on a single wall. Several conditions facilitate this transition, including the presence of liquid resting on the GDL surface, a water injection point which also wets the GDL, or a corner. These liquid bridges may form where local variations in the surface properties of the GDL favor the accumulation of water. Figure 4.7 shows two such transition points, in a straight channel at an injection point and at a corner.



**Figure 4.7: Images of flow transitions from stratified flow on two walls to one wall. Illustrations mark the cross-sectional configuration of the flow deduced from the images.**

This transition is favorable from both a surface-energy-based argument and a hydrodynamic efficiency standpoint. In terms of surface energy, the replacement of one air-water interface with an air-solid interface is energetically favorable if the liquid phase is not completely wetting (if the liquid phase equilibrium contact angle is greater than zero). Neglecting the effect of the film thickness on the side of the channel, the surface energy of a channel with films on two walls is given by

$$2(\gamma + \gamma_{SL}) + 2\gamma_{SO} , \quad (17)$$

while the surface energy of a channel with a film on one wall is given by

$$\gamma + \gamma_{SL} + 3\gamma_{SO}. \quad (18)$$

Comparing these expressions, we find that the surface energy of a two wall stratified flow is great than that of stratified flow in a one wall stratified flow if

$$\gamma > \gamma_{SO} - \gamma_{SL} \quad (19)$$

or, using the definition of the equilibrium contact angle,

$$1 > \cos(\theta_E), \quad (20)$$

a condition which is satisfied for any partially non-wetting surface.

Analytical solutions to the momentum equations for simplified stratified flow in a rectangular channel reveal there is also a hydrodynamic advantage of single-wall stratified flow over two-walled stratified flow. The pressure gradient within a channel of a particular dimension is determined by the ratio of flow rates of air and liquid phases (which is proportional to the stoichiometric ratio) and scales with the absolute magnitude of the flow rate (proportional to current density). After non-dimensionalization, the ratio of pressure gradient to volume flow rate of air is a function of the ratio of water to air volume flow rate (equivalent to fuel cell stoichiometry) and aspect ratio of the channel. The pressure gradient necessary to sustain equivalent flow rates of both gas and liquid in identical square channels is between 4 and 15% lower for stratified flow on a single-wall compared with stratified flow on two walls.



### 4.2.2 *Comparison of flow conditions*

There are several ways to compare the data between test conditions. A comparison of equivalent fuel cell operating conditions is interesting for direct application to fuel cell systems. The stoichiometric ratio fixes the ratio of air and water flow rates; an increase in current density for a fixed value of  $\lambda$  increases both the air and water flow rates proportionally. A constant stoichiometric coefficient corresponds to a line with unity slope on a standard flow regime map with superficial velocities of gas and liquid on the x- and y- axes, respectively.

For channels with teflonated GDL, for a given current density, as the stoichiometric ratio (or air flow rate) increases, the transition from intermittent flow to films occurs later in the channel. As current density increases for equivalent stoichiometric ratios, the transition point occurs further upstream. Alternatively, insight can be gained by comparing equivalent fluidic conditions, where the air flow rate in the channel is held constant, but the water flow rate varies. This simulates the common situation where air flow rate is fixed, but local current density varies in response to the load applied to the cell. As current density increases for equivalent air flow rates, the transition point similarly occurs further upstream.

For non-teflonated channels, the trends are less consistent. For  $i = 0.5 \text{ A cm}^{-2}$  and low air flow rates, water rests in the channel as thin films and as liquid droplets/plugs sitting on the GDL. When the air flow rate increases, slugs are observed and the transition to a film occurs halfway through the channel. For higher water flow rates, slugs are observed for the lower air flow rates and films are observed at high air flow rates. Films occur at highest water flow rates. For equivalent stoichiometric ratios,

the trend is progression from thin films with stationary plugs on the GDL, to moving slugs, to films.

### ***4.2.3 Variation of flow structure with flow rate***

Most two-phase flow studies organize the flow regimes onto regime maps according to the superficial gas and liquid velocities. In this study, the distributed water introduction along the length of the channel requires that the flow regime map consider the local flow rate of liquid after each injection location. Consequently, each experimental condition provides information at eight aligned locations in flow rate space. Furthermore, in this complicated geometry, flow structures often change spatially between injection points, such that a single experimental condition may result in multiple flow regimes for a particular air and local water flow rate, depicted as overlapping points on the regime map. Figure 4.8 shows observed flow regimes plotted against local air and water flow rates. The local water flow rate at a given position is the product of the number of liquid injection points upstream from the imaging location and the rate of water introduction per injection point. The volumetric air flow rate is determined from the inlet mass flow rate and pressure.

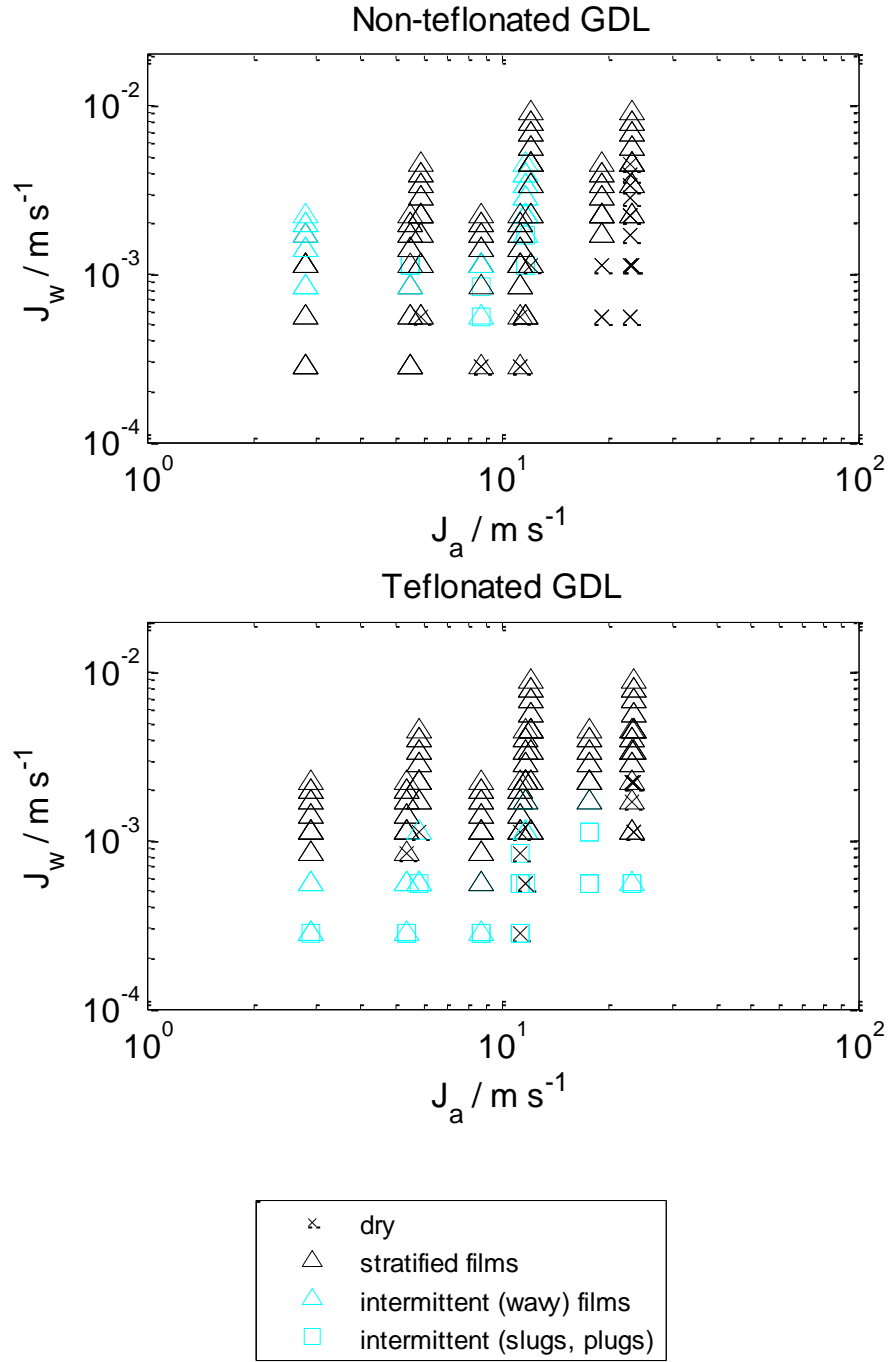


**Figure 4.8: Flow regimes in serpentine channels mapped against superficial air and water velocities. Black symbols represent stable flow regimes, gray symbols represent intermittent flow structures.**

In the samples containing Teflon, intermittent (slug and plug) flow regimes occur for low water injection rates. This corresponds to the first several injection points along a channel. Plug flow occurs at low air flow rates, but slugs exist at the same flow parameters because these plugs are quickly broken into slugs as they travel down the channel. At higher air flow rates, low liquid flow rates yield slug flow. For all air flow rates, stratified flow is the dominant flow regime at high water flow rates.

The samples without Teflon also exhibit stratified flow at the highest liquid flow rates as well as at the highest air flow rates. Intermittent flows are observed at moderate liquid flow rates; plug flow occurs at only under the lowest air flow and slugs occur at moderate air flow. Comparing the regime maps for the serpentine samples, the intermittent regimes occur for higher water flow rates in the hydrophilic GDL case than in the hydrophobic GDL condition. This similarity supports the observation that more liquid water appears in the channels with Teflon coating. Liquid water preferentially flowing through the GDL in the hydrophilic case effectively lowers the water flow rate occurring in the channel.

#### ***4.2.4 Effect of corners on flow regime evolution***

Flow rates for the straight channels were chosen with two equivalencies to the serpentine channels: equivalent fuel cell operating parameters where flow rates are adjusted in proportion to the reduced area of the straight channel, and equivalent hydrodynamics where the flow rates of each phase are identical to the serpentine channel conditions. Matching fluidic conditions in the channels provides a control to examine the effect of the corners on the flow, while matching fuel cell conditions

provides a better comparison for a fuel cell channel design which would include multiple shorter channels in parallel. This section describes the results of matching fluidic conditions. Section 4.2.5 describes the flow regimes which result from the same current density and stoichiometry in each channel.

For matching fluidic conditions, air and water are introduced into the straight channel at the same flow rates as for the serpentine channel, as given in Table 4.1. (This condition corresponds to much higher current densities which would not be practical. This particular analysis therefore relates only to the hydrodynamic effects of the corners on the flow regimes.) The pressure drop in the channel is proportionally smaller than that in a serpentine channel, so the average pressure gradient is comparable for these two channels and pressure forces exerted on droplets and films in the channels are equivalent.

Figure 4.9 is a flow regime map for the straight channel experiments. In these channels, intermittent flow regimes were observed more often than stratified films. In fact, stratified flow was not observed in the straight channel with teflonated GDL under any flow conditions.

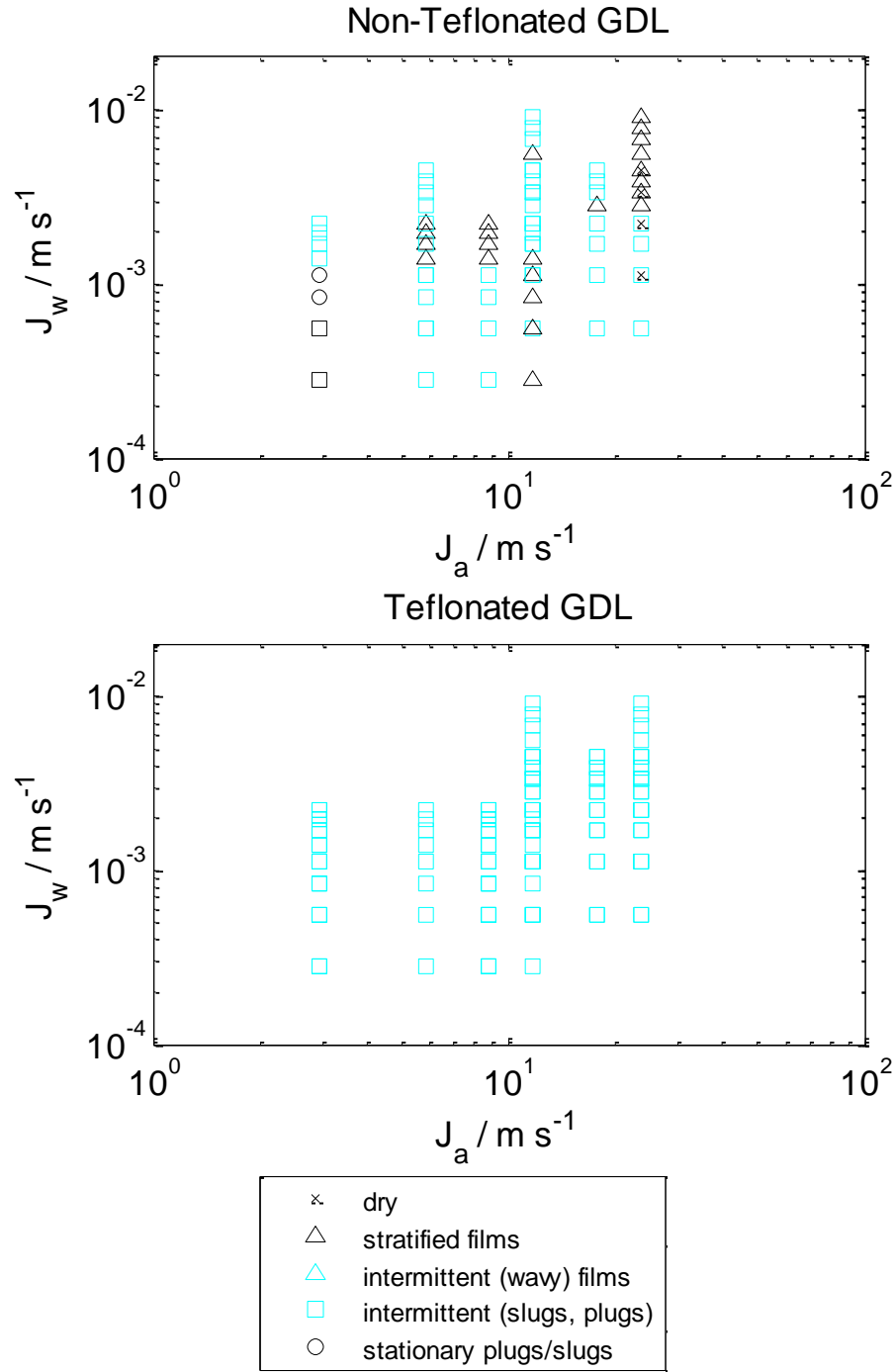


**Figure 4.9: Flow regime map for straight channels with equivalent flow rates to serpentine channel conditions of Figure 4.8. Compared with the serpentine channels, the straight channel configuration tends toward intermittent flow.**

Interestingly, flow regime transitions do not occur at the corner in the serpentine channel samples; however, the flow more frequently transitions to films when corners are present. The effect of the corner, therefore, is to facilitate the formation of films. Possible means for this effect are the build-up of water in the corners, which then facilitates the formation of films when there would otherwise not be enough liquid to sustain a film. When transitions occur at water injection locations, where they most often do, there could be a build-up of water in the GDL or corners of the channel near the injection point that creates conditions favorable to film formation. The corners reduce the water-repellent effect of the teflonated GDL sample by creating locations where water can accumulate and remain in the samples.

This effect is consistent, but less marked in the non-teflonated channels, where the conditions are inherently more favorable for water retention than in the teflonated samples. Unlike the teflonated samples, films and stationary water plugs are observed in the more hydrophilic non-teflonated samples. Films with plugs on the GDL occur at low air flow rates; moving slugs occur when air flow rates are increased. Finally, films occur at the highest air flow rates. These trends are similar to those observed in the serpentine channels, except that slugs are observed over a wider range of operating conditions, specifically for higher air flow rates.

#### ***4.2.5 Implications for fuel cell channel design***

Matching fuel cell operating conditions in a short straight channel gives insight in the effect of length and design of multiple channels for fuel cell gas delivery channels. In these 11 cm samples, the flow rates in the straight channels are 82% lower than

those in the serpentine channels, proportional to the reduction in length according to (15) and (16). Flow rates for the straight channel experiments with equivalent fuel cell operating conditions are listed in Table 4.2. The overall pressure drop and local pressure gradient is also smaller in these channels.

**Table 4.2: Experimental conditions for straight channels with equivalent fuel cell parameters**

I	$Q_w$ $A\ cm^{-2}$	$Q_w/inj.$ $\mu l\ min^{-1}$	$Q_a / Std.\ L\ min^{-1}$			
			Stoich. Coeff.	1	2	3
				4		
0.5	6.16	0.77	0.016	0.032	0.048	0.065
1	12.3	1.54	0.032	0.065	0.097	0.129
2	24.7	3.08	0.065	0.129	0.194	0.258

The reduction in pressure gradient and shear forces due to the reduced flow rates reduces the forces acting on the liquid in the channels. In both the samples with and without Teflon, slugs are stationary near the channel entrance for low air flow rates. Further downstream and after several water injection locations, motion of these slugs ensues. When air flow rates are increased, corresponding to higher stoichiometric ratios or current densities, moving slug flow dominates and water does not remain static in the channels. Slug detachment and its motion downstream is affected by the pressure gradient forces experienced by the liquid slug in the channel so that higher air flow rates create larger pressure forces on the slug [86]. In terms of fuel cell design, this suggests that the higher pressure gradients afforded by high air flow rates could facilitate the removal of liquid water from the gas channels, and multiple parallel



segments which would reduce the local volumetric flow rates and overall system pressure drop might adversely impact water removal from the channels.

Most fuel cell system designs include multiple parallel straight or serpentine gas delivery channels. While these designs decrease the overall pressure drop for a given flow rate of air for a specific plate area, the parallel channels are more prone to flooding as the presence of liquid water in one channel increases flow resistance in that channel, thereby diverting flow into other channels with relatively lower resistances. This is similar to the instabilities documented in parallel two-phase cooling channels, but without the effect of gas expansion during boiling.

In typical single serpentine channel designs, there is cross-talk between channels through the continuous GDL layer [87 88]. This cross-talk reduces the overall pressure drop in the channel and in the entire flow field. Cross-talk also creates zones at channel corners where water is easily trapped or accumulated as flow preferentially shortcuts the corner.

It is interesting to note that flooding of the channel is not observed under any flow conditions during the current studies, likely due to the single channel and sealed GDL configuration chosen for these tests. Where parallel channels provide alternative flow paths for the fluids, this single channel configuration and its larger pressure gradients and air velocities prevent blockage of the channels.

### **4.3 Summary and conclusions**

As one component of the larger water management problem in PEM fuel cells, the design of gas delivery channels is in itself a complicated problem involving many competing phenomena.

In this study, an experimental system was developed to study two-phase flow in microchannels by ex-situ visualization under known liquid and gas flow rates relevant to fuel cells in order to understand the flow conditions which favor particular flow structures in the channel. Images of the channels were collected along the length of the channel as the two-phase flow structure evolved. Flow structure labeling and mapping summarizes the observed flow regimes and the conditions under which they transition from one to another.

The geometric configuration of the channels has a significant effect on the local flow conditions. The gas flow rates are proportional to the entire length of the channel, while the liquid flow is “local”, introduced along the length of the channel. This results in very different local ratios of liquid to gas flow rates depending on channel configuration and number of parallel flow channels.

In particular, the choice of the number of parallel flow channels covering the cell area has a marked effect on the flow conditions in those channels. The water flow in the channel depends on length of channel and reactions occurring under the upstream channels. The air flow rate for the cell is set based on the stoichiometry and the total reaction which will occur in the entire flow field. Along a channel, the ratio of water to air flow rate will vary from zero to the chosen stoichiometry along the length of the

channel. This ratio changes more quickly in the case of multiple parallel channels because the channel lengths are shorter.

Multiple parallel channels reduce the overall pressure drop in the system for a given flow rate (stoichiometric ratio) or, in the case of a given pressure drop, allow more air flow through the channels. But the flow in multiple channels suffers from maldistribution, both inherent variations due to small geometric anomalies and induced redistribution due to the introduction of liquid water droplets [89 90]. These induced flow redistributions can create instabilities for the operation of the fuel cell microchannels. Gas flow is preferentially directed to channels which are not blocked by liquid water slugs, which can further aggravate the flow maldistribution.

Fewer parallel channels mean longer channel lengths. This allows for higher gas velocities in the channel, improving mass transport and enabling removal of water from the channels, but sustaining larger overall pressure drop and gas expansion in a given channel. However, fewer channels in parallel usually necessitate more corners as the channels serpentine to cover the reaction area. As the current study shows, corners trap liquid water and lead to liquid accumulation and film formation in the channels. The choice of channel configuration has a significant effect on the flow structures which occur in the channels.

The results of the current ex-situ experiments provide insight into the effect of channel geometry and corners on the evolution of flow structures in long microchannels relevant to PEM fuel cell operation. It is observed that corners reduce the water-evacuation capability of the channels and facilitate the formation of liquid films on the walls of the channel. At the same time, water is more efficiently removed

from the channels with the larger pressure gradient afforded by high air flow rates through long channels, rather than shorter parallel channels which can result in conditions prone to flooding. These results provide insight for gas delivery channels designed to optimize the performance of PEM fuel cells.

# **Chapter 5. Insights into confocal visualization for two-phase flow**

In order to draw conclusions about the meaning of the data in the previous sections, the analysis has had to make assumptions about the shape of the interface in the third dimension perpendicular to the imaging plane. A three-dimensional imaging technique has been proposed in order to visualize the shape of the interface and fully understand the interaction of the two-phases. In this chapter, we outline the development of a confocal imaging system for two-phase flow systems. We discuss the possibilities and limitations of the use of this technique for the imaging of interfaces.

## **5.1 Basics of Confocal Microscopy**

Confocal microscopy is a technique that allows for three-dimensional imaging. It is most often used for biological applications [91], but has also been implemented for high-resolution particle image velocimetry (PIV) techniques in single phase microfluidic systems and droplets [92 - 95]. Fluidic, diffusive, and thermal

interactions at the interface of stratified liquid-liquid flows have been examined using confocal techniques for two-phases with similar indices of refraction [96-99].

The principle of confocal microscopy relies on the ability of a pinhole aperture in the illumination and detection path of an imaging setup to isolate light originating from a single point in space, or in reality a small region called a voxel. Light originating from any other location is rejected because it is not focused through the pinhole. In the most basic formulation, the sample is scanned through space and a three-dimensional image is reconstructed from the intensity of each of the voxels. This concept was developed by Marvin Minsky in 1955 [100]. The technique is relatively slow and time consuming because a single focal point must be scanned through three-dimensional space with time at each location to capture enough light. A faster variation was developed which allows one focal plane to be imaged at a time, requiring scanning only in the axial dimension. In this implementation, the rejection of out of plane light is achieved by an array of pinholes on a spinning disk. Figure 5.1 illustrates the principle of confocal microscopy for a scanning configuration and for a spinning disk configuration.

There are a few disadvantages to the use of a spinning disk confocal microscopy setup compared with a laser scanning confocal microscope [101] though some post-processing techniques have been suggested to correct the images [102]. There is some loss of resolution and potential for aberrations in the image due to cross-talk between pinholes. By far, however, the biggest challenge is the rejection of light by the pinhole disk. While the scanning system is able to focus light from the source into an area as small as the pinhole, the illumination source for the spinning disk system must

be spread throughout an area large enough to illuminate many pinholes on the disk at one time. The disk typically rejects approximately 99% of the light incident on it. This disk alone significantly increases the requirements for illumination intensity and detection sensitivity.

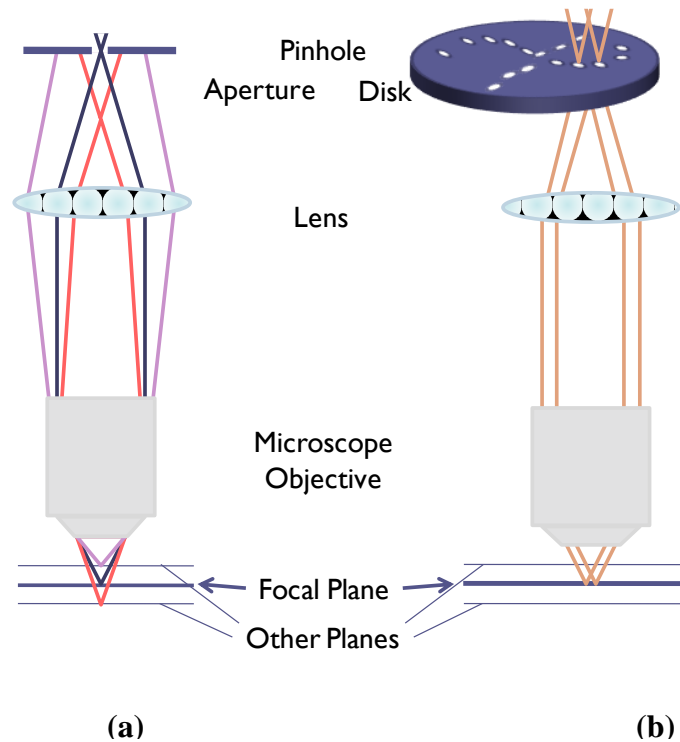


**Figure 5.1: Illustration of confocal imaging principle for (a) laser scanning microscopy and (b) spinning-disk microscopy. The out of plane light is rejected by the pinhole aperture, as shown by the out-of-plane light in (a). The spinning disk implementation passes light from several points in the focal plane through the pinholes in the disk.**

In the implementation of confocal systems employing a microscope, as shown in Figure 5.2, the illumination and detection paths share the same optical path, including the same pinhole apertures. Beam splitters are used to align the incident beam to the

path before the pinhole and divert the detection beam to the detector after the pinhole aperture. The speed of revolution of the disk spinning must be appropriate for the application, including camera frame rate and timescale of fluorescence [103]. The system must be carefully optimized for visualization of unique systems, such as two-phase flow interfaces.

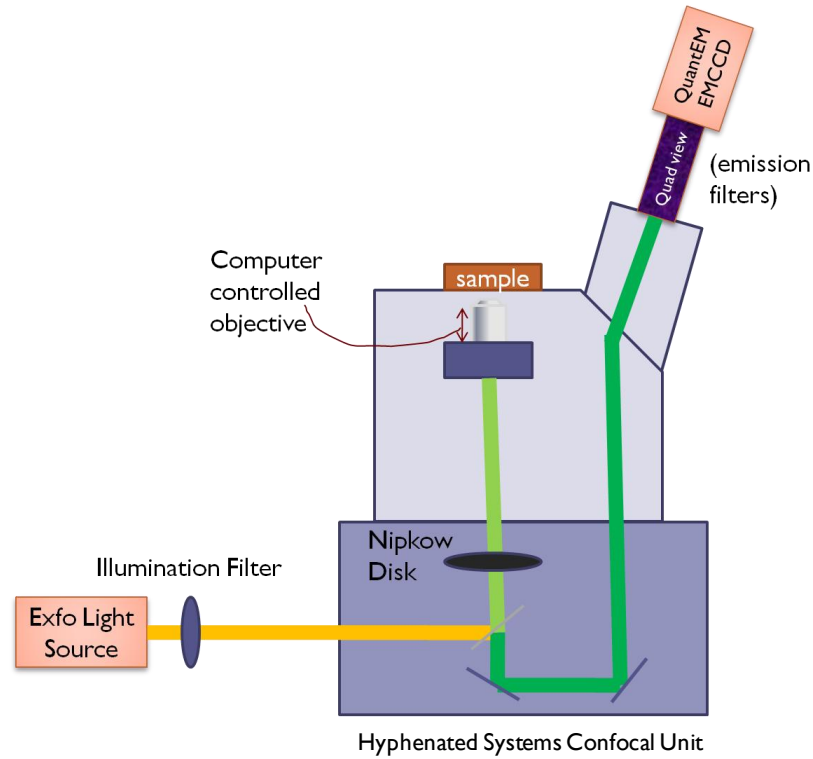


**Figure 5.2: Schematic of spinning disk implementation using Nikon TE2000-U inverted microscope and Hyphenated Systems confocal unit. Illumination and emission filters are external to the system by necessity due to limited flexibility for filters in the configuration.**



## 5.2 Considerations for two-phase flow imaging

In addition to the typical considerations for confocal imaging, which are presented in detail in Müller's handbook [104], imaging of two-phase flow interfaces introduces new challenges to the implementation of this technique. Firstly, the choice of the focusing optics for two-phase flow systems is more challenging and provides less confocal resolution than those suited for typical biological applications, because of the required field of view and desired working distances for fluidic systems. Key metrics are tabulated in Table 5.1. The resolution of the imaging plan in the z-dimension can be approximated with the theoretical full width at half maximum derived from the theoretical point spread function of both the illumination and detection paths of the optical system [91], however this approximation does not account for the expected spreading of the point spread function due to the aberrating effects of the cover glass [105].

$$FWHM_{conf}^z \approx \frac{1}{\sqrt{1 + (\lambda_{exc} / \lambda_{det})^2}} \frac{2n\lambda_{exc}}{(\text{NA})^2}. \quad (21)$$

For more accurate, system-specific calculations of the axial resolution, experimental methods are proposed to calculate the point spread function of the optical system and potentially correct images according to this distortion [106-108].

**Table 5.1: Key parameters for systems traditional for confocal imaging and two-phase systems**

Application	Magnification	Numerical Aperture	Working Distance	Z resolution
Traditional	60x – 100x	0.8-1.4	1 – 500 $\mu\text{m}$	0.5-1 $\mu\text{m}$
Two-phase flow	10x – 20x	0.3-0.5	> 600 $\mu\text{m}$	4-10 $\mu\text{m}$

The axial resolution has an inverse-squared relationship with the numerical aperture of the objective. This causes a significant decrease in the confocal resolution when the types of optics typical for microfluidic applications are used, as they tend to have lower numerical apertures than the high magnification, very short working distance objectives that can be used for biological applications. The longer working distances are required to scan through the depth of a channel and the lower magnification is preferred in order to image the full channel width and larger regions of the channel length in a single scan. The resulting confocal resolution for microfluidic flows is 4  $\mu\text{m}$  – 10  $\mu\text{m}$  unless a higher magnification can be employed.

A more fundamental challenge to the use of confocal microscopy for the imaging of interfaces results from the nature of the interface itself. The difficulty is illustrated in the images shown as Figure 5.3. As a molecularly smooth surface, an air-water interface makes an excellent specular reflector; few other surfaces of interest for imaging applications share this unique property. Special considerations and aberrations introduced when imaging through a liquid film have been addressed [109-111], but these methods do not consider the imaging of a curved interface itself. This

characteristic presents significant difficulties when attempting to image these interfaces in a reflected light mode. When implemented in a microscope setup, the pinhole aperture in the illumination and detection paths is the same. If the illumination is incident on the reflective interface at any angle other than perpendicular to its path, the light will be reflected and refracted away from the detection optics and the image will appear dark for any locations where the illumination path has had to pass through the interface at an angle.

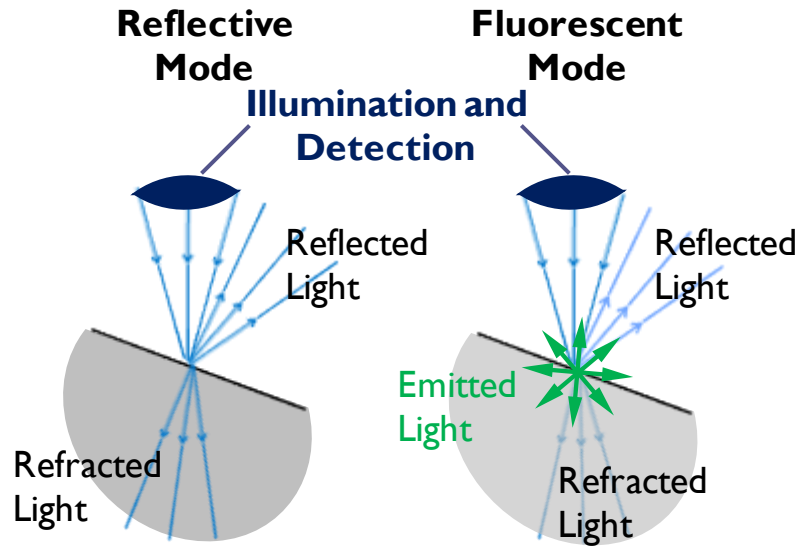


**Figure 5.3: Comparison of optical path for reflected and fluorescent imaging of specularly-reflecting air-water interfaces.**

By employing fluorescence techniques like those discussed in Section 2.2.3 we are able to mitigate this challenge. When the illumination is focused at a location, the fluorescent emission from the dye at that location is emitted diffusely, so a portion of that light will return through the optical path to the detector. Because of reflection off

the interface, some of the incident light will be lost. Because of refraction, the three-dimensional reconstruction of points in the optical path beyond the interface will be distorted, but the location of the first interface in the optical path will appear in the correct location at the detector. Ray tracing methods have been proposed in order to account for the distortion caused by curved interfaces in PIV applications [112 113].

The choice of dye concentration is critical for imaging of microfluidic systems. If the dye concentration is too low, the emission can be too faint for imaging; however, if the dye concentration is too high, the system becomes optically thick and the illumination cannot penetrate through the sample because it is absorbed by the dye at the surface of the fluid, according to Beer's law,

$$I/I_0 = \exp(-\epsilon Cl) \quad (22)$$

where  $\epsilon$  is the molar extinction coefficient of the dye,  $C$  is the dye concentration, and  $l$  is the depth through the thickness. Figure 5.4 demonstrates the effect of improper dye concentration when imaging a droplet on a surface. The dye is expected to be uniformly distributed within the droplet, which should result in a uniform distribution of fluorescent emission in the image of a slice of the droplet, as shown in the image on the right. When the dye concentration is too high, only the dye near the surface of the droplet is able to absorb light and emit fluorescence; a ring of emission appears marking the surface of the droplet rather than the expected disk representing a full slice of the droplet.

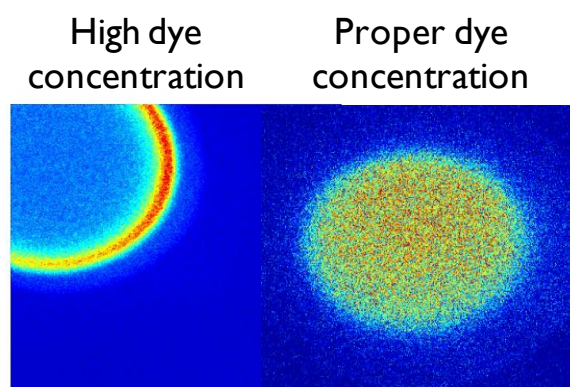


**Figure 5.4: Illustration of the effect of improper dye concentration in two-phase flow imaging using a confocal microscope.**

### 5.3 Demonstration of System

Based on these considerations, an optical system was designed and tested in order to image an air-water interface. The components of the system are shown in Figure 5.2. The Hyphenated Systems K5 confocal unit is a spinning disk confocal setup designed for reflected light imaging of solid surfaces. In order to adapt the setup for fluorescent imaging, the broadband illumination from the Exfo X-Cite metal halide lamp is collimated from the liquid guide, passed through an illumination filter, and refocused into another light guide that directs the light into the confocal unit. The emitted light is filtered just before the detection camera using a band-pass emission filter when one dye is fluorescing, or a quad-view beam splitter to image multiple fluorescent dyes simultaneously, each projected and captured in one quadrant of the camera. A high sensitivity QuantEM electron-multiplying CCD (EMCCD) camera is used to capture images, as the light emission is expected to be a limiting factor in technique. The EMCCD is capable of a multiplication gain up to a factor of 1000.

Using this camera, we were able to capture measureable signal from the fluorescence with an exposure time of 300 ms, whereas the Coolsnap ES and Phantom v7.3 cameras were unable to detect the fluorescence.

The system was demonstrated for a water droplet seeded with fluorescent dye resting on and hanging from a microscope slide. With the system optimized according to the parameters discussed above, an image of a droplet was achieved. The droplet was seeded with 50  $\mu\text{M}$  of Fluorescein dye. The images were captured with a QuantEM CCD camera, using Chroma HQ480/40x and HQ535/50m filters for excitation and emission, respectively. One-hundred thirty image slices were captured with a step size in the vertical dimension of 4  $\mu\text{m}$ . Despite the high sensitivity of the camera and its internal charge-multipliers which greatly improves signal-to-noise ratios and image quality at the detector level, a three-dimensional median filter was needed to produce acceptable signal from the stack of image slices. Figure 5.5 shows the raw data and image processing results. The resulting droplet reconstruction is shown in Figure 5.6.

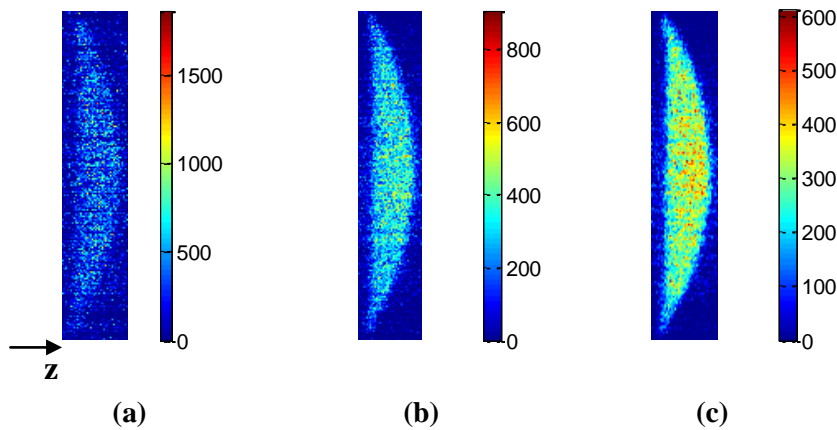


**Figure 5.5: Processing of fluorescent droplet images. Vertical slice of (a) raw data (b) 3 point 3D median filtered data (c) 5-point 3D median filtered data.**

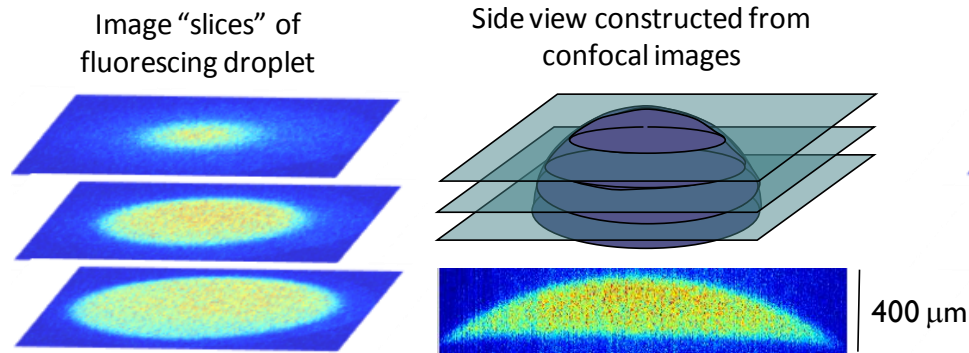


**Figure 5.6: Results of reconstruction of droplet profile from confocal images of planes, or “slices” within the droplet.**

Many attempts were made to image droplets sandwiched between microscope slides, as this flow more closely replicates the geometry and convex interface shape expected for stratified flow in a hydrophilic microchannel. Unfortunately, this interface shape in particular proves very difficult to image using confocal techniques, because the interface scatters light at the edge of the droplet. It may be possible to image half the depth of the droplet, to the location of the interface, but attempts to make this measurement resulted in interface images that were not clearly defined or interpretable. The best method for imaging the shape of an air-water interface is to establish the stratified flow on the top or bottom surface of a channel so that the interface is imaged from above or below. Due to the long exposure times required to collect enough emitted light using the spinning disk-confocal system, the interface must be stable over the duration of the scans, or on the order of seconds based on the current system optimization.

## 5.4 Conclusions

The use of spinning-disk confocal systems for the fluorescent imaging of air-water interfaces faces many challenges. In addition to the considerations faced by any confocal imaging technique in choice of optics and system configuration, two-phase interface imaging requires the use of fluorescent imaging techniques because of the reflectivity of the interface; fluorescence dramatically reduces the percentage of illumination light which can be detected by the sensor. In addition, the reflectivity of the air-water interface renders some sample configurations unable to be imaged and distorts others such that post-processing image deconvolution techniques must be employed to reconstruct the image shape. Some success has been achieved with the use of a high sensitivity electron multiplying CCD camera. Future development of this technique could include the development of test structures whose geometry facilitates the formation of stable films parallel to the imaging plane, as these interfaces are shown to be more accessible with these imaging techniques. Deconvolution techniques could improve the output from reconstructed images, however the fundamental difficulties associated with reflection and refraction at the interfaces will continue to limit the widespread implementation of confocal imaging for air-water interface applications.



## **Chapter 6. Conclusions and future directions**

In this work, we have developed visualization and analysis techniques to probe the interaction of air and water in microchannels applicable to transport phenomena in fuel cells. In silicon microchannels, we examined fundamental two-phase flow phenomena with water introduction from side wall injection slots, simulating the asymmetric water injection in PEM fuel cell channels. We also develop ex-situ fuel cell channels with distributed water injection along a long, serpentine channel through an integrated GDL-wall. Various visualization techniques are used to observe the structure of the flow in order to develop an understanding of the behavior of the two fluids in fuel cell channels.

### **6.1 Fluorescent visualization of two-phase flow regimes in rectangular microchannels**

Using fluorescent visualization techniques to observe two-phase flow in microchannels etched in silicon, we have corroborated and expanded boundaries of

flow regime maps in rectangular channels to high-aspect ratio channels with asymmetric injection conditions. In small square channels, our data corroborates the transition criterion proposed by Cubaud [32] between intermittent and separated flow regimes. However, the asymmetric injection conditions of the current study favor flow stratification; we observed stratified flow in high aspect ratio channels under low air flow conditions where intermittent flow regimes would be expected in square channels. Even in the small square channels, the injection conditions allow formation of stratified flow where annular or dry flow has been observed. Two distinct means of slug formation have been imaged using a high-speed camera which allows for discernment of the interface during the process of flow transition, providing insight into the mechanisms of flow structure formation in these channels. This study represents first-of-kind visualization of two phase flow regimes in channels of various aspect ratios with asymmetric injection, providing key data for the design and optimization of flow channels in practical devices where channel aspect ratio is expected to be an important design parameter.

## **6.2 Stratified flow physics**

High aspect ratio rectangular channels with asymmetric water injection show a propensity toward stratified flow. Several identifiable regimes of stratified flow are observed, depending on the flow conditions, with stationary wavy flow occurring for low air flow rates when surface tension dominates compared with the inertia of the air. As the air flow rates increase, the films smooth. At the highest air flow rates, the

interfaces become blurred. The film thickness was measured using an intensity-thresholding technique. Uncertainty analysis due to variations in the film thickness and in the sharpness of the interface provides insight into the structure of the film and highlights the flow conditions under which transition between stratified regimes occurs. Good agreement between the measured film thicknesses and an analytical solution to the Navier-Stokes equation for the velocity profile of stratified flow in a rectangular channel with a flat air-water interface indicates that this solution is a reasonable approximation to the actual flow in the channels. A key characteristic of the analytical solution is that both the shape of the velocity profile and the fractional thickness of the film are functions only of non-dimensional parameters, including the aspect ratio of the channel and the ratio of the flow rates. This insight allows simplifications in the analysis of channel designs for the optimization of devices in which stratified flow is expected or desired.

### **6.3 Two-phase flow visualization in an ex-situ PEM fuel cell channel**

We have designed an ex-situ fuel cell channel setup to examine the progression of flow structures in long channels with distributed water injection. GDL-integrated samples demonstrate the complexity of interactions in two-phase flow systems with materials exhibiting non-homogeneous surface properties. Flow structures evolve as they move through the channel, encountering water at downstream injection locations. Over a range of conditions chosen to reflect the operating conditions of an operating

fuel cell, the flow consistently transitions from intermittent flow regimes to stable stratified flows downstream, where more water exists in the channels. Under high air flow rate conditions, the water droplets remain attached to one wall, while low air flow rate conditions show droplets spanning the channel width. When the GDL wall is less hydrophobic, less water is observed in the channel, as it is more likely to remain in or flow through the GDL. Experiments were also performed in shorter, straight channels with similar flow rates as the serpentine channels and with similar equivalent fuel cell operating conditions in order to examine the effects of the channel bends to the flow structure. In the straight channels, stratified flow is never observed – the flow remains intermittent along the length of the channel. No flooding conditions are observed in these channels, a result which is explained by the lack of alternative flow paths to the single serpentine channel with no cross-talk between channel segments through the GDL. Implications of the results of these experiments to fuel cell channel design are proposed.

## **6.4 Insights into confocal visualization for two-phase flow**

A confocal fluorescent technique was explored for three-dimensional imaging of the interface shape in two-phase flow systems. While the technique is frequently employed for biological applications and has recently been adapted to fluidic systems, this study reveals that extending its use to two-phase flow systems presents unique challenges and considerations. In particular, the reflective properties of the air-water

interface render reflective imaging unsuitable for these systems, requiring the use of fluorescent techniques to observe the interface, which necessitates higher illumination intensity and a high sensitivity detection camera. The technique is demonstrated for a droplet on a microscope slide seeded with fluorescein dye, and the importance of median filtering to extract information from low signal to noise data is demonstrated. Further development of this technique for other systems is needed, according to the insight gain in this study.

## **6.5 Recommendations for future directions**

Several interesting phenomena have been observed and identified for future research on fundamental phenomena in two-phase microchannel flow. This work presented flow structures and visualization techniques in which asymmetric injection conditions led to the observation of unique flow structures including stratified flow in very small channels and flow transitions leading to the formation of plugs in the channels. High speed visualization provides insight into plug formation, however further development of stability analysis is needed to determine the transition criteria for the formation of plugs both at the water injection t-junction and from the instability of a stratified film where surface tension, viscous forces, and inertial forces may be important.

While the data of this study corroborated the regime transitions of the literature for square channels and suggested the regime boundary trends for channels of higher aspect ratios, a more detailed study is needed to map out this boundary and its

dependence on aspect ratio. A modification of the Weber number for flow transition which accounts for channel geometry may be possible and would provide very valuable insight for the design of practical two-phase flow systems.

Finally, the development of confocal microscopy for two-phase interface detection has not been achieved in the geometries used in this study. Based on the analysis and insights gained during the development of this system, the technique may successfully visualize the shape of an interface of a stable stratified flow if the film were located in the visualization plane. Further exploration of the limitations and capabilities of confocal microscopy in two-phase flow systems may reveal other systems of interest that can be observed using this system.

# Appendix A. Analytical solution to stratified flow in a rectangular channel

## A.1 Procedure

A Fourier Sine Transform solves the incompressible Navier-Stokes equation for the velocity profile of two phase stratified flow with a flat air-water interface in a rectangular channel, as described in [82]. The geometry of the problem is shown in Figure A.1.

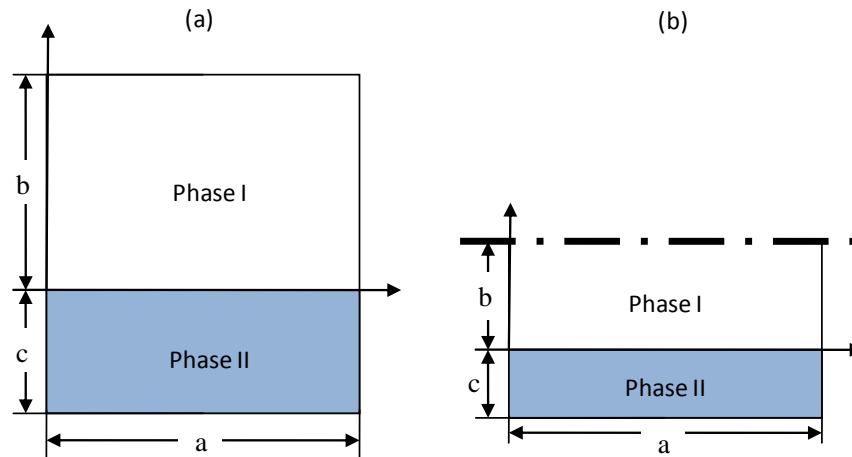


**Figure A.1: Geometry for analytical solution to stratified flow in rectangular channel (a) liquid film on one wall (b) liquid film on two opposite walls**

Assuming steady-state, isothermal flow with constant properties, the momentum equation in each phase is given by

$$\mu_i \nabla^2 w_i = -\frac{\Delta P}{\Delta L}, \quad (23)$$

where subscript i refers to the phase. In this analysis phase 1 is the gas phase, 2 is the liquid phase.

Letting

$$\bar{w} = \int_0^a w \sin \frac{p\pi x}{a} dx, \quad (24)$$

the general forms of the solution to the finite Fourier sine transform to the momentum equation are

$$\bar{w}_1 = A \sinh \left[ \frac{z(b-y)}{a} \right] + B \cosh \left[ \frac{zy}{a} \right] + \frac{2a^3 (\Delta P / \Delta L)}{z^3 \mu_1}, \text{ and} \quad (25)$$

$$\bar{w}_2 = C \sinh \left[ \frac{z(c+y)}{a} \right] + D \cosh \left[ \frac{zy}{a} \right] + \frac{2a^3 (\Delta P / \Delta L)}{z^3 \mu_2}. \quad (26)$$

We apply the boundary conditions given in Table A.1 and the interface conditions given in Table A.2 to solve for the constants in these equations.

**Table A.1: Boundary conditions for stratified flow solution**

Horizontal:	Film on one wall:	Film on two walls:
$\bar{w}_1(0, y) = 0$	$\bar{w}_1(x, b) = 0$	$\frac{d\bar{w}_1}{dy}(x, b) = 0$
$\bar{w}_2(a, y) = 0$	$\bar{w}_2(x, -c) = 0$	$\bar{w}_2(x, -c) = 0$



**Table A.2: Interface conditions for stratified flow solution**

$$\begin{aligned} \text{Velocity:} \quad & \bar{w}_1(0) = \bar{w}_2(0) \\ \text{Shear Stress:} \quad & \mu_1 \frac{d\bar{w}_1}{dy}(0) = \mu_2 \frac{d\bar{w}_2}{dy}(0) \end{aligned}$$

The inverse transform then gives the velocity function for each phase,  $i$

$$w_i = \frac{2}{a} \sum_{n=1}^{\infty} \bar{w}_i \sin \frac{zX}{a}. \quad (27)$$

The solution is written in terms of the dimensional and non-dimensional parameters listed in Table A.3, with the definition of the aspect ratio corresponding to the full channel height, requiring modification of the terms for the symmetry boundary condition in the case of film on two walls.

**Table A.3: Definition of parameters and non-dimensionalizations**

General:	Film on one wall:	Film on two walls:
$z = (2n + 1)\pi$	$\hat{h} = c/(b + c)$	$\hat{h} = c/(b + c)$
$P_2 = \frac{2a^3(\Delta P/\Delta L)}{z^3 \mu_2}$	$AR = (b + c)/a$	$AR = 2(b + c)/a$
$\hat{\mu} = \mu_2/\mu_1$	$\hat{h}AR = c/a$	$\hat{h}AR/2 = c/a$
$\hat{y} = y/a \quad \hat{x} = x/a$	$(1 - \hat{h})AR = b/a$	$(1 - \hat{h})AR/2 = b/a$

The results of the analysis, including the constants which meet the boundary conditions and the velocity profile functions are given in the following sections.

## A.2 Solution for stratified flow with film on one wall

**Constants:**

$$A_n = \hat{\mu} P_2 \beta_n \cosh(z \hat{h} AR)$$

$$B_n = \frac{-\hat{\mu} P_2}{\cosh(z(1 - \hat{h})AR)}$$

$$C_n = -P_2 \beta_n \cosh(z(1 - \hat{h})AR)$$

$$D_n = \frac{-P_2}{\cosh(z \hat{h} AR)}$$

where

$$\beta_n = \frac{\left(1 - \frac{1}{\cosh(z \hat{h} AR)}\right) - \hat{\mu} \left(1 - \frac{1}{\cosh(z(1 - \hat{h})AR)}\right)}{\sinh(z \hat{h} AR) \cosh(z(1 - \hat{h})AR) + \hat{\mu} \cosh(z \hat{h} AR) \sinh(z(1 - \hat{h})AR)}.$$

**Solution to Fourier Sine transform:**

$$\bar{w}_1 = \hat{\mu} P_2 \left[ \frac{\beta_n \cosh(z \hat{h} AR) \sinh(z((1 - \hat{h})AR - \hat{y}))}{1 - \cosh(z \hat{y}) / \cosh(z(1 - \hat{h})AR)} \right]$$

$$\bar{w}_2 = P_2 \left[ -\beta_n \cosh(z(1 - \hat{h})AR) \sinh(z(\hat{h}AR + \hat{y})) + \left(1 - \cosh(z \hat{y}) / \cosh(z \hat{h} AR)\right) \right]$$

### Velocity profile resulting from inverse transform:

$$w_i = \frac{2}{a} \sum_{n=0}^{\infty} \bar{w}_i \sin[z\hat{x}]$$

$$w_1 = \frac{4a^2(\Delta P/\Delta L)}{\mu_2} \sum_{n=0}^{\infty} \hat{\mu} \frac{\sin[z\hat{x}]}{z^3} \left[ \frac{\beta_n \cosh(z\hat{h}AR) \sinh(z((1-\hat{h})AR - \hat{y}))}{1 - \cosh(z\hat{y}) / \cosh(z(1-\hat{h})AR)} \right]$$

$$w_2 = \frac{4a^2(\Delta P/\Delta L)}{\mu_2} \sum_{n=0}^{\infty} \frac{\sin[z\hat{x}]}{z^3} \left[ \frac{-\beta_n \cosh(z(1-\hat{h})AR) \sinh(z(\hat{h}AR + \hat{y}))}{1 - \cosh(z\hat{y}) / \cosh(z\hat{h}AR)} \right]$$

## A.3 Solution for stratified flow with film on two walls

### Constants:

$$\begin{aligned} A_n &= \hat{\mu} P_2 \beta_n \cosh(z\hat{h}AR/2) \\ B_n &= \frac{\hat{\mu} P_2 \beta_n \cosh(z\hat{h}AR/2)}{\sinh(z(1-\hat{h})AR/2)} \\ C_n &= -P_2 \beta_n \cosh(z(1-\hat{h})AR/2) \\ D_n &= \frac{-P_2}{\cosh(z\hat{h}AR/2)} \end{aligned}$$

$$\text{where } \beta_n = \frac{\left(1 - \frac{1}{\cosh(z\hat{h}AR/2)}\right) - \hat{\mu} \left(1 - \frac{1}{\cosh(z(1-\hat{h})AR/2)}\right)}{\sinh\left(\frac{z\hat{h}AR}{2}\right) \cosh\left(\frac{z(1-\hat{h})AR}{2}\right) + \hat{\mu} \cosh\left(\frac{z\hat{h}AR}{2}\right) \sinh\left(\frac{z(1-\hat{h})AR}{2}\right)}.$$

**Solution to Fourier Sine transform:**

$$\bar{w}_1 = \hat{\mu} P_2 \left[ \beta_n \cosh\left(\frac{z\hat{h}AR}{2}\right) \sinh\left(z\left(\frac{(1-\hat{h})AR}{2} - \hat{y}\right)\right) + \frac{\cosh(z\hat{y})}{\sinh\left(\frac{z(1-\hat{h})AR}{2}\right)} + 1 \right]$$

$$\bar{w}_2 = P_2 \left[ -\beta_n \cosh\left(\frac{z(1-\hat{h})AR}{2}\right) \sinh\left(z\left(\frac{\hat{h}AR}{2} + \hat{y}\right)\right) - \frac{\cosh(z\hat{y})}{\cosh\left(\frac{z\hat{h}AR}{2}\right)} + 1 \right]$$

**Velocity profile resulting from inverse transform:**

$$w_i = \frac{2}{a} \sum_{n=0}^{\infty} \bar{w}_i \sin[z\hat{x}]$$

$$w_1 = \frac{4a^2(\Delta P/\Delta L)}{\mu_2} \sum_{n=0}^{\infty} \hat{\mu} \frac{\sin[z\hat{x}]}{z^3} \left[ \beta_n \cosh\left(\frac{z\hat{h}AR}{2}\right) \sinh\left(z\left(\frac{(1-\hat{h})AR}{2} - \hat{y}\right)\right) \dots + \frac{\cosh(z\hat{y})}{\sinh\left(\frac{z(1-\hat{h})AR}{2}\right)} + 1 \right]$$

$$w_2 = \frac{4a^2(\Delta P/\Delta L)}{\mu_2} \sum_{n=0}^{\infty} \frac{\sin[z\hat{x}]}{z^3} \left[ -\beta_n \cosh\left(\frac{z(1-\hat{h})AR}{2}\right) \sinh\left(z\left(\frac{\hat{h}AR}{2} + \hat{y}\right)\right) \dots - \frac{\cosh(z\hat{y})}{\cosh\left(\frac{z\hat{h}AR}{2}\right)} + 1 \right]$$

## A.4 Gas-phase area model

The analytical solution is used to evaluate the limits of validity of the gas-phase area model proposed by [72], in which the liquid is treated by the gas phase as a solid wall with a no slip condition. In this analysis, the volumetric flow rate of the gas phase for the solid wall assumption is compared to the velocity profile of the gas phase from the full solution.

The volumetric flow rate of the gas phase is determined by integrating the velocity profile over the gas region of the channel. The results of the comparison of the profiles are discussed in Section 3.1.2.

The volumetric flow rate and velocity profile for single phase gas flow in a channel where the liquid acts as a solid wall are given by

$$Q_{SP} = a^2 \int_{y=0}^{(1-\hat{h})AR} \int_{x=0}^1 u_{SP,air}(\hat{x}, \hat{y}) d\hat{x} d\hat{y}$$

$$u_{SP} = \frac{4a^2(-dP/dL)}{\mu_1} \sum_{n=0,1,2,\dots}^{\infty} \frac{\sin(z\hat{x})}{z^3} \left( \frac{(\cosh(z(1-\hat{h})AR) - 1) \sinh(z((1-\hat{h})AR - \hat{y}))}{\sinh(z(1-\hat{h})AR) \cosh(z(1-\hat{h})AR)} \dots \right) + \frac{\cosh(z\hat{y})}{\cosh(z(1-\hat{h})AR)} - 1$$

The volumetric flow rate of the gas phase from the full two-phase velocity profile solution described in Section A.1 and A.2 is given by

$$Q_{TP} = a^2 \int_{y=0}^{(1-\hat{h})AR} \int_{x=0}^1 u_{TP,air}(\hat{x}, \hat{y}) d\hat{x} d\hat{y}$$

$$u_{TP} = \frac{4a^2(-dP/dL)}{\mu_1} \sum_{n=0,1,2,\dots}^{\infty} \frac{\sin(z\hat{x})}{z^3} \left( \beta_n \cosh(z\hat{h}AR) \left( \frac{\sinh(z((1-\hat{h})AR/2 - \hat{y}))}{\cosh(z\hat{h}AR)} + \frac{\cosh(z\hat{y})}{\sinh(z(1-\hat{h})AR)} \right) + 1 \right)$$

$$\text{where } \beta_n = \frac{\left(1 - \frac{1}{\cosh(z\hat{h}AR)}\right) - \hat{\mu} \left(1 - \frac{1}{\cosh(z(1-\hat{h})AR)}\right)}{\sinh(z\hat{h}AR) \cosh(z(1-\hat{h})AR) + \hat{\mu} \cosh(z\hat{h}AR) \sinh(z(1-\hat{h})AR)}.$$

## References

- 1 H. Li, Y. Tang, Z. Wang, Z. Shi, S. Wu, D. Song, J. Zhang, K. Fatih, J. Zhang, H. Wang, Z. Liu, R. Abouatallah, A. Mazza, A review of water flooding issues in the proton exchange membrane fuel cell, *J. Power Sources* 178 (2008) 103–117.
- 2 F. Barbir, H. Gorgun, X. Wang, Relationship between pressure drop and cell resistance as a diagnostic tool for PEM fuel cells, *J. Power Sources* 141 (2005) 96–101.
- 3 T.V. Nguyen, M.W. Knobbe, A liquid water management strategy for PEM fuel cell stacks, *J. Power Sources* 114 (2003) 70-79.
- 4 J.P.Owejan, T.A. Trabold, J.J. Gagliardo, D.L. Jacobson, R.N. Carter, D.S. Hussey, M. Arif, Voltage instability in a simulated fuel cell stack correlated to cathode water accumulation, *J. Power Sources* 171 (2007) 626-633.
- 5 W. He, G. Lin, T. Van Nguyen, Diagnostic tool to detect electrode flooding in proton-exchange-membrane fuel cells, *AIChE Journal* 49 (2003) 3221-3228.
- 6 M. Müller, C. Müller, F. Gromball, M. Wölfe, W. Menz, Micro-structure flow field for small fuel cells, *Microsystem Tech.* 9 (2003) 159-162.

- 7 S.W. Cha, R. O'Hayre, F.B. Prinz, The influence of size scale on the performance of fuel cells, *Solid State Ionics* 175 (2004) 789–795.
- 8 S.W. Cha, R. O'Hayre, S.J. Lee, Y. Saito, F.B. Prinz, Geometric scale effect of flow channels on performance of fuel cells, *J. Electrochemical Society* (2004) A1856-A1864.
- 9 S.E. Litster, C.R. Buie, T. Fabian, J.K. Eaton, J.G. Santiago, Active Water Management for PEM fuel cells, *J. Electrochem. Society* 154 (2007) B1049-B1058 .
- 10 S.E. Litster, C.R. Buie, J.G. Santiago, Engineering model for coupling wicks and electroosmotic pumps with proton exchange membrane fuel cells for active water management, *Electrochimica Acta* 54 ( 2009) 6223-6233.
- 11 D.G. Strickland, J.G. Santiago, *In situ* polymerized wicks for passive water management in proton exchange membrane fuel cells, *J. Power Sources* 195 (2010) 1667-1675.
- 12 R.S. Stanley, R.F. Barron, T.A. Ameel, Two-phase flow in microchannels, *ASME Microelectromechanical Systems* DSC-62 (2007) 143-152.
- 13 J. Moreno Quibén, J.R. Thome, Flow pattern based two-phase frictional pressure drop model for horizontal tubes, Part II: new phenomenological model, *Int. J. Heat Fluid Flow* 28 (2007) 1060-1072.
- 14 D.R. Kim, J.-M. Koo, C. Fang, J.E. Steinbrenner, E.S. Lee, F.-M. Wang, C.H. Hidrovo, J.K. Eaton, K.E. Goodson, Compact model of slug flow in microchannels, *Proc. of ICNMM (18-20 June 2007) Puebla, Mexico*.



- 15 P.-G. de Gennes, F. Brochard-Wyart, D. Quéré, *Capillarity and Wetting Phenomena: Drops, Bubbles, Pearls, Waves* (2004) Springer-Verlag, New York, Inc., USA.
- 16 T. Cubaud, M. Fermigier, Advancing contact lines on chemically heterogeneous surfaces, *J. Colloid and Interface Sci.* 269 (2004) 171-177.
- 17 M.A. Tenan, S. Hackwood, G. Beni, Friction in capillary systems, *J. Appl. Phys.* 53 (1982) 6687-6692.
- 18 C. Fang, C.H. Hidrovo, F.-M. Wang, J.K. Eaton, K.E. Goodson, 3-D numerical simulation of contact angle hysteresis for microscale two phase flow, *Int. J. Multiphase Flow* 34 (2008) 690-705.
- 19 T. Cubaud, U. Ulmanella, C.-M. Ho, Two-phase flow in microchannels with surface modifications, Plenary Paper, ICMF (30 May – 4 June 2004) Yokohama, Japan.
- 20 K.S. Chen, M.A. Hickner, D.R. Noble, Simplified models for predicting the onset of liquid water droplet instability at the gas diffusion layer/gas flow channel interface, *Int. J. Energy Research* 29 (2005) 1113-1132.
- 21 A. Serizawa, Z. Feng, Z. Kawara, Two-phase flow in microchannels, *Exp. Thermal Fluid Sci.* 26 (2002) 703-714.
- 22 A. Kawahara, P.M.-Y. Chung, M. Kawaji, Investigation of two-phase flow pattern, void fraction and pressure drop in a microchannel, *Int. J. Multiphase Flow* 28 (2002) 1411-1435.
- 23 M.K. Akbar, D.A. Plummer, S.M. Ghiaasiaan, On gas-liquid two-phase flow regimes in microchannels, *Int. J. Multiphase Flow* 29 (2003) 855-865.

- 24 S. Saisorn, S. Wongwises, Flow pattern, void fraction and pressure drop of two-phase air-water flow in a horizontal circular micro-channel, *Exp. Thermal and Fluid Sci.* 32 (2008) 748-760.
- 25 S. Saisorn, S. Wongwises, The effects of channel diameter on flow pattern, void fraction and pressure drop of two-phase air-water flow in circular micro-channels, *Exp. Thermal and Fluid Sci.* 34 (2010) 454-462.
- 26 M. Kawaji and P. M.-Y. Chung, Adiabatic gas-liquid flow in microchannels, *Microscale Thermophysical Engineering* 8 (2004) 239-257.
- 27 I. Hassan, M. Vaillancourt, K. Pehlivan, Two-phase flow regime transitions in microchannels: A comparative experimental study, *Microscale Thermophysical Engineering* 9 (2005) 165-182.
- 28 R. Dreyfus, P. Tabeling, H. Willaime, Ordered and disordered patterns in two-phase flow in microchannels, *Physical Review Letters* 90 (1993) 144505-(1-4).
- 29 K.A. Triplett, S.M. Ghiaasiaan, S.I. Abdel-Khalik, D.L. Sadowski, Gas-liquid two-phase flow in microchannels Part I: two-phase flow patterns, *Int. J. Multiphase Flow* 25 (1999) 377-394.
- 30 J.L. Xu, P. Cheng, T.S. Zhao, Gas-liquid two-phase flow regimes in rectangular channels with mini/micro gaps, *Int. J. Multiphase Flow* 25 (1999) 411-432.
- 31 K. Pehlivan, I. Hassan, M. Vaillancourt, Experimental study on two-phase flow and pressure drop in millimeter-size channels, *Applied Thermal Engineering* 26 (2006) 1506-1514.
- 32 T. Cubaud, C.-M. Ho, Transport of bubbles in square microchannels. *Physics of Fluids* 16 (2004) 4575-4584.

- 
- 33 P. M.-Y. Chung, M. Kawaji, A. Kawahara, Y. Shibati, Two-phase flow through square and circular microchannels – effects of channel geometry, *J. Fluids Engineering* 126 (2004) 546-552.
  - 34 Q.C. Bi, T.S. Zhao, Taylor bubbles in miniaturized circular and noncircular channels, *Int. J. Multiphase Flow* 27 (2001) 561-570.
  - 35 S. Garimella, J.D. Killion, J.W. Coleman, An experimentally validated model for two-phase pressure drop in the intermittent flow regime for noncircular microchannels, *J. Fluids Eng.* 125 (2003) 887-894.
  - 36 T.C. Ransohoff, C.J. Radke, Laminar flow of a wetting liquid along the corners of a predominantly gas-occupied noncircular pore, *J. Colloid Int. Sci.* 121 (1988) 392-401.
  - 37 H. Wong, C.J. Radke, S. Morris, The motion of long bubbles in polygonal capillaries. Part 2. Drag, fluid pressure, and fluid flow, *J. Fluid. Mech.* 292 (1995) 95-110.
  - 38 A.M. Barajas, R.L. Panton, The effects of contact angle on two-phase flow in capillary tubes, *Int. J. Multiphase Flow* 19 (1993) 337-346.
  - 39 C.Y. Lee, S.Y. Lee, Influence of surface wettability on transition of two-phase flow pattern in round mini-channels, *Int. J. Multiphase Flow* 34 (2008) 706-711.
  - 40 N.J. English, S.G. Kandlikar, An experimental investigation into the effect of surfactants on air-water two-phase flow in minichannels, *Proc. of ICMF* (13-15 June 2005) Toronto, Canada.
  - 41 A. Bazylak, Liquid water visualization in PEM fuel cells: A review, *Int. J. Hydrogen Energy* 34 (2009) 3845-3857.

- 42 R. Anderson, L. Zhang, Y. Ding, M. Blanco, X. Bi, D.P. Wilkinson, A critical review of two-phase flow in gas flow channels of proton exchange membrane fuel cells, *J. Power Sources* 195 (2010) 4531–4553.
- 43 D. Kramer, J. Zhang, R. Shimoï, E. Lehmann, A. Wokaun, K. Shinohara, G.G. Scherer, In situ diagnostic of two-phase flow phenomena in polymer electrolyte cells by neutron imaging – Part A. Experimental, data treatment, and quantification, *Electrochem. Acta* 50 (2005) 2603–2614.
- 44 D.S. Hussey, D.L. Jacobson, M. Arif, J.P. Owejan, J.J. Gagliardo, T.A. Trabold, Neutron images of the through plane water distribution of an operating PEM fuel cell, *J. Power Sources* 172 (2007) 225–228.
- 45 T.A. Trabold, J.P. Owejan, D.L. Jacobson, M. Arif, P.R. Huffman, In situ investigation of water transport in an operating PEM fuel cell using neutron radiography: Part 1 – Experimental method and serpentine flow field results, *Int. J. Heat Mass Transfer* 49 (2006) 4712–4720.
- 46 P. Boillat, G. Frei, E. H. Lehmann, G.G. Scherer, A. Wokaun, Neutron imaging resolution improvements optimized for fuel cell applications, *Electrochem. and Solid State Letters* 13 (2010) B25-B27.
- 47 N. Pekula, K. Heller, P.A. Chuang, A. Turhan, M.M. Mench, J.S. Brenizer, K. Unlu, Study of water distribution and transport in a polymer electrolyte fuel cell using neutron radiography, *Nucl. Instrum. Meth. Phys. Res. A* 21 (2005) 134.
- 48 X. Li, I. Sabir, J. Park, A flow channel design procedure for PEM fuel cells with effective water removal, *J. Power Sources* 163 (2007) 933-942.

- 
- 49 J.P. Owejan, T.A. Trabold, D.L. Jacobson, M. Arif, S.G. Kandlikar, Effects of flow field and diffusion layer properties on water accumulation in a PEM fuel cell, *Int. J. Hydrogen Energy* 32 (2007) 4489-4502.
- 50 J. Zhang, D. Kramer, R. Shimo, Y. Ono, E. Lehmann, A. Wokaun, K. Shinohara, G.G. Scherer, In situ diagnostic of two-phase flow phenomena in polymer electrolyte fuel cells by neutron imaging Part B. Material variations, *Electrochimica Acta* 51 (2006) 2715-2727
- 51 R. Satija, D.L. Jacobson, M. Arif, S.A. Werner, In-situ neutron imaging technique for evaluation of water management systems in operating PEM fuel cells, *J. Power Sources* 129 (2004) 238-245.
- 52 I. Manke, Ch. Hartnig, M. Grünerbel, J. Kaczerowski, W. Lehnert, N. Kardjilov, A. Hilger, J. Banhart, W. Treimer, M. Strobl, Quasi-*in situ* neutron tomography on polymer electrolyte membrane fuel cell stacks, *Applied Physics Letters* 90 (2007) 184101.
- 53 I. Manke, Ch. Hartnig, M. Grünerbel, W. Lehnert, N. Kardjilov, A. Heibel, A. Hilger, J. Banhart, H. Riesemeier, Investigation of water evolution and transport in fuel cells with high resolution synchrotron x-ray radiography, *Applied Physics Letters* 90 (2007) 174105.
- 54 S.J. Lee, N.-Y. Lim, S. Kim, G.-G. Park, C.-S. Kim, X-ray imaging of water distribution in a polymer electrolyte fuel cell, *J. Power Sources* 185 (2008) 867-870.
- 55 S. Tsushima, K. Teranishi, S. Hirai, Magnetic resonance imaging of the water distribution within a polymer electrolyte membrane in fuel cells, *Electrochem. Solid- State Lett.* 7 (2004) A269-A272.

- 56 P.K. Sinha, P. Halleck, C.-Y. Wang, Quantification of liquid water saturation in a PEM fuel cell diffusion medium using X-ray microtomography, *Electrochem. Solid State Lett.* 9 (2006) A344-A348.
- 57 K. Tuber, D. Pocza, C. Hebling, Visualization of water buildup in the cathode of a transparent PEM fuel cell, *J. Power Sources* 124 (2003) 403–414.
- 58 D. Spornjak, S.G. Advani, A.K. Prasad, Simultaneous neutron and optical imaging in PEM fuel cells, *J. Electrochemical Society* 156 (2009) B109-B117.
- 59 X.G. Yang, F.Y. Zhang, A.L. Lubawy, C.Y. Wang, Visualization of liquid water transport in a PEFC. *Electrochem. Solid State Lett.* 7 (11) (2004) 408–411.
- 60 X. Liu, H. Guo, F. Ye, C.F. Ma, Water flooding and pressure drop characteristics in flow channels of proton exchange membrane fuel cells, *Electrochimica Acta* 52 (2007) 3607–3614.
- 61 A. Hakenjos, H. Muentert, U. Wittstadt, C. Hebling, A PEM fuel cell for combined measurement of current and temperature distribution, and flow field flooding, *J. Power Sources* 131 (2004) 213–216.
- 62 E. Kimball, T. Whitaker, Y.G. Kevrekidis, J.B. Benziger, Drops, slugs, and flooding in polymer electrolyte membrane fuel cells, *AIChE Journal* 54 (2008) 1313-1332.
- 63 F.B. Weng, A. Su, C.Y. Hsu, The study of the effect of gas stoichiometric flow rate on the channel flooding and performance in a transparent fuel cell, *Int. J. of Hydrogen Energy* 32 (2007) 666-676.
- 64 T. Ous, C. Arcoumanis, Visualisation of water droplets during the operation of PEM fuel cells, *J. Power Sources* 173 (2007) 137–148.

- 
- 65 D. Spornjak, A.K. Prasad, S.G. Advani, Experimental investigation of liquid water formation and transport in a transparent single-serpentine PEM fuel cell, *J. Power Sources* 170 (2007) 334–344.
- 66 Z. Lu, S.G. Kandlikar, C. Rath, M. Grimm, W. Domigan, A.D. White, M. Hardbarger, J.P. Owejan, T.A. Trabold, Water management studies in PEM fuel cells, Part II: Ex situ investigation of flow maldistribution, pressure drop and two-phase flow pattern in gas channels, *Int. J. of Hydrogen Energy* 34 (2009) 3445-3456.
- 67 L. Zhang, H.T. Bi, D.P. Wilkinson, J. Stumper, H. Wang, Gas-liquid two-phase flow patterns in parallel channels for fuel cells, *J. Power Sources* 183 (2008) 643-650.
- 68 A. Su, F.B. Weng, C.Y. Hsu, Y.M. Chen, Studies on flooding in PEM fuel cell cathode channels, *Int. J. of Hydrogen Energy* 31 (2006) 1031-1039.
- 69 J. Benziger, J. Nehlsen, D. Blackwell, T. Brennan, J. Itescu, Water flow in the gas diffusion layer of PEM fuel cells, *J. Membr. Sci.* 261 (2005) 98–106.
- 70 J. Stumper, C. Stone, Recent advances in fuel cell technology at Ballard, *J. Power Sources* 176 (2008) 468– 476.
- 71 B. Gao, T.S. Steenhuis, Y. Zevi, J.-Y. Parlange, R.N. Carter, T.A. Trabold, Visualization of unstable water flow in a fuel cell gas diffusion layer, *J. Power Sources* 190 (2009) 493-498.
- 72 E.S. Lee, Water transport in two-phase fuel cell microchannels, PhD Thesis (2007) Stanford University.
- 73 F.M. Wang, J.E. Steinbrenner, C.H. Hidrovo, T.A. Kramer, E.S. Lee, S. Vigneron, J.K. Eaton, K.E. Goodson, Microfabricated experimental structures

- for the investigation of two-phase transport phenomena in microchannels, Heat SET (5-7 April 2005) Grenoble, France. Applied Thermal Engineering 27 (2007) 1728-1733.
- 74 P.A. Gauglitz, C.J. Radke, An extended evolution equation for liquid film breakup in cylindrical capillaries, Chemical Engineering Science 43 (1988) 1457-1465.
- 75 Y. Taitel, A.E. Dukler, A model for slug frequency during gas-liquid flow in horizontal and near horizontal pipes, Int. J. Multiphase Flow 3 (1977) 585-596.
- 76 D. Barnea, Y. Taitel, Interfacial and structural stability of separated flow, Int. J. Multiphase Flow 20 (1994) 387-414.
- 77 Y. Taitel, A.E. Dukler, A model for predicting flow regime transitions in horizontal and near horizontal gas-liquid flow, AIChE Journal 22 (1976) 47-55.
- 78 J. Biswas, P.F. Greenfield, Two phase flow through vertical capillaries – existence of a stratified flow pattern, Int. J. Multiphase Flow 11 (1985) 553-563.
- 79 D. Barnea, Y. Luninski, Y. Taitel, Flow pattern in horizontal and vertical two phase flow in small diameter pipes, Canadian J. Chem. Engineering 61 (1983) 617- 620.
- 80 J.F. Zhao, W.R. Hu, Slug to annular flow transition of microgravity two-phase flow, Int. J. Multiphase Flow 26 (2000) 1295-1304.
- 81 J.E. Steinbrenner, C.H. Hidrovo, F.-M. Wang, S. Vigneron, E.S. Lee, T.A. Kramer, C.-H. Cheng, J.K. Eaton, K.E. Goodson, Measurements and modeling of liquid film thickness evolution in stratified two-phase microchannel flows, Proc. of HeatSET (April 5-7, 2005) Grenoble, France. Applied Thermal Engineering 27 (2007) 1722-1727.



- 
- 82 Y.P. Tang, D.M. Himmelblau, Velocity distribution for isothermal two-phase co-current flow in a horizontal rectangular duct, *Chemical Engineering Science* 18 (1963) 143-148.
- 83 J.E. Steinbrenner, E.S. Lee, F.M. Wang, C. Fang, C.H. Hidrovo, K.E. Goodson, Flow regime evolution in long, serpentine microchannels with a porous carbon paper wall, *Proc. of IMECE* (November 2-6, 2008) Boston, Massachusetts, USA.
- 84 J.E. Steinbrenner, E.S. Lee, C.H. Hidrovo, J.K. Eaton, K.E. Goodson, Impact of channel geometry on two-phase flow in fuel cell microchannels, *J. Power Sources* (2011), in press.
- 85 J.J. Kowal, A. Turhan, K. Heller, J. Brenizer, M.M. Mench, Liquid water storage, distribution, and removal from diffusion media in PEFCs, *J. Electrochem. Soc.* 153 (2006) A1971-A1978.
- 86 C.H. Hidrovo, F.-M. Wang, J.E. Steinbrenner, E.S. Lee, S. Vigneron, C.-H. Cheng, J.K. Eaton, K.E. Goodson, Water slug detachment in two-phase hydrophobic microchannel flows, *Proc. of ICMM* (June 13-15, 2005) Toronto, Canada.
- 87 J.P. Feser, A.K. Prasad, S.G. Advani, Particle image velocimetry measurements in a model proton exchange membrane fuel cell, *J. Fuel Cell Sci. Tech.* 4 (2007) 328-335.
- 88 J. Martin, P. Oshkai, N. Djilali, Flow structures in a U-shaped fuel cell flow channel: Quantitative visualization using particle image velocimetry, *J. Fuel Cell Sci. Tech.* 2 (2005) 70-80.

- 89 A. Lozano, F. Barreras, L. Valino, C. Marin, Imaging of gas flow through a porous medium from a fuel cell bipolar plate by laser-induced fluorescence, *Exp. Fluids* 42 (2007) 301-310.
- 90 F. Barreras, A. Lozano, L. Valino, C. Marin, A. Pascau, Flow distribution in a bipolar plate of a proton exchange membrane fuel cell: experiments and numerical simulation studies, *J. Power Sources* 144 (2005) 54-66.
- 91 S. Paddock, ed. *Methods in Molecular Biology*, vol. 122: *Confocal Microscopy Methods and Protocols* (1998) Humana Press Inc, Totowa, NJ.
- 92 J.S. Park, K.D. Kihm, Use of confocal laser scanning microscopy (CLSM) for depthwise resolved microscale-particle image velocimetry ( $\mu$ -PIV), *Optics and Lasers in Engineering* 44 (2006) 208-223.
- 93 L.E. Rodd, S.T. Huntington, K. Lyytikainen, D.V. Boger, J.J. Cooper-White, The effect of surface character on flows in microchannels, *Proc. of SPIE* 5275 (2004) 114-122.
- 94 H. Kinoshita, S. Kaneda, T. Fujii, M. Oshima, Three-dimensional measurement and visualization of internal flow of a moving droplet using confocal micro-PIV, *Lab on a Chip* 7 (2007) 338-346.
- 95 R. Lima, S. Wada, M. Takeda, K. Tsubota, T. Yamaguchi, In vitro confocal micro-PIV measurements of blood flow in a square microchannel: The effect of the haematocrit on instantaneous velocity profiles, *J. Biomechanics* 40 (2007) 2752-2757.
- 96 Y. Yamaguchi, F. Takagi, T. Watari, K. Yamashita, H. Nakamura, H. Shimizu, H. Maeda, Interface configuration of the two layered laminar flow in a curved microchannel, *Chemical Engineering Journal* 101 (2004) 367-372.

- 
- 97 R.F. Ismagilov, A.D. Stroock, P.J.A. Kenis, G. Whitesides, H.A. Stone, Experimental and theoretical scaling laws for transverse diffusive broadening in two-phase laminar flows in microchannels, *Applied Physics Letters* 76 (2000) 2376- 2378.
- 98 D.G.A.L. Aarts, M. Schmidt, H.N.W. Lekkerkerker, Direct visual observation of thermal capillary waves, *Science* 304 (2004) 847-850.
- 99 M. Ichiyanagi, Y. Sato, K. Hishida, Optically sliced measurement of velocity and pH distribution in microchannel, *Exp. Fluids* 43 (2007) 425 – 435.
- 100 M. Minsky, Memoir on Inventing the Confocal Scanning Microscope, *Scanning* 10 (1988) 128-138.
- 101 D.T. Fewer, S.J. Hewlett, E.M.McCabe, Laser sources in direct-view-scanning, tandem-scanning, or Nipkow-disk-scanning confocal microscopy, *Applied Optics* 37 (1998) 380-385.
- 102 S. Inoué, T. Inoué, Digital unsharp masking reveals fine detail in images obtained with new spinning-disk confocal microscope, *Biol. Bull.* 191 (1996) 269-270.
- 103 F.K. Chong, C.G. Coates, D.J. Denvir, N. McHale, K. Thornbury, M. Hollywood, Optimization of spinning disk confocal microscopy: Synchronization with the ultra-sensitive EMCCD, *Three-Dimensional and Multidimensional Microscopy, Image Acquisition and Processing XI*, Proc. of SPIE 5324 (2004) 65-76.
- 104 M. Müller, *Introduction to Confocal Fluorescence Microscopy* (2006) SPIE Press, Bellingham, Washington.

- 105 O. Haeberlé, Focusing of liquid through a stratified medium: a practical approach for computing microscope point spread functions – Part II: confocal and multiphoton microscopy, *Optics Communication* 235 (2004) 1-10.
- 106 M. Schrader, U.G. Hofmann, S.W. Hell, Ultrathin fluorescent layers for monitoring the axial resolution in confocal and two-photon fluorescence microscopy, *J. Microscopy* 191 (1998) 135-140.
- 107 M.A. Model, J.L. Blank, Concentrated dyes as a source of two-dimensional fluorescent field for characterization of a confocal microscope, *J. Microscopy* 229 (2008) 12-16.
- 108 J.M. Zwier, L. Oomen, L. Brocks, K. Jalink, G.J. Brakenhoff, Quantitative image correction and calibration for confocal fluorescence microscopy using thin reference layers and SIP chart-based calibration procedures, *J. Microscopy* 231 (2008) 59-69.
- 109 C.J.R. Sheppard, M. Gu, Axial imaging through an aberrating layer of water in confocal microscopy, *Optics Communications* 88 (1992) 180-190.
- 110 C.J.R. Sheppard, T.J. Connolly, J. Lee, C.J. Cogswell, Confocal imaging of a stratified medium, *Applied Optics* 33 (1994) 631-640.
- 111 C.J.R. Sheppard, T.J. Connolly, Confocal imaging of thin films, *Three-Dimensional Microscopy*, SPIE 2184 (1994) 104-110.
- 112 K.H. Kang, S.J. Lee, C.M. Lee, I.S. Kang, Quantitative visualization of flow inside an evaporating droplet using the ray tracing method, *Meas. Sci. Technol.* 15 (2004) 1104-1112.

- 113 G. Minor, P. Oshkai, N. Djilali, Optical distortion correction for liquid droplet visualization using the ray tracing method: further considerations, *Meas. Sci. Technol.* 18 (2007) L23-L28.